AD-A090 714 NAVAL RESEARCH LAB WASHINGTON DC F/G 13/8
THE USE OF ION IMPLANTATION FOR MATERIALS PROCESSING.(U)
OCT 80 F A SMIDT
UNCLASSIFIED NRL-MR-4341 NL

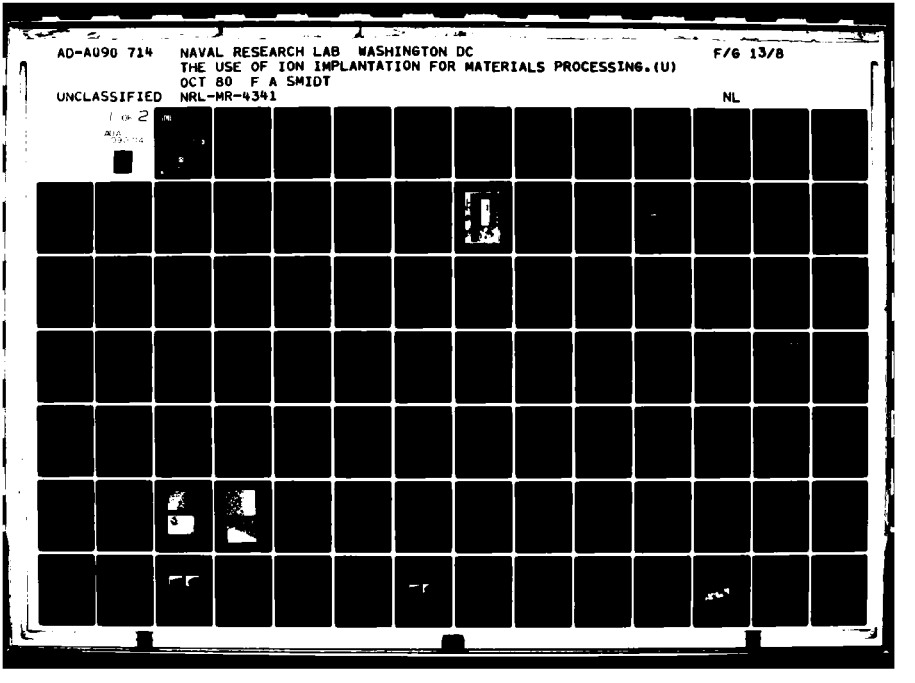

LEVEL II

NRL Memorandum Report 4341

The Use of Ion Implantation for Materials Processing

Semiannual Progress Report for the Period 1 Oct. 1979 — 31 Mar. 1980

F. A. SMIDT

Special Programs Coordinator
Material Science and Component Technology Directorate

October 6, 1980

NAVAL RESEARCH LABORATORY
Washington, D.C.

SECURITY CLASSIFICATION OF THIS PAGE (When Data Entered)

REPORT DOCUMENTATION PAGE

READ INSTRUCTIONS BEFORE COMPLETING FORM

1. REPORT NUMBER	2. GOVT ACCESSION NO.	3. RECIPIENT'S CATALOG NUMBER
NRL Memorandum Report 4341	AD-A090 714	

4. TITLE (and Subtitle)
THE USE OF ION IMPLANTATION FOR MATERIALS PROCESSING, ~~SEMIANNUAL PROGRESS REPORT FOR THE PERIOD~~, 1 OCTOBER 1979 – 31 MARCH 1980

5. TYPE OF REPORT & PERIOD COVERED
Interim report on a continuing NRL problem.

6. PERFORMING ORG. REPORT NUMBER

7. AUTHOR(s)
F.A. Smidt

8. CONTRACT OR GRANT NUMBER(s)

9. PERFORMING ORGANIZATION NAME AND ADDRESS
Naval Research Laboratory
Washington, D.C. 20375

10. PROGRAM ELEMENT, PROJECT, TASK AREA & WORK UNIT NUMBERS
(Continued on next page)

11. CONTROLLING OFFICE NAME AND ADDRESS
Office of Naval Research
Arlington, VA 22217

12. REPORT DATE
October 6, 1980

13. NUMBER OF PAGES
152

14. MONITORING AGENCY NAME & ADDRESS(if different from Controlling Office)

15. SECURITY CLASS. (of this report)
UNCLASSIFIED

15a. DECLASSIFICATION DOWNGRADING SCHEDULE

16. DISTRIBUTION STATEMENT (of this Report)
Approved for public release; distribution unlimited.

17. DISTRIBUTION STATEMENT (of the abstract entered in Block 20, if different from Report)

18. SUPPLEMENTARY NOTES

19. KEY WORDS (Continue on reverse side if necessary and identify by block number)

Auger electron spectroscopy	Ion implantation
Corrosion	Materials processing
Fatigue	Wear
Friction	X-ray photoelectron spectroscopy
Index of refraction	

20. ABSTRACT (Continue on reverse side if necessary and identify by block number)
An interdisciplinary program on the use of ion implantation for materials processing is being conducted at NRL. This report describes the important factors in ion implantation science and technology and reports progress in the use of ion implantation to modify friction, wear, fatigue, corrosion, and optical properties of materials.

DD FORM 1 JAN 73 1473 EDITION OF 1 NOV 65 IS OBSOLETE
S/N 0102-LF-014-6601

SECURITY CLASSIFICATION OF THIS PAGE (When Data Entered)

10. Program Element, Project, Task Area and Work Unit Numbers

66-0300-0-0	62761N NavMat ZF 61-544-007
66-0424-0-0	RR022-08-44 ONR WF41-401-000
66-0424-A-0	62376 NAPC/NavAir
66-0424-B-0	61101E DARPA Order 3577
66-0425-0-0	RR022-08-44 ONR
66-0420-0-0	RR022-11-41 ONR
63-1019-0-0	RR022-08-44 ONR
63-1020-0-0	RR022-01-47 ONR
61-0037-0-0	RR013-01-43 ONR

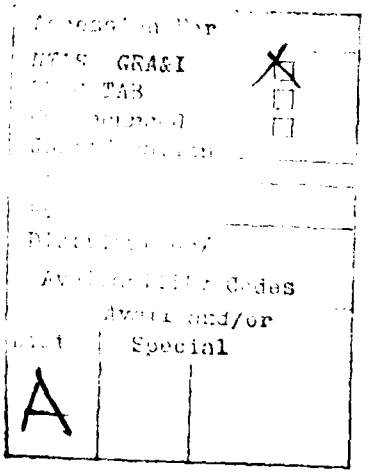

CONTENTS

THE USE OF ION IMPLANTATION FOR MATERIALS PROCESSING

Preface - F. A. Smidt

The quest for improvement in materials performance has led in recent years to the exploitation of controlled processing to enhance and tailor the properties of materials for specific applications. Ion implantation offers a powerful, broadly applicable technique for the modification of the surface region of a material. This ability to alter the surface composition and structure potentially offers a means to modify such divergent surface controlled properties as corrosion, wear, catalysis, work function, and reflectivity to name a few. The Naval Research Laboratory (NRL) is pursuing an aggressive research program to exploit the use of ion implantation for materials processing. The program includes both in-house basic research under the auspices of the Office of Naval Research and applied reseach programs for several Navy and DOD sponsors (NAVAIR, DARPA, NAVMAT, AFML, SSPO, NAVSEA). The research has reached a stage of maturity such that it seemed valuable to collect the results from various programs and publish them in one place as a comprehensive report of progress. This document is the first semi-annual report of progress for the NRL program on the use of ion implantation for materials processing.

The concept of using heavy ion bombardment to study and modify the properties of materials originated in the Nuclear Physics Division at NRL in the mid sixties. Studies of radiation damage in metals bombarded with heavy ions developed during the early seventies and the heavy ion sources currently in use were developed during that time period. The first experiments to specifically explore the modification of non-semiconductor materials by ion implantation were undertaken in 1975 when the Materials Modification and Analysis Branch (Code 6670) demonstrated that the wear and corrosion resistance of materials could be improved by ion implantation. The promise shown by the initial experiments prompted Dr. A. I. Schindler, Associate Director of Research at NRL for Material Science and Component Technology (Code 6000), to establish a broad-based interdisciplinary effort in the Radiation Technology (Code 6600), Chemistry (Code 6170), and Material Science and Technology (Code 6300) Divisions. The program is coordinated through the Ion Implantation Steering Committee consisting of Dr. J. K. Hirvonen (Code 6670), Dr. J. N. Butler (Code 6670), Dr. N. L. Jarvis (Code 6170), Dr. B. B. Rath (Code 6320), and Dr. F. A. Smidt (Code 6004), Chairman.

The program currently includes investigations of the influence of ion implantation on wear, fatigue, corrosion, and optical properties of materials as well as basic studies of the implantation process. Exploratory research in several other applications areas is also being conducted. Modern research techniques such as Auger electron spectroscopy, x-ray photoelectron spectroscopy, Rutherford backscattering analysis, nuclear reaction techniques, and transmission electron microscopy are available for characterizing the materials. Ion implantation facilities at NRL include a commercial Varian/Extrion 200-kV "high current" implanter designed for semiconductor applications and modified at

NRL to provide the vacuum chamber and work piece handling capabilities required for materials implantation, a 200-kV "low current" implanter built in 1975 at NRL as a prototype for the implantation experiments, and the 5-MV Van de Graaff accelerator.

The progress report consists of four sections describing the experimental work: Ion Implantation Science and Technology, Wear and Fatigue, Corrosion, and Exploratory Research. The latter includes several articles on implantation to modify the optical properties of silicon and a new ion beam mixing technique. A final section includes a cumulative bibliography of papers and reports published on ion implantation by NRL authors since the inception of the program. It is our hope that this report and future progress reports will provide a useful vehicle for rapidly disseminating information on the Use of Ion Implantation for Materials Processing and stimulating an exchange of ideas with potential users of this promising new technique.

THE USE OF ION IMPLANTATION FOR MATERIALS PROCESSING

SEMI-ANNUAL PROGRESS REPORT FOR THE PERIOD 1 OCTOBER 1979 - 31 MARCH 1980

SUMMARY

I. ION IMPLANTATION SCIENCE AND TECHNOLOGY

A. Ion Implantation Science and Technology

An overview of the science and technology of implanting ions into a material to modify the surface properties is presented. The components and operation of a typical ion implantation machine are described and the capabilities and limitations discussed. The physics of ion-target interactions are reviewed and the principal phenomena controlling the implantation and the material modification are examined.

B. Ion Implantation Simulations with MARLOWE

The binary-collision simulation Code MARLOWE developed by M. T. Robinson and I. M. Torrens to study the effects of neutron and heavy ion irradiations on crystalline materials has been converted to run on the NRL TI ASC Computer. A brief description of the code capabilities and the planned research is provided.

II. WEAR AND FATIGUE

A. Friction and Wear Reduction of Bearing Steel Via Ion Implantation

Ion implantation has been found to reduce friction and wear in the technologically important AISI-52100 bearing steel. Implantation of titanium at a fluence of 4.6×10^{17} ions/cm^2 and an energy of 190 keV reduces the kinetic coefficient of friction for the unlubricated steel-on-steel case from about 0.7 to about 0.3. Lubricated sliding-wear experiments show large reductions in wear for the Ti implanted steel. Other ions which reduce wear in Type 304 stainless steel, such as nitrogen and boron, are not effective in 52100 steel.

Analytical techniques are described which determine the distribution of elements in the 52100 steel after ion implantation. When Ti is implanted, Auger spectroscopy combined with sputter erosion shows an unexpected distribution of carbon atoms in the form of carbide in the first 100 nm of the surface. The Ti distribution is described in detail with two techniques: (a) Auger spectroscopy with ion beam milling, and (b) the resonant nuclear reaction profiling technique utilizing the ^{48}Ti $(p,\gamma)^{49}$V nuclear reaction. The Ti distribution shows a peak concentration of 29 ±3 at.% occurring at 70 ± 5 nm. Auger line shape analysis of the Ti shows a 2 to 3 nm layer of TiO_2 on the 52100 surface. Below the surface, TiC predominates.

Manuscript submitted July 18, 1980.

but the Ti signal becomes more metal-like as the carbide tails off. The presence of Ti and C in the 52100 steel matrix, perhaps as an amorphous layer, is inferred as the reason for friction and wear reduction.

B. Surface Hardness and Abrasive Wear Resistance of Ion-Implanted Steels

The hardness of nitrogen-implanted steel surfaces have been measured with an abrasive wear technique capable of characterizing surface layers as thin as 25 nm. Treated steel discs and reference discs were abraded with 1 to 5 μm diamond, and relative wear resistances were calculated from the mass losses. Surface hardness was obtained from a relationship between wear resistance and hardness.

The surface of a hardened and tempered carbon steel implanted with nitrogen ions (10^{17}/cm^2) was significantly harder than with other treatments including quench hardening and nitriding. The hardness is decreased to the bulk value over a depth corresponding to the initial implantation depth.

Nitrogen-implanted stainless steel surfaces wore faster than unimplanted ones, possibly due to interference with transformation hardening which normally occurs during wearing. This "softening" effect persisted to depths several times the depth of implantation, and may help to explain the reduction of sliding wear produced by the implantation of stainless steels. Analyses by Auger electron spectroscopy indicated nitrogen migrated toward the bulk during wear.

Titanium implanted in stainless steel (4.6 x 10^{17} ions/cm^2) produced a very hard surface with more than 10 times the abrasive wear resistance of the bulk metal.

C. The Chemical State of Ion-Implanted Nitrogen in Fe18Cr8Ni Steel

Auger electron spectroscopy (AES) and x-ray photoelectron spectroscopy (XPS), in conjunction with ion milling, were used to determine the chemical state of nitrogen implanted at relatively high doses (10^{16} to 10^{18}/cm^2) into Type 304 steel. Nitrogen atoms were bonded in the nitrided state, at all doses, according to both AES and XPS. As the nitrogen concentration increased, the lineshape of the Cr MVV Auger spectra evolved from that of metallic Cr to Cr nitride; at highest doses, the Fe MVV lineshape could be identifed as Fe nitride. Auger and XPS spectra of implanted 304 and thermally nitrided 304 were virtually identical at comparable nitrogen concentrations. The Cr($2p_{3/2}$) binding energies of both, however, were about 1 eV lower than found in Cr nitride but 0.5 eV higher than in metallic Cr.

D. Surface Hardening of Beryllium By Ion Implantation

The effectiveness of ion implantation for the production of a hard wear-resistant surface on instrument grade beryllium of high strength (HP-40) was explored. Samples of beryllium were implanted with boron and were subjected to microhardness tests in both the as-implanted state and after annealing. The implanted region was examined using Rutherford backscattering to determine the depth distribution of the implanted boron. By using ion implantation to produce a buried layer containing boron, the limitations imposed by solubility and diffusivity are avoided and much greater boron concentrations than those attainable with conventional thermal treatments are generated.

E. The Effect of Ion Implantation on Fatigue Behavior of Ti-6Al-4V Alloy

Ion implantation of Ti-6Al-4V with carbon and nitrogen has improved the fatigue life. Carbon has shown the best results, with a 20 percent increase in endurance limit, and a factor of 4 to 5 increase in lifetime at higher stresses. Lifetime improvement is maximum for a dose of 1×10^{17} atoms/cm^2 of carbon at 75 keV, and does not increase for greater doses. Subsurface fatigue crack origins are found for lifetimes over 10^5 cycles. TEM examination reveals TiC and TiN precipitates in carbon and nitrogen implanted regions, respectively, with a greater amount of carbide than nitride observed.

III. CORROSION

A. Corrosion Control by Ion-Implantation

An exciting new approach to corrosion control is the modification of the surface of metals by ion implantation. This paper outlines the characteristics and advantages of the ion implantation method and illustrates the approach with two examples of corrosion research in progress at the Naval Research Laboratory. The first of these is a fundamental study on the effect of implanted palladium on the corrosion of titanium in hot, concentrated acids. Implanted Pd reduces the corrosion rate of Ti by a factor of 1000, with the improvement due to retention of Pd at the surface. The second example is a practical study on the use of ion implantation to improve the corrosion resistance of bearing alloys used in aircraft engines. Preliminary results indicate that Cr implantation substantially reduces pitting corrosion of M50 steel in chloride-contaminated lubricating oil.

B. Applications of Ion Implantation for the Improvement of Localized Corrosion Resistance of M50 Bearing Steel

Pitting corrosion of M50 alloy steel bearings used in turbojet engines has been found to be a severe problem. The difficulty arises when salt-spray condensates accumulate in the engine lubricants of aircraft not in regular use. Ion implantation was applied to this problem because in the early stages of this work it was shown to be able to maintain both the dimensional stability and the contact fatigue lifetime of the M50 bearings.

Qualitative tests, which simulated the geometry and thermal cycle conditions leading to pitting of the M50 bearing surface, were performed using oil containing 3 ppm NaCl. Initially it was found that chromium surface alloys containing 20 to 25 percent chromium substantially reduced the level of attack. Prior to further corrosion simulation tests, potentio-kinetic studies were carried out on M50 implanted with chromium, molybdenum and titanium in order to screen both the passivating tendency of the surface alloys formed and their resistance to localized forms of corrosion. Singular additions of chromium, molybdenum and titanium were found to increase the resistance of M50 to localized breakdown significantly. The highest resistance to localized breakdown was found for a multi-implantation of chromium and molybdenum.

IV. OTHER EXPLORATORY RESEARCH AREAS

A. Refractive Index Profiles and Range Distributions of Silicon Implanted with High-Energy Nitrogen

Single-crystal silicon has been implanted with nitrogen ions at MeV energies, to fluences between 0.2×10^{18} and 1.65×10^{18} ions/cm^2 at a substrate temperature of 700°C. Infrared transmission and reflection spectra in the range of 1.25 to 40 μm were measured

and interference fringes were observed which are produced by the interference of light which has been multiply reflected between the front surface and the buried layers. By detailed theoretical analyses of the interference fringes we obtain refractive-index profiles, which, under suitable interpretation, provide accurate measurements of the range and straggling of the implanted ions. Rutherford backscattering measurements on the same samples confirm this interpretation. Between the energies of 0.67 and 3.17 MeV, the measured values of the projected range agree with theory after adjusting the electronic stopping power, but the straggling measurements are lower by ~ 30 percent. It is demonstrated that the asymmetry of the range distribution can be measured with this technique as well.

B. High-Fluence Implantations of Silicon: Layer Thickness and Refractive Indices

Refractive-index measurements are reported for amorphous Si produced by ion implantation. Reflection interference measurements in the frequency range $250 \lesssim \nu \lesssim 7600$ cm^{-1} were made for several Si samples implanted with P-ion fluences between 1.0×10^{16} ions/cm^2 and ion energies between 0.20 and 2.7 MeV and for Si implants of 1.0×10^{16} and 3.0×10^{16} ions/cm^2 and an ion energy of 0.30 MeV. The interference measurements were computer analyzed by using a model in which the damaged layer has a refractive index n_D and extinction coefficient k_D, and the substrate has a refractive index n_s and $k_s = 0$. The optical constants of the two regions are smoothly connected by a transition region approximated by a half-Gaussian curve of standard deviation σ_D. The finite-width transition region is necessary for fitting the data. Excellent fits are obtained for literature values of n_s and k_D with the chi-square being $\simeq 10^{-5}$. The value of k_D has little effect on the analysis. Within the experimental accuracy a single curve for $n_D(\nu)$ is obtained for the amorphous region where $n_D(\nu)$ is independent of the ion type, ion energy, ion fluence, or position in the amorphous layer. The thicknesses of the damaged layers deduced from the infrared data agree well with LSS values for $R_p + \sigma_p$ and with channeling results. Visual observations of the thicknesses also agree well for the high-energy implants but not for the lower-energy ones.

C. Plasma Region in High-Fluence Implants of Phosphorus in Amorphized Silicon

Phosphorus ions were implanted into silicon previously made amorphous by implantation with neon ions of projected range considerably greater than that of the P^+ ions. Comparison of the annealing behavior for this case with that for P^+-only implants indicates that free-carrier plasma formation in the region of high phosphorus concentration does not occur until the material has recrystallized.

D. High-Dose Implantation and Ion-Beam-Mixing

Substitutional solid solutions and metastable phases in single-crystal metals can be produced by ion bombardment either by ion implantation to high-dose levels of one of the elements or by implantation of inert ions through a thin film to induce atomic mixing between the film and the single-crystal substrate. In this paper we compare these two methods of high-dose implantation and ion-beam-mixing to introduce Au and Pd into single-crystal Cu. In direct implantation the maximum concentration of implanted ions is determined by sputtering effects whereas in ion-beam-mixing the concentration is determined by the film thickness and the amount of interdiffusion over the penetration depth of the energetic ions.

With implantation of 1×10^{17}/cm^2 Au or Pd ions at 150 keV into $<110>$ Cu, high substitutional concentrations at about 6 at.% were achieved. With ion-beam-mixing of ~ 10 nm Au or Pd films by 300 keV Xe ions at ion doses $\lesssim 1 \times 10^{16}$/cm^2, substitutional concentrations twice as high ($\simeq 12$ at.%) were achieved. With thicker films, higher concentrations of Au and Pd were achieved with polycrystalline solid solutions formed at Au and Pd concentrations above 30 at.%.

Section I.A

ION IMPLANTATION SCIENCE AND TECHNOLOGY

J. W. Butler[1]

[1]Materials Modification and Analysis Branch
Radiation Technology Division
Naval Research Laboratory

This work was supported by the Office of Naval Research.

ION IMPLANTATION SCIENCE AND TECHNOLOGY

J. W. Butler

Materials Modification and Analysis Branch
Radiation Technology Division

Introduction

Ion implantation is a process for injecting atoms of any element into any solid material to selected depths and concentrations. One thereby forms an alloy or other solid mixture that has a different composition from the original and which therefore exhibits different (and sometimes highly desirable) chemical and physical properties.

An ion-implantation accelerator of the type used by NRL is illustrated schematically in Fig. 1. Atoms of a selected chemical element are ionized by collisions with electrons in an electrical discharge in a gas at low pressure in the ion source. These ions then pass through an orifice into a high-vacuum region where they are accelerated by an electric field to a moderate energy (10-30 keV) and analyzed by a magnetic field according to ion mass. The selected ions are then accelerated by another electric field to the desired implantation energy. When the ions strike and penetrate the target lattice, they lose energy through collisions with lattice atoms and come to rest. Table I lists ranges of typical values of certain technical parameters and economic factors which apply to ion implantation performed to modify the chemical, optical, or mechanical properties of materials.

Table I. Ranges of technical parameters and economic factors. These ranges represent typical, rather than absolute, limits for implantations to modify chemical, optical, or mechanical properties.

ion species	any element or combination
target material	any solid material
target preparation	surface clean and smooth
target dimensions	less than 2 m
target temperature	-196°C to 300°C
pressure in beam tubes	10^{-5} torr to 10^{-7} torr
potential on terminal	10 kV to 1000 kV
depth of implanted ions	10 nm to 1 μm
ion beam current	1 nA to 20 mA
ion beam cross section	0.1 cm^2 to 1 cm^2
ion fluence or dose	10^{16} atoms/cm^2 to 10^{18} atoms/cm^2
relative concentration	1 at.% to 50 at.%
surface erosion	1 nm to 100 nm
capital investment	$200,000 to $400,000
power requirement	5 kVA to 20 kVA
floor space requirement	10 m^2 to 20 m^2
implantation costs	1¢/cm^2 to $1/$cm^2$

A few exploratory experiments involving the bombardment of semiconductor materials by high-energy ions as a means of altering the electrical characteristics of these materials were performed in the 1950s; and three broad U.S. patents[1-3] were issued in the late 1950s on the ion implantation technique. Although commercial exploitation of the process for the manufacture of semiconductor devices was delayed because of industry concern about the problem of radiation damage (whether annealing could remove the lattice damage produced by collisions of the implanted ions with lattice atoms), the semiconductor device industry did begin to use ion implantation to dope semiconductor devices during the late 1960s. Since the early 1970s ion implantation has been widely used by the semiconductor device industry to introduce dopants into many types of devices, including large scale integrated circuits such as are used in pocket calculators. The main reasons for this widespread use are the reproducibility and controllability of the process; it is used mainly as a predeposition technique, followed by thermal diffusion. Also during the early 1970s a few laboratories worldwide began to experiment with the modification of the chemical, optical, and "mechanical" properties of materials by means of ion implantation. In 1975 the Naval Research Laboratory began a program to investigate the effect of ion implantation on the mechanical and chemical properties of metals. In 1976 the program was extended to optical properties of materials such as silicon or magnesium fluoride.

[1] U.S. Pat. 2,750,541 (June 12, 1956), R. S. Ohl.
[2] U.S. Pat. 2,787,564 (April 2, 1957), W. Shockley.
[3] U.S. Pat. 2,842,466 (July 8, 1958), J. W. Moyer.

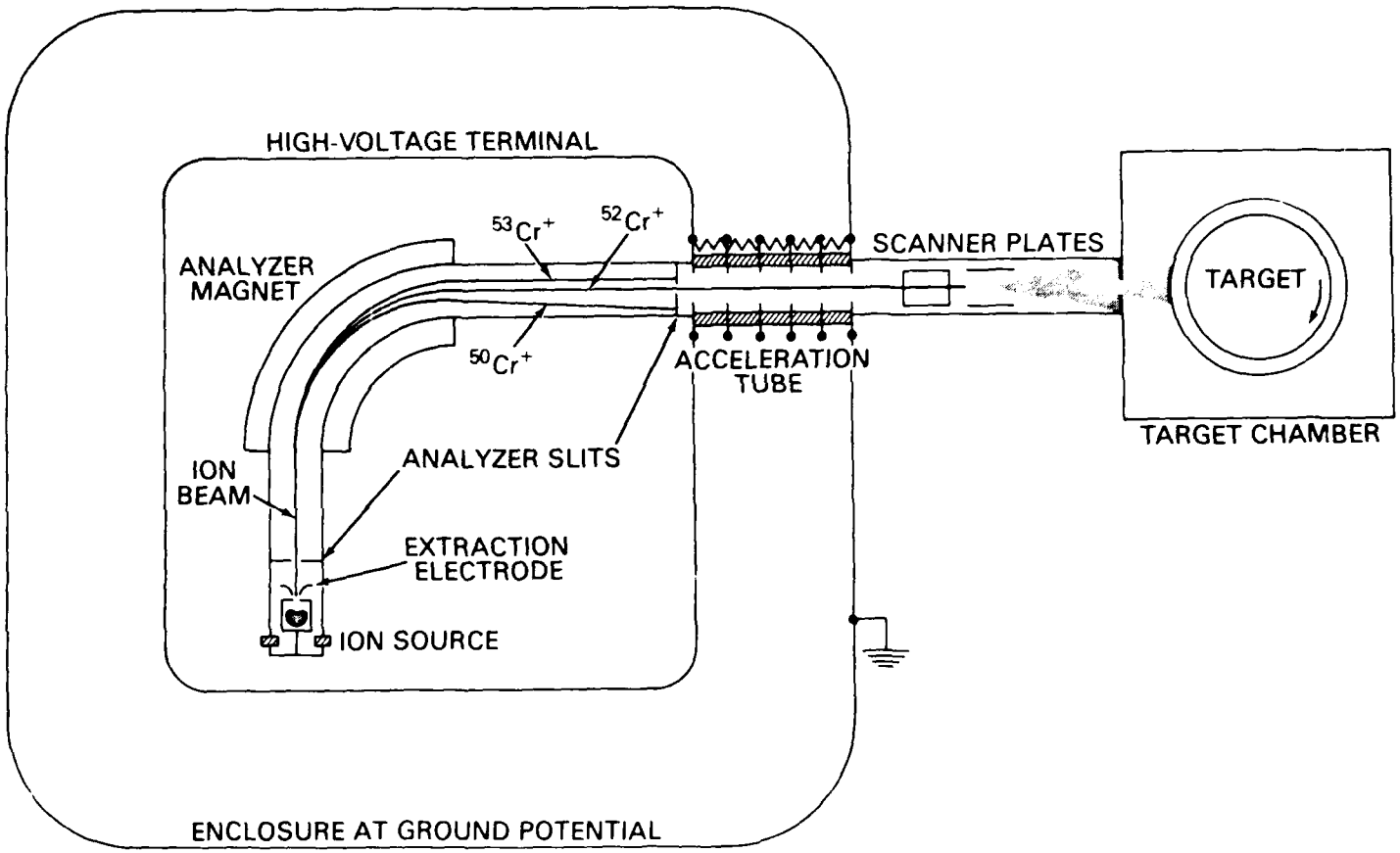

Figure 1. A schematic drawing of an NRL ion implantation machine. Ions from the source are accelerated to an energy of about 25 keV by the extraction electrode, then pass through the mass analyzer; the heavier the ion, the smaller the deflection. In this example, the magnet current is set so that the most abundant isotope of chromium (^{52}Cr) passes through the analyzer output slit. The selected ions are then accelerated to the desired energy, refocussed by a quadrupole lens (not shown), deflected by a scanner system, collimated by a defining aperture, and allowed to strike the target (which in this example is rotating to enable all-around implantation and also to spread out power dissipation).

The Technology of Ion Implantation (Implanters)

Ion Source. For implantations performed to modify the chemical, optical, or mechanical properties of a material, substantial concentrations of implanted ions are required (typically about 20 at.%). Such concentrations in turn require a relatively large number of implanted ions per unit area (or "fluence" or "dose"). So large ion beam currents are required. The NRL machine (Fig. 1) produces beams in the fraction of a milliampere region for many species of ions.

Figure 2 is a schematic drawing of the NRL gas-discharge type of ion source. The electrons from the hot filament, repelled by the negative potential of the filament (about 100 V with respect to the source wall), are accelerated,

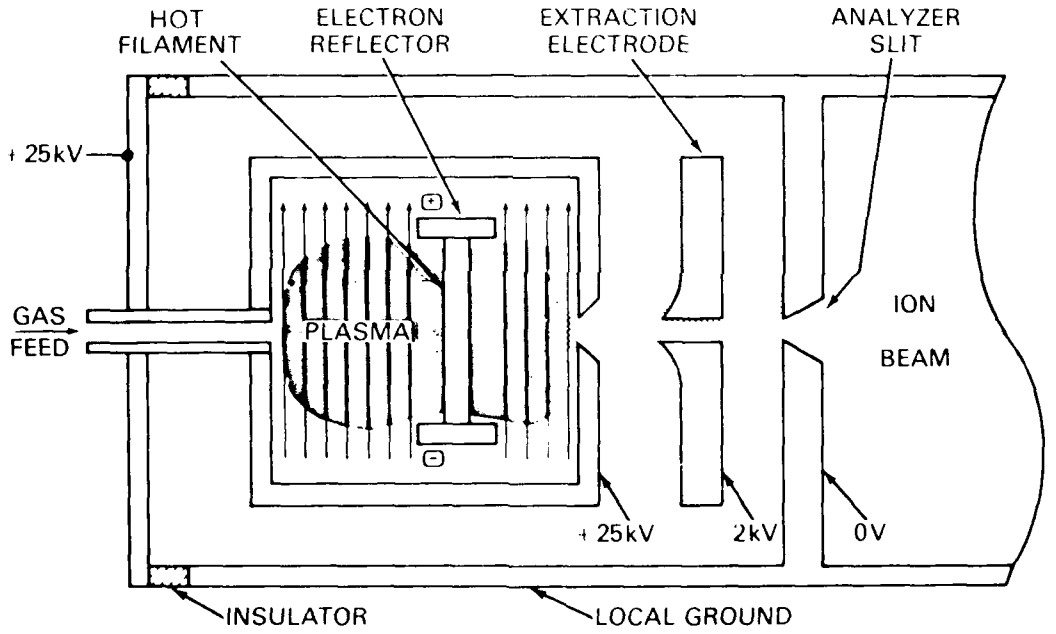

Figure 2. A schematic drawing of an NRL gas discharge ion source, extraction electrode, and entrance slit to the mass analyzer. Electrons from the hot filament are repelled by the potential (-100 V with respect to the source wall) on the filament and collide with gas molecules at a pressure in the millitorr region, thereby ionizing them. The resulting plasma is confined by a uniform axial magnetic field (parallel to the filament) and by electron repeller plates at the same potential as the filament. The extraction electrode serves a triple purpose: pulling ions out of the source, focusing them into a beam, and accelerating them for mass analysis prior to the major acceleration to implantation energy.

colliding with gas molecules and atoms at low pressure, thereby ionizing them and producing a plasma, which is confined by an axial magnetic field (illustrated by the arrows) and by electron repeller plates at the ends of the filament. The ion source in this example has a fixed potential of +25 kV with respect to the terminal (or local ground). The ion extractor electrode potential (in this example, -2 kV with respect to local ground or -27 kV with respect to the source) is variable to accommodate different source operating conditions. The extractor attracts the positive ions out of the source plasma, focuses them into a beam, and accelerates them for subsequent mass analysis. The negative potential (with respect to local ground) of the extractor shields the positive-potential source from downstream secondary electrons, thereby preventing unnecessary drain on the 25-kV power supply and also preventing unnecessary x-ray generation. In addition, this negative potential of the extraction electrode with respect to local ground helps to maintain the stationary "satellite electron gas" that neutralizes the space charge of the beam in the field-free region downstream from the grounded jaws of the analyzer slit. (Without the neutralizing effect of this electron gas, the low-energy high-current positive-ion beam would diverge rapidly under the mutual repulsion of the ions, and most of the beam would strike the jaws of the output slit.)

Mass Analyzer. The ion beam from a source usually contains impurities: vacuum system contaminants from residual air, from vacuum pumps, or from solid components of the source. When an ion that does not exist as an elemental gas is produced in an ion source, the ion beam contains even more undesired components. For example, if boron ions are to be accelerated, the source feedstock may be BF_3, which produces several kinds of molecular ions from various combinations of atoms present.

The ions from the source must be accelerated (or extracted with a substantial energy), focused into a beam, and then mass analyzed so that these undesirable ions in the beam can be removed prior to implantation (or, as in Fig. 1, prior to the main acceleration).

For a magnetic mass analyzer, shown schematically in Fig. 1, the product of magnetic field H and path radius of curvature r is proportional to the square root of the ratio of ion mass m to charge q or

$$Hr \propto V^{\frac{1}{2}} (m/q)^{\frac{1}{2}}, \tag{1}$$

where V is the accelerating potential. Figure 3 shows the mass spectrum of the output of the ion source during the implantation of chromium ions.

Acceleration Tube. The function of an acceleration tube is to provide (a) an evacuated path for the ions and (b) an electric field to accelerate them. The electric field is in addition shaped so as (i) to tend to focus the beam of selected ions from the mass analyzer and (ii) to impede the backstreaming secondary electrons. The tube consists of a series of sections, each section being an annular insulator (glass) and a shaped metal electrode (polished aluminum) cemented together. A resistor stack distributes the potential drop approximately uniformly along the tube (but some nonlinearity has been introduced to improve focusing.)

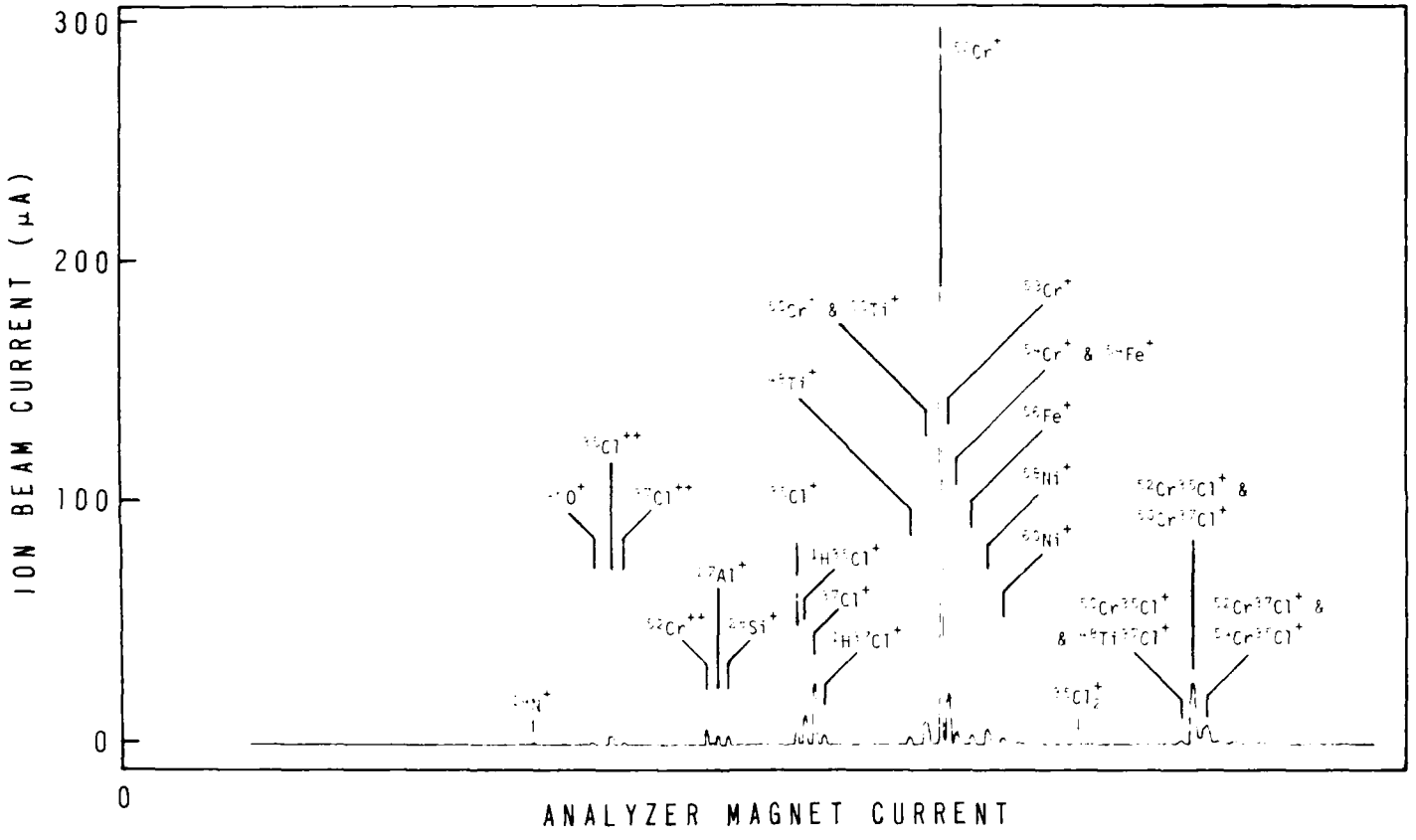

Figure 3. Mass spectrum from the NRL hot-filament gas-discharge ion source producing chromium ions from chromium chloride molecules made from the interaction of chromium lumps inside the source with chlorine gas at a pressure in the millitorr region. This spectrum, which is a plot of the analyzed ion beam current as a function of analyzer magnet current, was taken shortly after a changeover from an implantation involving iron, titanium, and nickel. These vestige peaks, along with the comtaminant-gas peaks, disappeared after a few hours of operation. This figure illustrates many of the types of components found in a mass spectrum: singly ionized atomic ion contaminants, doubly ionized atomic components, diatomic gases, and compound molecules. Not all multiple occupancies of mass locations are indicated here; e.g., the $^{27}Al^{+}$ peak also includes $^{54}Cr^{++}$ and $^{54}Fe^{++}$.

Target Chamber. The primary function of the target chamber is to provide line-of-sight high-vacuum access to each area to be implanted. It is customary, but not necessary, for the beam to strike the target at normal incidence; at nonnormal incidence, the penetration is smaller, and target sputtering (discussed below) is greater. Figure 4 is a photograph of an NRL target chamber taken during the implantation of the steel balls (2.2 cm diameter) from a bearing from a jet engine. The chamber interior dimensions are about 25 cm x 25 cm x 45 cm; but a chamber 2.3 m long and 2.3 m in diameter has been constructed at the Atomic Energy Research Establishment at Harwell (England).

The target chamber together with auxiliary equipment (some of it external to the chamber and not strictly part of the target chamber) also provides at one time or another the following functions:

Ion-beam-current integration (by means of which the dose is measured),
Secondary electron suppression (to avoid ion-beam-current errors),
Vapor condensation (by means of a cold tube containing liquid nitrogen),
Differential pumping (high vacuum to inhibit target contamination),
Beam sweeping (to scan the target as an electron beam in a kinescope),
Target manipulation (to expose every part of the target to the beam),
Target cooling (heat transfer system to dissipate ion beam power), and
Auxiliary magnet (to separate the desired beam from any neutral beam).

In a production system, the target chamber would also provide for automatic target changing (by means of vacuum locks and a conveyor).

Power Dissipation. The power density of the beam at the target can be substantial. For example, a 0.5 mA beam of 200-kV ions has a power of 100 watts. If the beam has a cross section of 0.5 cm^2, then the power transport density is 200 W/cm^2. If the ions are chromium and the target, ordinary steel, the ion range is about 60 nm, and the volume power density in the implantation region of the target is about 33 MW/cm^3. Therefore precautions must be taken to prevent unwanted temperature excursions of the target; e.g., scanning the beam over the front of the target and rotating the target about its own axis. Such techniques can keep the average target temperature within tolerable limits (e.g., 100°C).

The power dissipation problem is exacerbated by the vacuum environment of the target: The principal mode of heat transfer may be radiation, and polished metals are poor radiators. Conduction transfer is significant only if the target makes good contact with a material (i) that is soft enough to conform to the microscopic contours of the target, (ii) that itself is a good conductor of heat, and (iii) that is thermally coupled to a heat sink. Silicon wafers are usually cooled during implantation by such techniques.

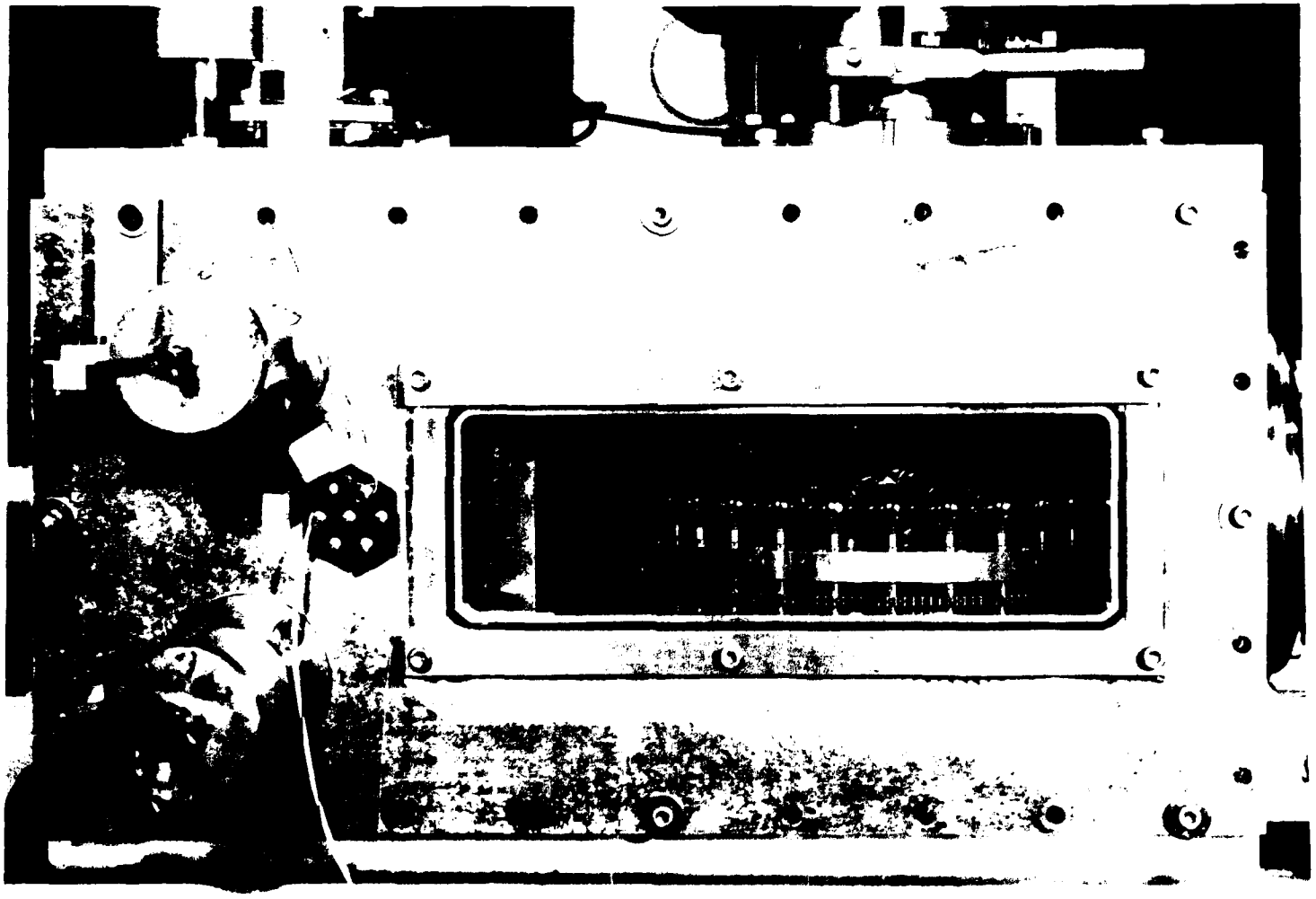

Figure 4. Photograph of an NRL target chamber. The ions, coming from the left, strike the targets seen through the window: 2.22-cm-diameter balls from the main thrust bearing of the J-79 jet engine. Each ball pedestal rotates about its own axis, and the entire carousel rotates about its axis.

The Science of Ion Implantation (Ion-Target Interactions)

When a high-energy ion strikes a solid target, the ion collides with the individual atoms in the target, loses energy, knocks some atoms out of their lattice sites, and comes to rest after penetrating a few hundred atom layers, in a time of roughly 10^{-13} s. The implanted ions (or atoms) generally have the same effect on the properties of the material as if they had arrived at the same lattice locations by some other means (such as in the melt or by thermal diffusion or by quenching). But the effect of the implantation process per se (viz., displacements and other microstructure changes) must also be considered in assessing the overall effect of the implantation.

Atomic Collisions. The collisions between the incident ion and lattice atoms involve two basic types of energy transfer: (i) *elastic*, in which the two partially screened nuclei experience each other's Coulomb field, transferring momentum in the process as in a billiard-ball collision, and (ii) *inelastic*, in which energy is transferred to the electrons of the struck atoms.

A binary collision model[4,5] is used to calculate the magnitudes of the energy and momentum transfers, and in this model the elastic and inelastic contributions are assumed to be independent, with no interference between the two. (This assumption is not strictly true, but it provides results which are tractable.) The nature of the interaction is strongly dependent on the instantaneous energy of the incident ion E_1, the atomic number of the incident ion Z_1, and the atomic number of the target atom Z_2. Generally, for large values of E_1 and for small values of Z_1 (e.g., a 100-keV helium ion), the predominant mode of energy transfer is inelastic; for relatively low values of E_1 and for large values of Z_1 (e.g., a 10-keV molybdenum ion), the elastic mode of energy transfer predominates. Figure 5 illustrates the variations of the energy loss per unit path length as a function of E_1 for two values of Z_1 and for each kind of collision in a target of iron.[6-8] The crossover point for incident iron ions is about 500 keV; but for nitrogen ions, about 30 keV.

The qualitative features of the energy loss rate curves of Fig. 5 may be understood as follows. For low ion energies and for a "hard" *elastic* interaction potential ϕ between ion and atom (viz., if ϕ falls off more sharply than r^{-2}, as is assumed for the ion-atom interaction) the elastic energy transfer rate increases with ion energy for basically the same reason as with billiard ball collisions. But unless the potential is infinitely hard, at sufficiently *high* speeds for the incident ion the interaction time is so short that the atom cannot be fully accelerated during the interaction (except for rare head-on collisions, for which the

[4]J. Lindhard, V. Nielsen, and M. Scharff, Kgl. Danske Videnskab. Selskab, Mat.-Fys. Medd. **36**, No. 10 (1968).
[5]M. Robinson and I. M. Torrens, Phys. Rev. **B9**, 5008-5025 (1974).
[6]J. Lindhard, Kgl. Danske Videnskab. Selskab, Mat.-Fys. Medd. **28**, No. 8 (1954). O. B. Firsov, Sov. Phys. JETP **9**, 1076 (1959).
[7]J. Lindhard, M. Scharff, and H. E. Schiott, Kgl. Danske Videnskab. Selskab, Mat.-Fys. Medd. **33**, No. 14 (1963).
[8]I. Manning and G. P. Mueller, Comp. Phys. Comm. **7**, 85 (1974).

interaction potential is hard indeed). (The momentum transferred is $\int F dt$.) Thus the energy loss rate decreases for higher ion energies as illustrated in Fig. 5. The *inelastic* energy transfer rates (Fig. 5) have a constant slope of 0.5, implying that the inelastic transfer rate is proportional to $E^{\frac{1}{2}}$ or to the ion velocity **v**. This relationship comes from the model of the inelastic interaction as follows. When the electron shells of incident ion and host atom overlap, some electrons change their atomic identification and transfer momentum m**v** to the electronic structure of the recipient atom. The effective inelastic force between the two atoms is therefore, according to the model, equal to the product of the electron transfer rate and m**v**. So the inelastic energy transfer is proportional to $\int m\mathbf{v}\cdot d\mathbf{R}$, where **R** is the relative position vector.

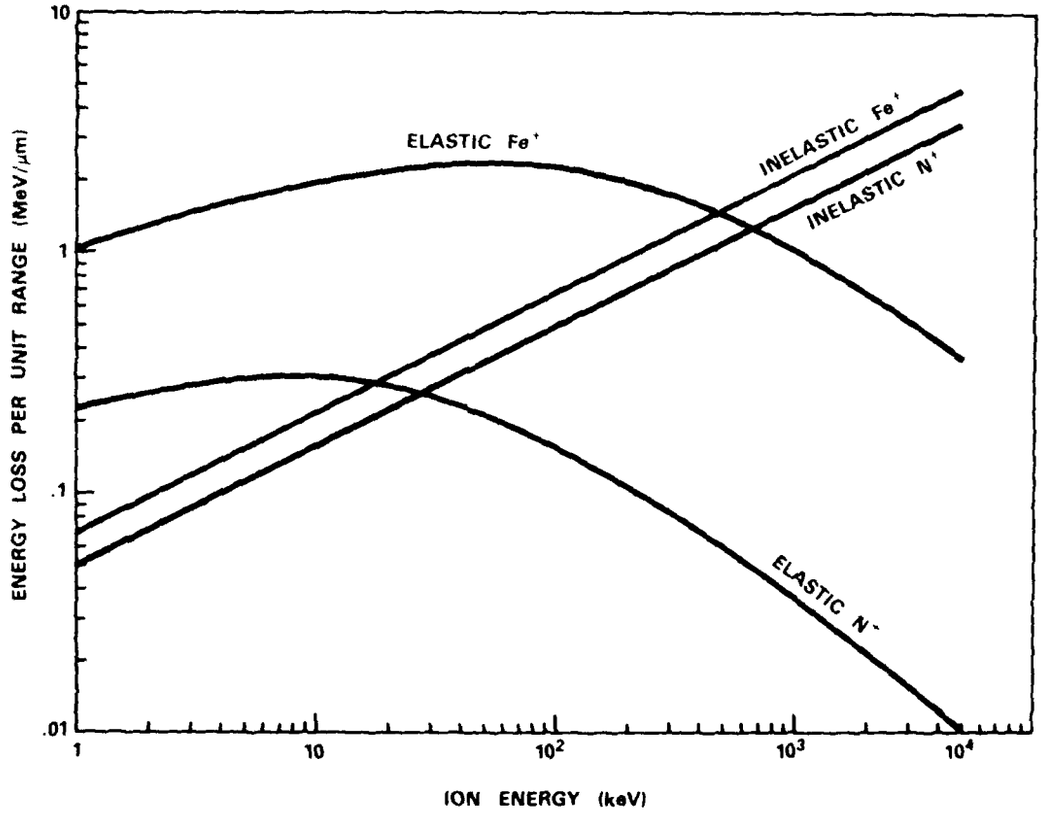

Figure 5. A logarithmic plot of the rate of energy loss of iron ions and nitrogen ions in an iron sample as a function of instantaneous ion energy.[4-8] The total energy loss rate is separated into the elastic part (that results in displaced host atoms) and the inelastic part (that results in electronic excitation of the host atoms).

Ion Range. Because the incident ion is deflected by elastic collisions, its path is not straight. For a homogeneous beam of iron ions striking an iron target at normal incidence, a group of paths might look roughly like the sketch in Fig. 6. It is customary to define the word "range" as the projected length of the path onto the beam's initial velocity vector. Variations in the range from ion to ion (with all conditions the same) arise because of statistical fluctuations in (i) the energy losses in elastic collisions and (ii) the direction of the ion after a collision. (Those collisions that involve greater energy transfers also involve greater deflections.) The inelastic collisions are assumed to constitute a smooth braking force, hence do not contribute to the straggling in range. If the projection of the initial velocity vector is divided into equal increments or bins and then the number of ion path projections that terminate in each such bin are counted, a range distribution curve, such as that shown at the bottom of Fig. 6, may be obtained.

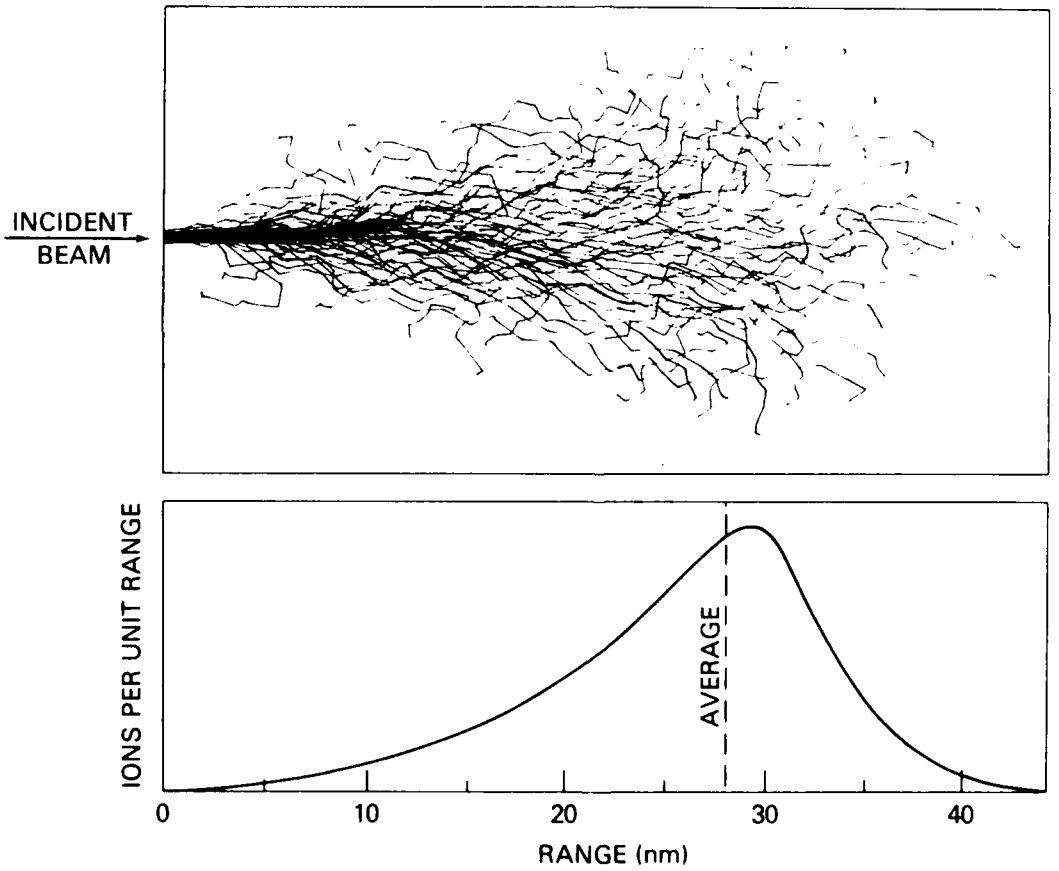

Figure 6. A schematic representation of a number of ion paths from a homogeneous beam of 100-keV iron ions entering a block of iron from the left. In general, the range distribution curve at the bottom may be skewed either to the right or to the left, depending on the ion species, energy, and target material. For implantations performed to modify the chemical or mechanical properties of material surfaces, it is customary to assume a gaussian shape for the distribution.

The distribution in range in Fig. 6 is asymmetric, being skewed toward shorter ranges. The precise shape of the distribution depends on the ion species, incident ion energy, and target material. Even for a given ion species and target material the skewness may be either toward the right or the left, depending on the incident ion energy. For implantation into semiconductor devices, the skewness may be important because tails on the distribution may lead to free carriers existing in regions where free carriers are not desired, but for implantations performed to modify the chemical or mechanical properties of materials, the precise shape of the distribution is not so important. Hence for reasons of convenience, the distribution in range (hence the distribution in concentration of implanted ions) is usually assumed to have a gaussian shape.

Figure 7 shows the calculated distribution of ranges for several incident energies of iron ions implanted into an iron sample (calculation based on references 7 and 8). Figure 7 suggests the possibility of tailoring the depth concentration profile of implanted ions so as to achieve almost any desired smoothly varying (or constant) profile. Of course the range is dependent on Z_1 and Z_2 as well as E_i. Figure 8 illustrates the dependence on Z_1 by showing the calculated range distributions of nitrogen ions with all other parameters the same as in Fig. 7.

Several computer codes are available, and a few tabulations[9] of results have been published, providing values of mean range and standard deviation for any combination of ion and solid material. The uncertainties in the calculations arise mainly from the method of obtaining the inelastic braking force. The best calculations have uncertainties of about 20%; and others, about 30%. A combination of experiment (i.e., measurement of the depth concentration profile of implanted ions for a few energies) and theory can give substantially more accurate values.

An experiment at NRL involving the implantation of high-energy (0.6 MeV to 3 MeV) nitrogen ions into silicon single crystals[10] implies that the range straggling predicted by conventional theory[7] is too large. Since range straggling is caused mainly by elastic collisions, this result implies that the cross section for elastic atomic collisions used in reference 7 is too large. Wilson, Haggmark, and Biersack[11] have recently developed a more sophisticated theory for this cross section. I. Manning[12] at NRL is now applying the Wilson *et al.* cross section to analyze the NRL experimental results. Similar analyses will be made for future NRL experiments that result in accurate experimental values of range straggling. The result may determine which is the more valid cross section (Lindhard *et al.* or Wilson *et al.*).

[9] D. K. Brice, Ion Implantation Range and Energy Deposition Distributions, Vol. 1, High Incident Ion Energies, Plenum Press, New York, Washington, and London, 1975; K. B. Winterbon, Ion Implantation Range and Energy Deposition Distributions, Vol. 2, Low Incident Ion Energies, Plenum Press, New York and London, 1975; J. F. Gibbons, W. S. Johnson, and S. W. Mylroie, Projected Range Statistics, 2nd ed., Halsted Press, a div. of John Wiley & Sons, Inc., New York, 1975. Also see paper IB in the present report.

[10] G. K. Hubler, P. R. Malmberg, T. P. Smith, III, paper IVA in the present report.

[11] W. D. Wilson, L. G. Haggmark, and J. P. Biersack, Phys. Rev. **B15**, 2458 (1977).

[12] Irwin Manning, Radiation-Matter Interactions Branch, NRL.

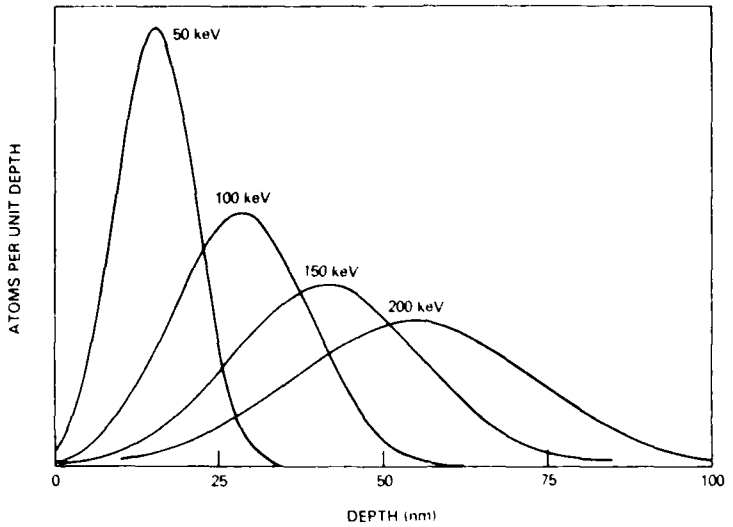

Figure 7. The calculated range distributions for iron ions of various incident energies E_i in an iron sample at normal incidence (based on references 7 and 8). By judicious choices of incident ion energies and fluences one can tailor the depth concentration profile of implanted ions to particular needs. Sputtering of the surface influences the final depth concentration profile of the implanted atoms.

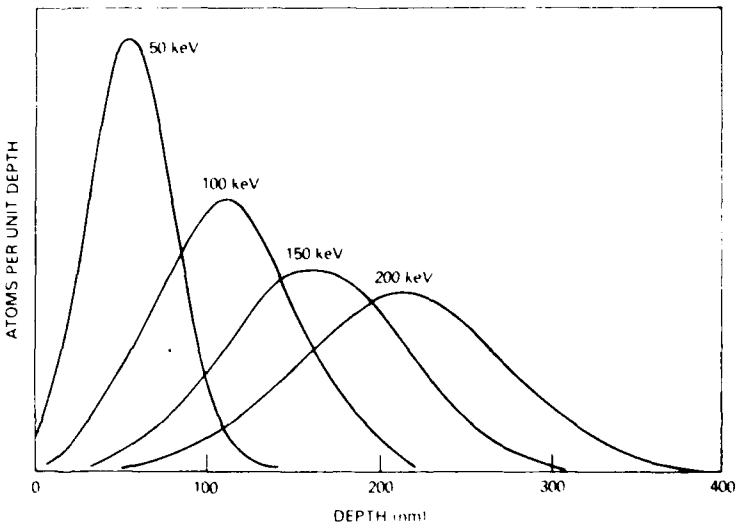

Figure 8. The calculated range distributions (or depth distributions of implanted ions for normal incidence) for nitrogen ions of various incident energies E_i in an iron sample.[7,8] This figure together with Fig. 7 illustrates the variation of range with respect to the atomic number of the incident ion Z_1. For convenience of visual comparison the nitrogen range distributions have been compressed horizontally and stretched vertically by a factor of four with respect to the curves in Fig. 7. The area under each curve is proportional to the total number of implanted ions in each case; the areas under all eight curves are the same.

Channeling. The preceding section on ion range, was discussed under the implicit assumption that the target atoms were located randomly. In metals, grains (which are miniature crystals) typically have random orientations; hence for any region much larger than a grain, this implicit assumption of random arrangement of atoms is reasonable. But if the incident ions are within a small angle (typically 1^{o}) of a low-index direction in a single-crystal target, then most of the ions are steered[13] through the "channel" as illustrated by trajectory A in Fig. 9. No displacements occur; so the only energy transfers are inelastic (electronic), and in a perfect crystal the ion's range may be several times the normal value. If a defect is present (such as an interstitial, vacancy, dislocation, impurity atom, or thermal perturbation) it is likely to dechannel the ion, as illustrated by trajectory B.

Because typical commercial materials are not single crystals and because large implantation doses destroy the regularity if the target *is* a single crystal, channeling is important in ion implantation only in special cases, such as where deep implants of small doses are desired (e.g., radioactive ions, dopants for luminescence, or dopants for certain semiconductor devices). Sometimes, however, channeling is hard to avoid (e.g., with low-energy heavy ions in a single-crystal target) because (i) the critical angle may be several degrees and (ii) there are many directions that produce channeling.

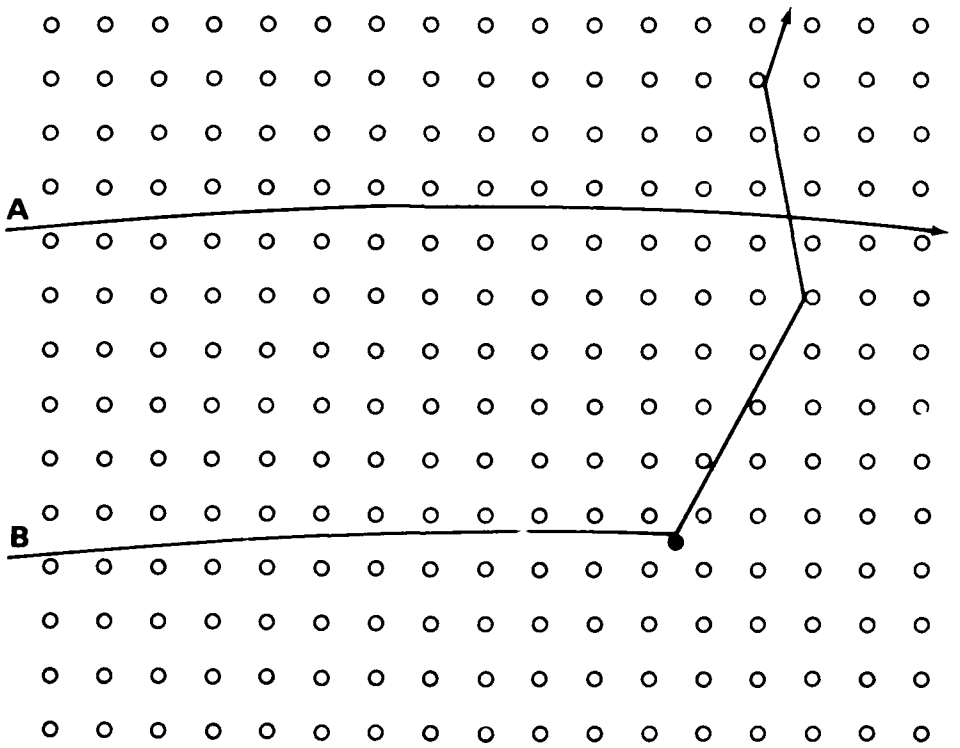

Figure 9. Schematic representations of ion trajectories in a crystal lattice. A: The path of a channeled ion being steered by the lattice rows. B: The path of an ion dechanneled by an interstitial atom.

[13]M. T. Robinson and O. S. Oen, Phys. Rev. **132**, 2385-2398 (1963).

Radiation Damage. To displace an atom from its lattice site requires the expenditure of a minimum amount of energy that lies between 20 eV and 40 eV for most materials; the average displacement energy E_d is about 25 eV. When a collision between an incident ion and a target atom causes an energy transfer much greater than E_d, the struck atom then collides with other atoms, knocking some of them out of their lattice sites. This process creates a cascade of collisions producing secondary and tertiary knock-on atoms. Thus an ion leaves a path of havoc in its wake, and the residual effect of this havoc is called "radiation damage." However, this term is somewhat misleading because the overall result may be beneficial instead of detrimental. For example, the ion beam tends to clean the surface (by means of sputtering); and the interstitial atoms produce in the implanted layer compressive stresses which appear to play a role somewhat analogous to those in prestressed concrete. This section considers the volume effects of the passage of the ions (displacements), and the next section considers the surface effects (sputtering).

The total number of atoms displaced depends on a number of factors: the average displacement energy E_d, the ion's initial energy E_i, the relative masses of the colliding atoms, and the dose or fluence of implanted ions. (The *flux* of incident ions is defined as the number of ions per unit area per unit time striking the target, and the *fluence* (dose) is defined as the integration of flux over time. So fluence has dimensions of ions per unit area.) For the situation in which the bombarding species and bombarded species are the same, the number of displacements per incident ion (N_d) is given by the approximation

$$N_d = 0.8\ \nu(E)\ E_i/2E_d, \tag{2}$$

which is a variation of the Kinchin-Pease[14] formula, which was orginally derived for calculations of radiation damage to reactor materials by neutrons. The energy partition function $\nu(E)$ represents the fraction of the total energy transfer that goes into elastic collisions. This function was not in the original Kinchin-Pease derivation because, in the neutron knock-on energy regime, essentially all the energy loss is of the elastic type. The "2" in Eq. 2 is a statistical factor that arises from the model, in which the final displacement collision in each branch of the cascade results in two atoms, each of which possesses a kinetic energy of E_d or less. Although the original formula (without $0.8\ \nu(E)$) was derived under rather crude assumptions, after it had been used for more than a decade, computer simulations[15] showed that it is surprisingly accurate if one merely multiplies the right-hand side by $0.8\ \nu(E)$.

For example, when a 100-keV iron ion is implanted into an iron specimen, application of Eq. (2) indicates that on the average *each lattice atom* of iron in the region traversed by the ions is *displaced about 500 times during the bombardment.* This number taken by itself seems to raise the question whether the implanted region can maintain its structural integrity. Metals usually do

[14]G. H. Kinchin and R. S. Pease, Rep. Prog. Phys. **18**, 1-51 (1955).
[15]M. J. Norgett, M. T. Robinson, and I. M. Torrens, Nucl. Eng. Deg. **33**, 50-54 (1975).

maintain their structural integrity, and the reason is that almost as many lattice-vacancy/interstitial-atom recombinations as displacements occur. There are several mechanisms by means of which these recombinations occur. One mechanism is thermal activation (except at cryogenic temperatures). Another mechanism is the mutual elastic interaction between defects in metals, even in the absence of thermal activation. For example, an interstitial atom and a vacancy may combine (by means of the ordinary phenomenon of barrier penetration from wave mechanics) even at cryogenic temperatures from separations as great as two or three atoms by sucessive spontaneous lattice jumps towards each other. These considerations imply that an upper limit to the number of interstitial-vacancy pairs in the implanted region of a metal, even at cryogenic temperatures, is roughly one percent of the lattice sites. At room temperature, thermal activation normally causes the actual net relative number of displacements to be substantially less than this upper limit.

Radiation damage must be annealed out of semiconductor devices after implantation because the disorder causes a drastic reduction in minority carrier lifetime. The annealing is usually performed at a temperature between 300°C and 900°C, depending on the ion species, semiconductor material, attached materials (such as aluminum leads), implantation energy, and dose; but some devices are annealed by laser or electron beams. During the annealing process, the amorphous layer may recrystallize epitaxially onto the undisturbed substrate.

For implantations in alloys to enhance their resistance to corrosion or wear, the residual radiation "damage" may even be beneficial, hence is usually not annealed out. One reason is that the implantation process leaves many atoms (both implanted and host) in interstitial sites in the implanted layer (typically, a few hundred atoms thick). These interstitials constitute, in effect, wedges. As a result, this layer tends to expand, but the expansion is restricted by the much thicker substrate and by the surface energy. The result is a compressive stress near the surface, and this compressive stress may inhibit the initiation or propagation of cracks, thereby accounting in part for the observed improvements in mechanical properties of the material. Another reason that radiation damage may be beneficial is that, under some unusual conditions, ion implantation in metals may produce an amorphous surface layer even for metals,[16] and some amorphous metals produced by means other than ion implantation have been found to possess greater strength than the corresponding crystalline alloys[17] and also to possess greater corrosion resistance.[18] A potential detrimental effect of residual radiation damage in crystalline metals is the existence of high-energy sites that may be vulnerable to corrosion.

[16]A. Ali, W. A. Grant, and P. J. Grundy, Phil. Mag. **37B**, 353-376 (1978); Radiat. Eff. **34**, 251-254 (1977).
[17]T. Masumoto and R. Maddin, Mater. Sci. Eng. **19**, 1-24 (1975).
[18]T. M. Devine and L. Wells, Scr. Met. **10**, 309-310 (1976); M. Naka, K. Hashimoto, and T. Masumoto, Corrosion **32**, 146-152 (1976); K. Hashimoto, K. Osada, T. Masumoto, and S. Shimodaira, Corros. Sci. **16**, 71-76 (1976).

A computer code which is now under development[19] at NRL utilizes the ion implantation range distribution to estimate the profile of the damage energy S_D as a function of penetration depth x. A knowledge of $S_D(x)$ is equivalent to a knowledge of the density profile of atomic displacements. Experience suggests that the capability of conveniently calculating $S_D(x)$ will find many applications in the analysis of ion implantation phenomena. In particular, this code is expected to facilitate the phenomenological analysis of (a) ion-beam mixing effects in ion implantation (ion beam mixing is discussed in paper IVD in this report) and (b) damage-enhanced diffusion effects in ion implantation.

Sputtering. Wherever the cascade of knock-on atoms intersects the surface, an atom may leave the surface if its energy exceeds the surface binding energy (usually in the range 2-5 eV). This process of emission of atoms from the surface is called "sputtering," and the number of sputtered atoms per incident ion is called the "sputtering yield" (S). Sputtering is a significant factor for heavy implantation doses, which are common for metal targets, because sputtering (i) may have a substantial effect on the depth concentration profile of implanted ions and (ii) may seriously limit the maximum achievable concentration of implanted ions.

The sputtering yield depends on a number of parameters, including ion energy, species, flux, angle of incidence, target material, dose, crystal state, surface binding energy, and perhaps other parameters as yet unknown. The general nature of these dependences is as follows.

Ion Energy. The dependence of S on incident ion energy E_i (*Fig. 10*) may be understood qualitatively in terms of elastic collisions and the binding energy of a surface atom. A given target atom may receive a maximum amount of energy (determined by classical mechanics) from the incident ion and, if this energy is less than the surface binding energy, no sputtering can occur. Thus, a sputtering threshold energy (E_t) is expected. At higher energies, S rises with E_i because collisions involving less than the maximum energy transfer begin to contribute to the process. As E_i continues to increase, it eventually reaches an energy at which the rate of elastic energy transfer decreases (as in Fig. 5). The collision cascade near the surface subsides, leading to a decrease in sputtering. Although this simple picture qualitatively describes the actual behavior of S with respect to E_i, there are quantitative differences (which are not understood) between this simple picture and experiment (in both the threshold energy E_t and the subsequent variation of S).

Ion Species. As can be seen by an inspection of Fig. 5 a high-Z incident ion (in this case, iron) transfers a larger fraction of its energy via elastic collisions than a low-Z ion (in this case, nitrogen). Hence S increases as a function of Z_1 as illustrated by the measured values[20] of Fig. 11.

[19] W. A. Fraser and Irwin Manning, Radiation-Matter Interactions Branch, NRL.

[20] Adapted from H. H. Andersen and H. L. Bay, Radiat. Eff. **19**, 139-146 (1973); **13**, 67-74 (1972).

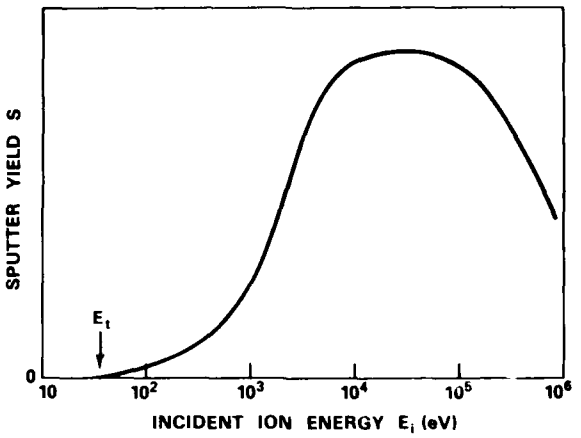

Figure 10. A schematic representation of the sputtering yield S as a function of incident ion energy E_i. The energy scale is for a "typical" case only; the scale for an actual case is a function of several parameters, including the ion species and target material. In particular, the threshold energy E_t is related to the binding energy of the surface atoms and to the maximum transferable energy in a single collision from classical (billiard ball) mechanics. The curve rises above E_t because collisions other than those transferring maximum energy begin to contribute. The rest of the curve generally follows the shape of the elastic part of the energy-loss rate (Fig. 5).

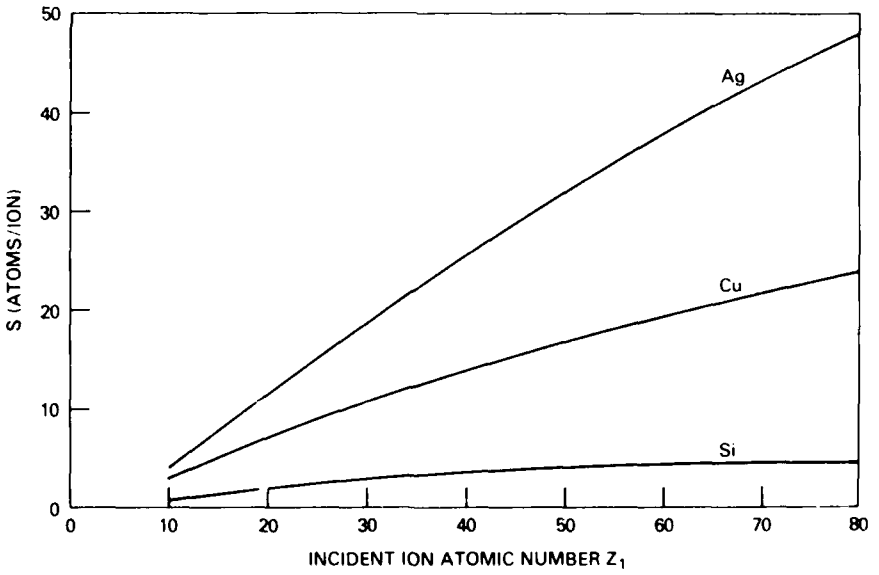

Figure 11. The sputtering yield S at normal incidence from polycrystalline copper and silver and amorphous silicon targets as a function of incident ion atomic number Z_1.[20] The incident ion energy is 45 keV in all cases. One may not interpolate to obtain curves for other target materials because the sputtering yield does not vary monotonically with Z_2; rather it depends more on the surface binding energy than on Z_2.

Angle of Incidence. As the angle of incidence θ (the angle between the incident-velocity vector and the normal to the surface) varies from zero, one expects S to be proportional to sec θ since, for a given instantaneous depth of the incident ion in the target the path length of the ion is proportional to sec θ. However, the multiple scattering implicit in the sputtering process complicates this simple picture: The sputtering yield actually[21] depends on $(\sec \theta)^x$, where x is slightly greater than one; and the precise dependence is a function of the incident and target atoms. This sec θ dependence breaks down for large values of θ because of the escape of indident ions from the surface. The dependence is qualitatively illustrated by Fig. 12. For single-crystal materials, the relationship between θ and channeling directions has a major influence on S.

Target Material. The sputtering yield depends on the mass of the target atoms because the energy transferred in a collision depends on this mass. But a more critical dependence is the approximately inverse proportionality between S and the surface binding energy, which depends on surface topography, grain characteristics, crystal plane and crystal axis orientation within the grain, and other surface conditions as well as atomic number and basic lattice constants.

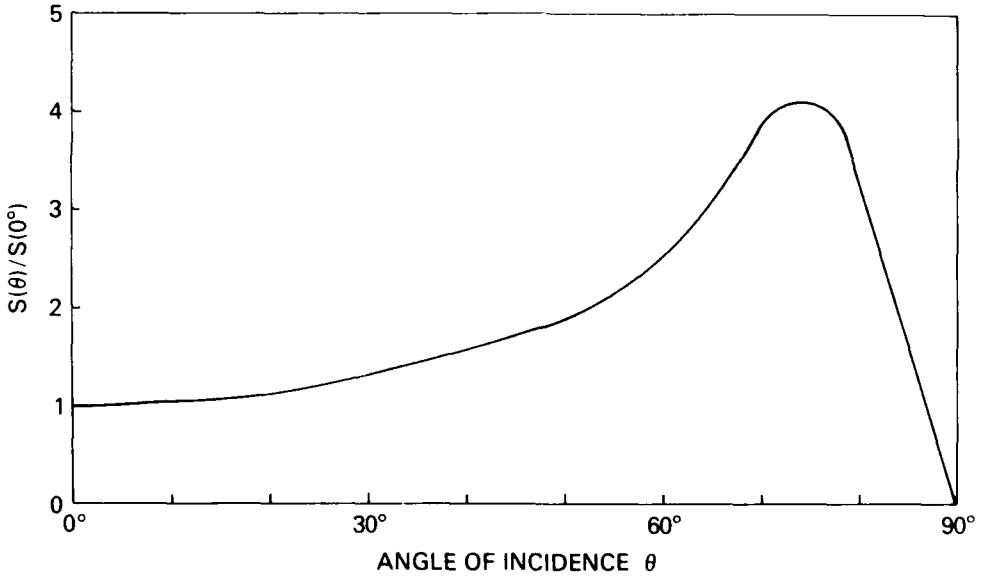

Figure 12. A schematic representation of the sputtering yield S as a function of the angle of incidence.[21] For angles below roughly 70°, the curve follows sec θ, approximately. At larger angles the curve shape is determined by the rate of escape of incident ions through the surface, and this factor is in turn determined by the elastic collision rate, the relative masses of ion and host atom, and surface topography.

[21] Adapted from K. B. Cheney and E. T. Pitkin, J. Appl. Phys. **36**, 3542-3544 (1965).

Dose. If the target atoms and incident ions are not the same species, then the composition of the surface changes as a function of time (or dose or fluence); so in order to predict the sputtering at any given time, one must take into account the near-surface composition at that time.

These dependences may be summarized as follows. The conditions that lead to large sputtering yields are

(i) a low value of target surface binding energy,
(ii) a high value of Z_1,
(iii) an intermediate value of E_i (about 100 keV), and
(iv) a high value of θ (but not more than about 70°).

Figure 13 illustrates some of these dependences and gives measured values of S for different ions incident on polycrystalline copper.[22] An example of the significance of the sputtering yield follows. From Fig. 13 we see that 50-keV argon ions striking polycrystalline copper, at normal incidence, exhibit a

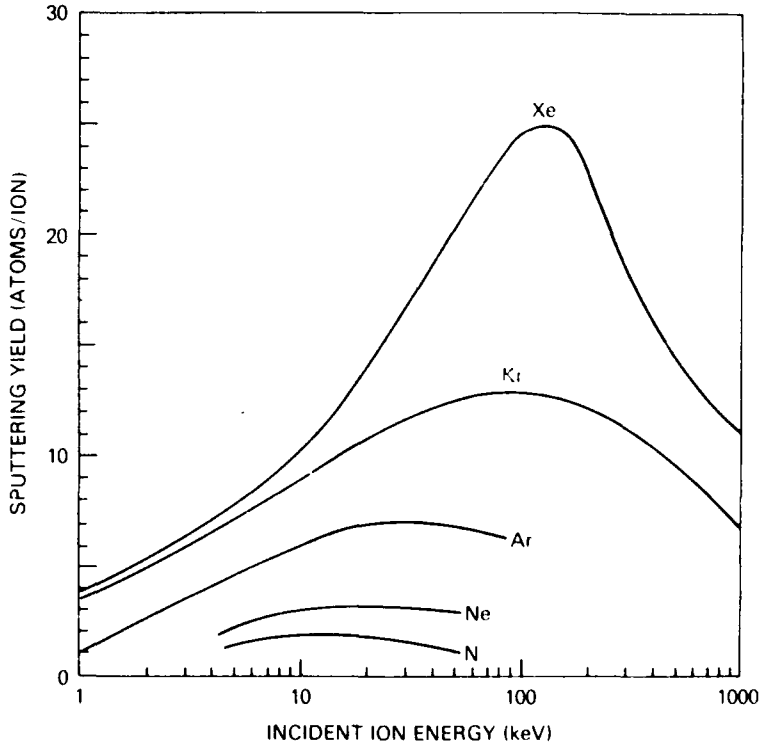

Figure 13. The sputtering yield (S) for a polycrystalline copper target as a function of incident ion energy E_i for various ion species at normal incidence. These curves have the same general shape as the elastic energy-loss curves of Fig. 5.

[22] Adapted from the data of reference 20 and O. Almen and G. Bruce, Nucl. Inst. Methods **11**, 257 (1961); G Dupp and A. Scharmann, Z. Physik **192**, 284 (1966); **194**, 448 (1966); and F. Keywell, Phys. Rev. **97**, 1611 (1955).

sputtering yield of about seven. Therefore for a fluence of 10^{17} argon ions/cm^2 on copper, about 7 x 10^{17} copper atoms/cm^2 (equivalent to 360 atom layers) are sputtered. Although this dimensional change is not measurable by ordinary instruments, it is several times the range of 50-keV argon ions in copper (95 atom layers), hence removes all of the atoms initially implanted if the implantation energy is held constant.

There are several beneficial effects of a small amount of sputtering during implantation. (i) The process tends to clean the surface being bombarded. (ii) Sputtering (under certain conditions) tends to polish the surface. (iii) As the surface erodes during bombardment, lower layers become exposed; so if one bombards long enough, the layer in which the initial ions were implanted is exposed. This effect can be an advantage when one is implanting for anticorrosion purposes where one wants a substantial concentration of implanted ions right on the surface. (iv) Surface analysis techniques can be used with sputtering to measure concentrations of elements as a function of depth. (v) Sputtering leads to a saturation concentration of implanted ions. The larger the fraction of implanted atoms in the target the more implanted atoms are themselves sputtered until eventually (after the erosion depth becomes a few times the original implantation depth) an equilibrium is reached at which one previously implanted atom is sputtered for each new atom that is implanted. If $S \gg 1$, then this equilibrium relative concentration of implanted atoms is 1/S, or 100/S atom percent. Although this effect may not always be deemed beneficial, it can be beneficial, for example, in smoothing out concentration fluctuations in the implantation of an object with a complex shape for which it is difficult to assure uniform irradiation. (A complicating consideration is that, if an object has a complex shape, resulting in different angles of incidence at different locations, then S is a function of location, and the equilibrium concentration is also a function of location.)

Although the *equilibrium* relative concentration of implanted atoms is 100/S atom percent, one can circumvent equilibrium and exceed the equilibrium value substantially by decreasing the incident ion energy as a function of time such that the newly implanted ions always come to rest in the same physical layer and by stopping the implantation process when the eroding surface is near or at this physical layer.

NRL Research on Sputtering. Because of the large number of parameters involved with sputtering, not all have been investigated adequately for general industrial application. For example, most research to date has involved single-element materials rather than mixtures, such as alloys. For these reasons NRL is engaged in a basic research program[23] of investigating the sputtering of multicomponent samples during the transition period between an initially unimplanted, unsputtered surface and a surface containing a steady-state distribution of implanted atoms. Most previous studies of this nature have concentrated on analysis of the target surface. Although the NRL project also involves examining the final target surface, the emphasis of the NRL project is on the sputtered atoms themselves because they reveal more information than the surface they leave behind. Sputtered atoms will be collected on catcher foils

[23]M. R. Weller, Materials Modification and Analysis Branch, NRL.

surrounding the targets, and these foils will be analyzed to obtain angular distributions for the sputtered species. It is anticipated that, even after a steady-state situation has been reached in the target, the angular distributions of different species will not be the same. Investigations of binary systems should give some indication of how various properties of the target atoms (mass, binding energies, etc.) affect the sputtering of multicomponent samples.

In another series of experiments (concurrent with the catcher-foil measurements) the light emitted by excited sputtered atoms will be monitored or measured according to intensity and wavelength. Such data will reveal changes in the total sputtering yields of the original target elements and of the implanted species as a function of implanted dose. This information will complement that obtained with the catcher-foil measurements. In addition, this technique permits the study of systems which cannot be easily studied with catcher-foil techniques but which are nevertheless important and of scientific interest.

Commercial Status and Future Outlook

The status of ion implantation in the semiconductor device industry is well established. With several companies manufacturing and servicing implantation machines, about 450 machines (worldwide) were engaged in production and research in 1979. But at that time the commercial application of ion implantation outside the semiconductor field was limited to a few instances in the United Kingdom.

Estimates of the production-line cost (depreciation, overhead, materials, and labor) of implanting metals depend on several assumptions (including the ion current available and the fluence needed) some of which vary (according to circumstances) by more than an order of magnitude. For a fluence of 10^{17} ions/cm^2 of an element such as chromium into a steel part (a typical dose for many nonsemiconductor applications) the cost is estimated to be the order of 10¢ per square centimeter at the 1980 state of the technology. This cost rate, which may decrease significantly as the technology advances, implies that the ion implantation of small or medium-size parts is cost effective where reliability is important or where the implantation substantially increases the time between replacements and where a substantial amount of labor is involved in the replacement.

Because research results in the late 1970s imply that ion implantation may have as promising a future in the modification of the chemical, optical, or mechanical properties of materials as in the modification of the electrical properties, it appears reasonable to expect that these commercial applications of ion implantation will occur during the early 1980s.

Section I.B

Ion Implantation Simulations with MARLOWE

G. P. Mueller[1] and M. Rosen[1]

[1]Radiation-Matter Interaction Branch
Radiation Technology Division
Naval Research Laboratory

This work was supported by the Office of Naval Research.

ION IMPLANTATION SIMULATIONS WITH MARLOWE

G. P. Mueller and Mervine Rosen

Radiation-Matter Interactions Branch
Radiation Technology Division

MARLOWE is a binary-collision simulation code developed by M. T. Robinson and I. M. Torrens[1] to study the effects of neutron and heavy ion irradiations on crystalline materials. The code models a crystal lattice and observes the collision histories of both the impinging particles and of each lattice atom they set in motion. After the irradiation, the code reports all changes in the lattice (vacancies, interstitials) and all particles that may have escaped the crystal.

The code is flexible both in the variety of initial conditions that it allows and in the forms of output that can be requested. MARLOWE operates most efficiently for knock-on energies between the displacement energy of lattice atoms at the low end and tens of keV at the upper end.

The latest version of MARLOWE has been converted and is available for use on the NRL Texas Instruments Advanced Scientific Computer. Tables I and II indicate the flexibility of the code by listing some of the input and output choices that are available.

The first calculation planned as part of the ion implantation program involves a study of the recoil implantation of boron in beryllium. In the experiment, a beam of boron particles is implanted into beryllium through a 10-nm layer of boron already deposited on the surface of the beryllium. Some of the boron atoms are driven into the beryllium by the boron beam particles.

The analysis with MARLOWE will be done in two stages. The first will consist of a run with a boron beam passing through a thin boron film. The output of this run will be a table of the number of beam and recoil ions at various angles and energies escaping the far surface of the thin film. A second run will be made in which the output of the initial run is used as a diffuse beam on a beryllium target. The output of this run will then list the final resting places of all of the boron recoils and boron beam ions in the beryllium. The damage done to the beryllium by the stopping particles will also be evaluated.

A comparison of the code calculations with the experimental results will assist in separating recoil implantation effects from diffusion due to the local melting effects at the boron-beryllium interface. The latter are not treated by the code.

[1]M. T. Robinson and I. M. Torrens, Phys. Rev. **B9**, 5008 (1974).

TABLE I. INPUT CHOICES

CRYSTAL STRUCTURE (cubic, diamond, etc.)
- single crystal
- polycrystalline
- amorphous

CHEMICAL ORDERING
- any specified amount of disorder

INITIAL VACANCIES

INITIAL INTERSTITIALS

SURFACES
- infinite solid
- semi-infinite solid
- thin film

TEMPERATURE (zero or finite)

CROSS SECTIONS
- various elastic and inelastic cross sections

SOURCE OF IRRADIATION
- *internal*
- external beam
  - choice of:
    - direction
    - beam divergence
    - target area
    - crystal surface

TABLE II. OUTPUT CHOICES

RANGE DISTRIBUTIONS
- histograms
- range moments (1st - 4th)

VACANCY AND INTERSTITIAL DISTRIBUTIONS
- separation pairings of vacancies and interstitials

SPUTTERING YIELD
- direction and energy of sputtered particles

REFLECTION AND TRANSMISSION OF BEAM

REPLACEMENT SEQUENCE DIRECTIONS

Section II.A

FRICTION AND WEAR REDUCTION OF BEARING STEEL VIA ION IMPLANTATION

C. A. Carosella,[1] I. L. Singer,[2] R. C. Bowers,[2]

and C. R. Gossett[1]

[1]Materials Modification and Analysis Branch
Radiation Technology Division

[2]Surface Chemistry Branch
Chemistry Division
Naval Research Laboratory

This work was supported in part by the Office of Naval Research and in part by Defense Advanced Projects Research Agency.

FRICTION & WEAR REDUCTION OF BEARING STEEL VIA ION IMPLANTATION*

C. A. Carosella and C. R. Gossett

Materials Modification and Analysis Branch
Radiation Technology Division

I. L. Singer and R. C. Bowers

Surface Chemistry Branch
Chemistry Division

Introduction

Work at Harwell[1,2] and NRL[3] has shown that the ion implantation technique can be used to significantly improve the lubricated sliding wear resistance of steels. Most work has concentrated on the effects of the implantation of nitrogen ions. Intense nitrogen ion beams are easily obtained and the nitrogen ions affect a number of surface sensitive mechanical properties of steels.[4] For example, sliding wear rates for nitrogen-implanted stainless steels, such as AISI 304, have been reduced by factors of twenty or more.[3] Reductions in sliding wear have also been found for the nitriding steel EN40B, annealed 440C stainless steel, and mild steel.[1,2] Other ions besides nitrogen, such as carbon, boron, titanium, and molybdenum, can also reduce lubricated sliding wear in these steels.[1,5] In general, the largest reductions in sliding wear from ion implantation have been found for the relatively soft stainless steels.

*This work was supported in part by DARPA.

[1] N. E. W. Hartley, G. Dearnaley, J. F. Turner, and J. Saunders, "Friction and Wear of Ion Implanted Metals," in Applications of Ion Beams to Metals, eds., S. T. Picraux, E. P. EerNisse, and F. L. Vook, Plenum Press, New York (1974) pp 123-138.

[2] G. Dearnaley and N. E. W. Hartley, "Ion Implantation into Metals and Carbides," Thin Solid Films **54**, 215-231 (1978).

[3] J. K. Hirvonen, "Ion Implantation in Tribology and Corrosion Science," J. Vac. Sci. Technol. **15**, 1662-1668 (1978).

[4] H. Herman, W. W. Hu, C. R. Clayton, J. K. Hirvonen, R. Kant, and R. K. MacCrone, "Modification of Mechanical Properties Through Ion Implantation," Ion Plating and Allied Techniques 79, CEP Consultants Ltd, UK (1979) pp 255-263.

[5] J. K. Hirvonen, C. A. Carosella, R. A. Kant, I. Singer, R. Vardiman, and B. B. Rath, "Improvement of Metal Properties by Ion Implantation," Thin Solid Films **63**, 5-10 (1979).

There is therefore a question of whether or not ion implantation can reduce the sliding wear of through-hardened bearing steels such as AISI 52100, M50, and 440C. This is certainly a relevant question because the demanding operating conditions of (high speed, low load) instrument bearings and (low speed, high load) engine bearings create wear, fatigue, and corrosion problems. Attempts have been made to alleviate these difficulties with various coating technologies, such as rf sputtering and chemical vapor deposition. However, coating techniques (i) have a degree of inherent adhesion problems, (ii) can change the temper and dimensionality of parts, and (iii) require relatively expensive machining as well as further heat treatment.

This paper describes experiments for reducing friction and wear in AISI 52100 (martensitic) bearing alloy steel with ion implantation. AISI 52100 steel is the most common bearing alloy presently used for aeronautical applications. It is through-hardened martensitic steel with a Knoop hardness number (KHN) of 750 kg/mm^2 at room temperature. Applications of this steel are limited, however, to noncorrosive environments and to temperatures below 175°C, since the steel rapidly loses its hardness above this temperature. The nominal alloy composition (atomic per cent) of 52100 is Fe/93.2, C/4.48, Cr/1.50, Si/0.48, and Mn/0.34.

Experimental Procedure

Implantation. Implantation of all AISI-52100 steel samples was done with a modified Model 200-20A2F Varian/Extrion ion implanter. The ion source is a hot cathode arc discharge type. Producing ion beams for gaseous elements is standard, and ion beams up to 1 mA are obtainable. For metal ion beams, such as titanium, a chlorination technique is employed. Chlorine gas is passed through fine titanium powder contained in a graphite oven within the source chamber, producing titanium chlorides, which volatilize at the high source temperature and are subsequently ionized. Ion beams intensities of about 200 μA of Ti^+ are routinely obtained.

Both flat and cylindrical 52100 samples were implanted in this work. The 52100 steel flats were water cooled and were kept near room temperature (<50°C) during implantation. The 52100 steel cylindrical samples were rotated during implantation and their temperature stayed under 150°C during the period of implantation (2-5 hr). The ion beams were electrostatically scanned over the samples, with average target currents the order of 50 $\mu A/cm^2$. The target chamber was cryogenically pumped and pressures of about 5×10^{-7} torr are typical during implantation.

A number of different elements were implanted in the 52100 steel, and the implantation parameters are summarized in Table I. These implantation parameters give gaussian distribution profiles, usually skewed toward the surface because of sputtering effects, with the peak of the distribution in the first 50-100 nm of the 52100 steel. The peak concentrations are about 30 atomic percent.

Table I. Implantation parameters for friction and wear experiments. The implants marked with an asterisk (*) were for the ball-on-cylinder wear experiments.

Element	Energy (keV)	Fluence (10^{17}/cm^2)
Ti	190	4.6
B	35	2.3
C	40	2.3
N	46	2.3
P	40	2.3
S	105	4.0
Mo	150	2.0
Ti*	150	2.0
N*	75	2.0

Friction and Wear

Three types of apparatus were used to determine friction and wear: a "stick-slip" machine, a pin-on-disk geometry machine, and a ball-on-cylinder geometry machine. The first apparatus, which was used to measure friction, utilizes a sphere sliding on a plane surface (platen). The platens used in these studies were 1.9-cm (0.75 in.) diameter 52100 steel disks, which were lapped and polished. The final polishing was done with a 3-μm diamond paste suspended in lapping oil. The surface had a mirror finish, but microscratches were easily visible with an optical microscope at a magnification of 1100. Surface roughness as measured with a profilometer was less than 0.025 μm (< 1 μin.). After being polished, those specimens were treated with a corrosion-prevention surface coating and stored in a desiccator. They were cleaned by solvents before implantation, then retreated and kept in a desiccator. Just prior to the friction measurements the disks were recleaned with benzene and 2-propanol. The sliders were 1.27-cm (0.5-in) diameter spheres of 52100 steel. The surface roughness was 0.025 μm (1 μin.). These sliders were cleaned by refluxing benzene in a Soxhlet extractor.

The slider in the "stick-slip" apparatus is attached to an elastically restrained friction arm, and the disk is clamped to a sliding table so that the disk moves under the steel slider. Two pairs of resistance strain gages, bonded to the arm, measure the normal and tangential forces (load and friction).

Wear rates were determined with the pin-on-disk and with the ball-on-cylinder apparatus. The former used the same disks studied in the "stick-slip" machine. The "pins" were the same 52100 steel spheres as used in the friction studies, loaded with a force of 9.8 N. The disks were rotated at 20 rpm resulting in velocities the order of 1.5 cm/sec. These conditions should produce a boundary lubrication condition (i.e., only monomolecular lubricant coverage, not sufficient for hydrodynamic or elastohydrodynamic lubrication). Hexadecane was chosen as the lubricant in these studies. This material is a well defined, easily purified, and relatively uncomplicated molecule, $CH_3(CH_2)_{14}CH_3$, with a melting point just below room temperature. It is a relatively ineffective boundary lubricant because it has no polar end group and therefore cannot form a close-packed, solid-type, monomolecular film on the solid surface that is characteristic of an effective boundary lubricant. Thus it will permit a wear rate that is measurable in a reasonable time period. With an effective boundary lubricant, the wear rate may be too slow; with no lubricant the effect of ion implantation may be obscured

by the catastropic wear. Measurements were made in air and in a nitrogen environment. An unbonded resistance strain gage was used to measure friction. Wear on the upper (stationary) sphere was found by periodically measuring the diameter of the circular wear scar on the sphere and calculating the volume, whereas the wear track on the disks were examined in several regions with a profilometer. Since the slider and disk have the same hardness, their wear rates should be comparable. Both slider and disk were cleaned by solvents before each measurement and then relubricated for the next test period.

Finally, experiments were performed with a ball-on-cylinder apparatus to observe the initial (run-in) portion of the wear curve. Wear tests with the 3.2-cm (1.25-in.) races were conducted by adapting a lathe. In these experiments the slider was a 1.27-cm-diameter unimplanted 52100 steel sphere, which was held against a rotating 3.2-cm (1.25-inch) race under a load of 19.6 N. The implanted race rotated partially submerged in a bath of synthetic polyester turbojet engine lubricant (MIL-L-23699). Friction was not measured with this apparatus. The rotational speed was 400 rpm, corresponding to a linear velocity of 66 cm/sec. Electrical resistance measurements indicated that boundary lubrication conditions predominated.

Analytical Techniques

Two complementary analytical methods were employed to determine the distribution of elements in the 52100 steel after ion implantation; these were Auger electron spectroscopy combined with sputter etching and nuclear reaction analysis. The Auger analysis was used to determine the distribution of Fe, Cr, C, O, and implanted Ti. It also yields chemical information, used to determine the chemical state of C and implanted Ti. The nuclear reaction profiling technique quantifies the concentration profile of the implanted Ti and helps to confirm the Auger C data.

Auger Analysis. Auger analysis was performed in a UHV chamber equipped with a Perkin-Elmer (PHI) Model-545 Auger microprobe, an ion gun, a Ti sublimator and liquid nitrogen cooled cryopanels. The electron gun was operated at 2 kV, at currents from 0.6 to 6 μA, and the electron beam was scanned over a spot size of 50 μm to reduce the intensity. Auger derivative spectra were recorded either directly, with a modulation amplitude of 3 eV, or by a peak-height recording multiplexer with a 6-eV modulation amplitude.

The ion gun was operated in an argon atmosphere (about 5×10^{-5} torr) with a beam of 2-keV Ar^+ ions, at selected current densities between 2 and 30 $\mu A/cm^2$. Depth profiles were recorded during ion milling with Ti sublimators operating and cryopanels cooled to liquid-nitrogen temperature. These procedures reduced contamination of ion milled surfaces by residual gas vapors to below detectable levels.

Quantitative analysis was accomplished with the usual normalization procedures.[6] The normalization constants (sensitivity factors, S) were obtained from the PHI Auger handbook[7] and verified for a variety of alloy steels and carbide powders. Only the value for carbon differs from the handbook value, which was established for a graphite-like

[6] C. C. Chang, "General Formalism for Quantitative Auger Analysis," Surface Science **48**, 9-21 (1975).

[7] "Handbook of Auger Electron Spectroscopy," 2nd edition, L. E. Davis, ed., Physical Electronics Industries, Eden Prairie, MN (1976) p. 13.

carbon lineshape and not a carbide-like lineshape. Sensitivity factors are listed in Table II for the principal Auger spectra lines used to characterize each species (note the shorthand notation used, e.g., $Ti_{385\ eV}$). With these values, Auger analysis of unimplanted 52100 steel gave Fe/95 Cr/1.5 C/3.4, in good agreement with the expected Fe/93.2, Cr/1.5, C/4.5 atomic percent concentration.

Table II. Sensitivity factors (S) for Auger peak-to-peak amplitudes acquired at a modulation amplitude of 3 eV.

Auger line	$Fe_{650\ eV}$	$Cr_{530\ eV}$	$Ti_{385\ eV}$	$C_{272\ eV}$
S	0.17	0.34	0.45	0.47

The depth scale for the Auger profiles was established by Michelson interferometry. Auger depth profiles were taken near the edges of partially masked steel surfaces. The depth of an ion-milled step was later measured with a Michelson interferometer to an uncertainity of about ±5 nm. This procedure gave the depths at which several composition profiles had been terminated and, since no differences were observed in the sputter rates of Ti^+-implanted and unimplanted steels, the depth scale was taken to be proportional to milling time.

Nuclear Reaction Profiling. A resonant nuclear reaction technique[8] was used to determine the profile of the concentration of implanted Ti as a function of depth in the sample. The narrow 1007-keV resonance of the $^{48}Ti(p,\gamma)^{49}V$ reaction provided a characteristic identifying spectrum for the resonance in an experiment in which the gamma rays were detected with a high-resolution Ge(Li) detector. The gamma-ray yield from the resonance was measured at a number of different energies above the resonance of the incident H ion beam, which results in the resonance occurring at different depths below the surface of the sample. From the known energy loss relationships for the incident H ions, the depth scale may be calculated by taking into account the observed changes in the composition of the sample with depth. In addition to the observed titanium profile, the carbon profile observed in the Auger measurements was also introduced into the depth determination. This inclusion produced about a 5% change in the depth scale at the peak compared to that for only a carbon concentration present in the basic AISI 52100 steel diluted by the titanium implant.

The distribution of C in 52100 steel is analyzed by the use of the nonresonant $^{12}C(d,p)^{13}C$ nuclear reaction. This reaction is not as depth sensitive as the resonant reaction used to determine the titanium profile, and it was thus not possible to determine whether the observed excess of carbon was only on the surface or was distributed in the very near surface region. This problem introduces some uncertainty into the results because, in the relatively poor accelerator vacuum conditions used here, the buildup of carbon surface layers during analysis is possible even under the cryotrap conditions used in these experiments.

[8] C. R. Gossett, "A Method for Determining Depth Profiles of Transition Elements in Steels," Nucl. Instr. Methods (1980), to be published.

Friction and Wear Results

Kinetic Coefficient of Friction. Table III summarizes the kinetic coefficient of friction (μ_k) measured for a 52100 ball sliding on an implanted 52100 disk. The coefficient μ_k was determined in air at 23°C and at a sliding velocity of 0.01 cm/sec. A normal force of 9.8 N (1 kg) was used, producing a peak Hertzian pressure of 0.57 GPa (83,000 psi). Multiple unilateral traverses were made over the disks. The first traverse was 5 mm in length and subsequent traverses were made over the center 3 mm of the first traverse without rotating the slider. Measurements of μ_k were made either on an unlubricated surface or in the presence of hexadecane. Friction coefficients vary by ± 0.05 along a traverse. When stick-slip occurs, however, coefficients can vary by as much as ± 0.2.

Table III. Kinetic coefficient of friction (μ_k) for an unimplanted 52100 steel ball against an implanted 52100 steel disk. The entries marked with an asterisk (*) are average coefficients of friction when stick-slip occurs. Entries marked with a dagger (†) represent the value of μ_k after five traverses.

	Dry		Hexadecane	
Implanted Ion	1st traverse	10th traverse	1st traverse	10th traverse
None	.60	.65†	.16*	.13*
Ti	.18	.32	.15	.18
Ti+C	.23	.32	.15	.11
C	.75	.54†	.14*	.15*†
Mo	.23	.73	.17	.15
S	.36	.45	.19*	.14
Mo+S	.26	.54	.19	.16
B	.3*	.66	.16*	.14*
N	.71	.66	.17*	.16
P	.20	.69	.17	.17

As shown in Table III, the effect of the implantation of titanium, even after ten traverses, is a reduction of μ_k by about a factor of two when no lubricant is present. See also Fig. 1. (Measurements at 19.6 N (2 kg) normal force give similar results.) Ti + C implants do equally well, but C alone has no reducing effect. The other elements listed, except for S, show little lasting effects, with μ_k returning to unimplanted values after a few traverses. (Multiple traverses not only show whether the implantation effects are long lasting but also tend to remove the complications of any lubricating surface contaminants left behind after solvent cleaning.)

Values of μ_k for the hexadecane lubrication experiments are more uniform than for the no-lubrication experiments, tending to be about 0.16 for all elements; μ_k exhibits stick-slip behavior. The Ti implant eliminates stick-slip behavior, as is shown in Fig. 1. Generally stick-slip behavior occurs whenever the static and kinetic coefficients of friction differ by more than a factor of two.[9] Under the low-speed motion of these friction experiments (0.01 cm sec^{-1}) adhesion can take place at asperities, increasing the static coefficient of friction. The ion implantation of Ti reduces this microadhesion and equalizes the static and kinetic coefficients of friction, eliminating stick-slip behavior.

[9] E. Rabinowicz, "The Nature of the Static and Kinetic Coefficients of Friction," J. Appl. Phys. **22**, 1373-1379 (1951).

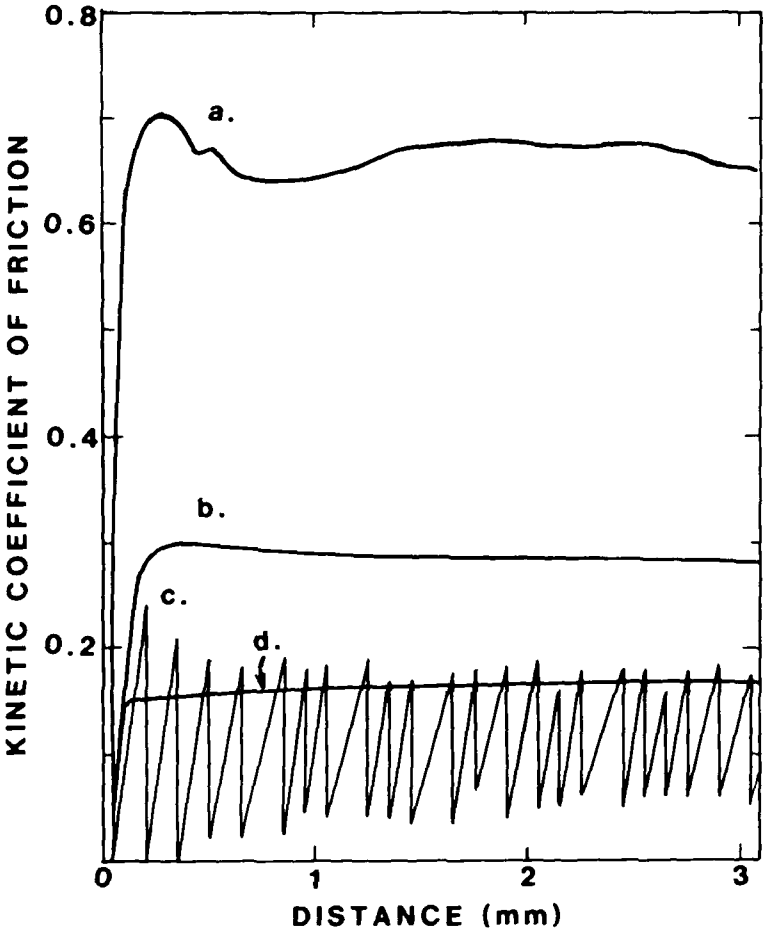

Figure 1. Kinetic coefficient of friction vs. sliding distance for a 52100-steel sphere on a 52100-steel platen for the following conditions: (a) dry, unimplanted, five traverses; (b) dry, Ti-implanted, 10 traverses; (c) hexadecane lubricated, unimplanted, five traverses; (d) hexadecane lubricated, Ti-implanted, five traverses. Sliding velocity is 0.01 cm/sec in all cases.

Pin-on-Disk Wear. Results of the 52100-pin-on-52100-disk wear experiments are shown in Fig. 2. Conditions are similar to those for the hexadecane-lubrication friction measurements except that velocities are typically about 1.5 cm/sec. The "pins" are steel spheres from the same batch used for the friction measurements, and the disks are the same as used for the friction measurements. The wear rate for the unimplanted samples increases rapidly with sliding distance, with wear commencing almost immediately. Friction measurements during sliding wear show a rapid increase in friction from initial values of about 0.15 to about 0.4 as severe wear commences. Adhesion between the sphere and disk manifests itself by the oscillation in friction for each revolution of the sphere on the disk. The oscillations grow larger as the friction increases and wear becomes severe. Wear on the boron-implanted disk is very similar to that of the unimplanted disk and is shown in Fig. 2. Wear for unimplanted disks is the same whether done in air or in a nitrogen atmosphere.

The wear curve for the B-implanted and unimplanted samples was reproducible well within the factor-of-two variations in these types of experiments. However the wear curve for the Ti-implanted samples shown in Fig. 2 is not reproducible in the sense that the onset of wear is extremely variable. For different experiments, wear can commence at about 250 m as shown but also as soon as about 150 m and as late as about 550 m. This behavior may be due to the random nature of the wear process through a thin wear-resistant layer. The depth of the wear scar on the Ti-implanted disk, as measured with a profilometer, indicates that severe wear begins when the wear scar is about 0.1 μm deep, which is in qualitative agreement with the depth of the Ti implant. Friction measured during the wear process on the Ti-implanted disk has a vastly different behavior than for the unimplanted disks. Initial values of about 0.1 fall to values of about 0.07 during the period when no appreciable wear takes place. The friction is low and steady with very little oscillation as the disk revolves. Friction does increase and, once severe wear sets in, behaves as observed on the unimplanted disks.

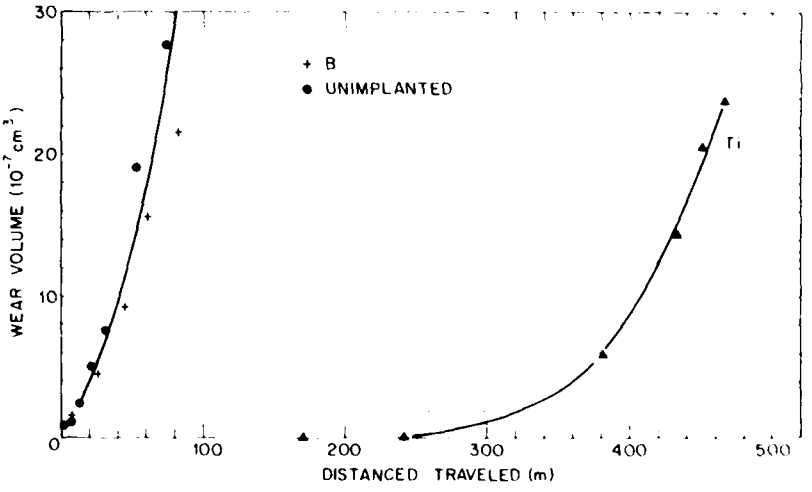

Figure 2. 52100-pin-on-52100-disk wear experiments. The arrows beside the Ti implantation wear curve indicate that the onset of severe wear is highly variable but always occurs well after severe wear begins for the boron implanted and unimplanted samples.

Ball-on-Cylinder Wear. Figure 3 shows the results of the 52100-ball-on-52100-cylinder wear experiments. The wear is much less severe for these experiments than for the pin-on-disk experiments because here an excellent boundary lubricant is used (MIL-L-23699). These data illustrate the "run-in" region of the wear process. Measurements were done in air at 23°C with a normal load of 19.6 N (2 kg), giving a Hertzian pressure of 0.81 GPa (117,000 psi).

Wear rates for N-implanted races and unimplanted races differ by less than a factor of two, which is within the data reproducibility for a typical wear experiment. Once again, though, Ti and Ti+C implants reduce wear rates by a factor of five or more.

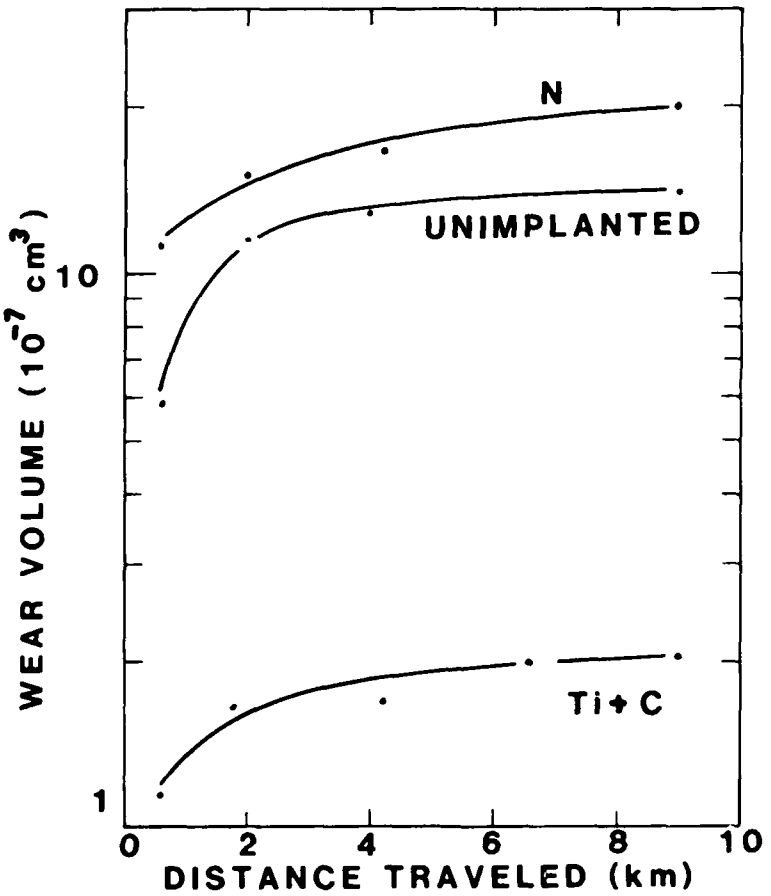

Figure 3. 52100-ball-on-52100-cylinder wear experiments show the "run-in" part of the wear curve. Wear rates for the unimplanted and N-implanted samples are not significantly different.

Composition of Ti-Implanted 52100 Steel

Our experiments show that Ti implanted into 52100 steel does significantly reduce friction and wear. There follows an analysis of the composition of Ti-implanted 52100 steel to help understand the reasons for these improvements in tribological properties.

Auger Analysis. A composition vs depth profile of a Ti-implanted 52100 steel disk is shown in Fig. 4. In addition to Ti, the profile shows a large, unexpected, concentration of subsurface carbon. Appearing directly beneath the oxide layer, the C concentration first reaches a maximum of about five times the bulk value of 4 at.%, then tails off to near bulk value at a depth of about 100 nm. The $C_{272\ eV}$ profile actually appears to dip to a minimum before leveling off. We do not yet know whether this dip reflects a gradient in the C concentration or is an Auger artifact associated with ion milling through a rapidly changing interface. $C_{272\ eV}$ profiles similar to the one in Fig. 4 have also been observed in low carbon AISI 304 stainless steel (Fe, Cr/18, Ni/8) and in pure Fe (< 20 ppmC). The latter observation suggests that the subsurface C (above background) in the Ti-implanted 52100 steel samples diffuses in from the vacuum system during implantation. There is no evidence of such C diffusion into 52100 steel during implants of N, Mo, and S.

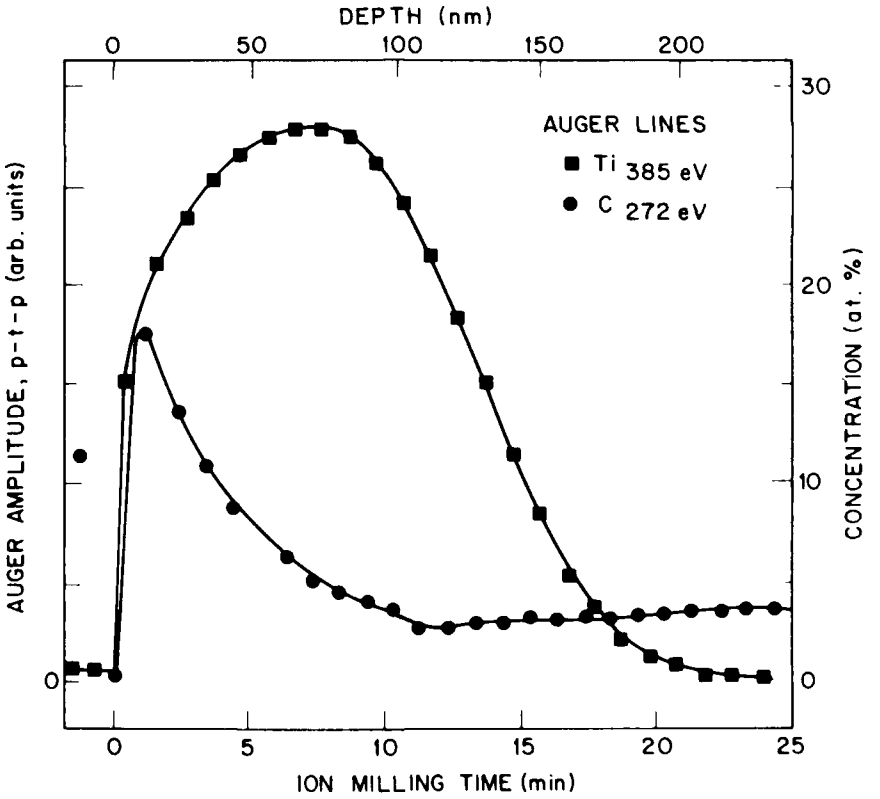

Figure 4. Concentration profiles of Ti and C from Auger analysis with ion beam milling.

Auger line-shape analysis has been used to infer the chemical identity of titanium and carbon in the implanted 52100 steel. There are three very thin layers on the implanted 52100 steel. The surface was covered by a carbonaceous overlayer. Under the carbon layer was a very thin Fe_2O_3 layer, and under this was an equally thin TiO_2 layer. The iron oxide was identified by the $Fe_{50\ eV}$ lineshape and the TiO_2 by the $Ti_{385\ eV}$ and $Ti_{420\ eV}$ lineshapes.[10] The total thickness of the two oxide layers is 2-3 nm, about the thickness of oxides found on polished surfaces of steels. The carbon, which virtually disappeared in the oxide layer, reappeared beneath it in the form of titanium carbide, as identified by the $C_{272\ eV}$ lineshape. Titanium carbide was also identified from the $Ti_{385\ eV}$ and $Ti_{420\ eV}$ lineshapes.[11] As the carbide disappeared, the Ti lineshape became more metal-like.

Semiquantitative concentrations from the $Ti_{385\ eV}$ and $C_{272\ eV}$ data are given by the ordinate scale in Fig. 4. This scale was based on a single sensitivity factor of 0.45 for $Ti_{385\ eV}$ and was found to agree with peak-height analysis of TiC powder. Carbide concentration can be read from the same scale since sensitivity factors for $C_{272\ eV}$ and $Ti_{385\ eV}$ are virtually the same. The concentrations of Ti are accurate to ± 10% at the depths where the $Ti_{385\ eV}$ lineshape is that of a titanium carbide. But, as just described, the $Ti_{385\ eV}$ lineshape varies from surface to bulk. These changes, while useful for chemical identification, make it difficult to quantify the Ti concentration throughout the 52100 steel.

Nuclear Reaction Analysis. The results of a second method of profiling 52100 steel implanted with 4.6×10^{17} ^{48}Ti atoms/cm^2 at 190 keV are shown in Fig. 5. The data indicate a maximum concentration of titanium of about 29 ± 3 at.% occurring in a broad peak centered at about 40 μg/cm^2. The peak is asymmetric with a drop-off to a surface concentration of about 22 at.%. The shape of the profile indicates that significant sputtering has occurred in the implantation of the titanum, but also that the fluence was less than that required for saturation of the sputtering. Integration of the Ti concentration in the depth profile indicates that 3.0×10^{17} Ti atoms/cm^2 are retained in the sample, implying that about one-third of the implanted titanium was lost in the sputter erosion of the surface.

[10] J. S. Solomon and W. L. Baun, "Molecular Orbital Effects on the Ti LMV Auger Spectra of TiO and TiO_2," Surface Science **51**, 228-236 (1975).

[11] N. K. Sharma and W. S. Williams, "An Auger Analysis of Substrate-Layer Interactions in the Chemical Vapor Deposition and Activated Reactive Evaporation of TiC," Thin Solid Films **54**, 75-83 (1978).

The depth scale of Fig. 5 is given in terms of $\mu g/cm^2$ determined directly from the measured energy loss in terms of the concentration of the constituents and their stopping powers, which are known to better than 10-15%. To convert to a linear scale of depth for comparison with Auger measurements requires assumptions as to the density in the implanted region. The simplest assumption is to take a uniform density (p=7.84 gm/cm^3) which would place the Ti peak, measured at 40 $\mu g/cm^2$, at a depth of 51 nm. Other assumptions of a variation in density of the implanted region with variation in Ti and C concentrations place the Ti peak at depths ranging from about 51 nm to 65 nm. The depth values obtained by the resonance nuclear reaction profiles appear to be somewhat less than those obtained by the Auger measurements, but otherwise the agreement in shape and concentration is excellent.

The $^{12}C(d,p)^{13}C$ reaction was used to confirm the Auger results of excess carbon in Ti-implanted 52100 steel. Comparison of Ti-implanted and unimplanted samples did show an excess of C at or near the surface for the Ti implanted 52100 steel. The measured fluence was 4.07×10^{16} C atoms/cm^2, which is two-thirds as large as detected in the Auger measurements.

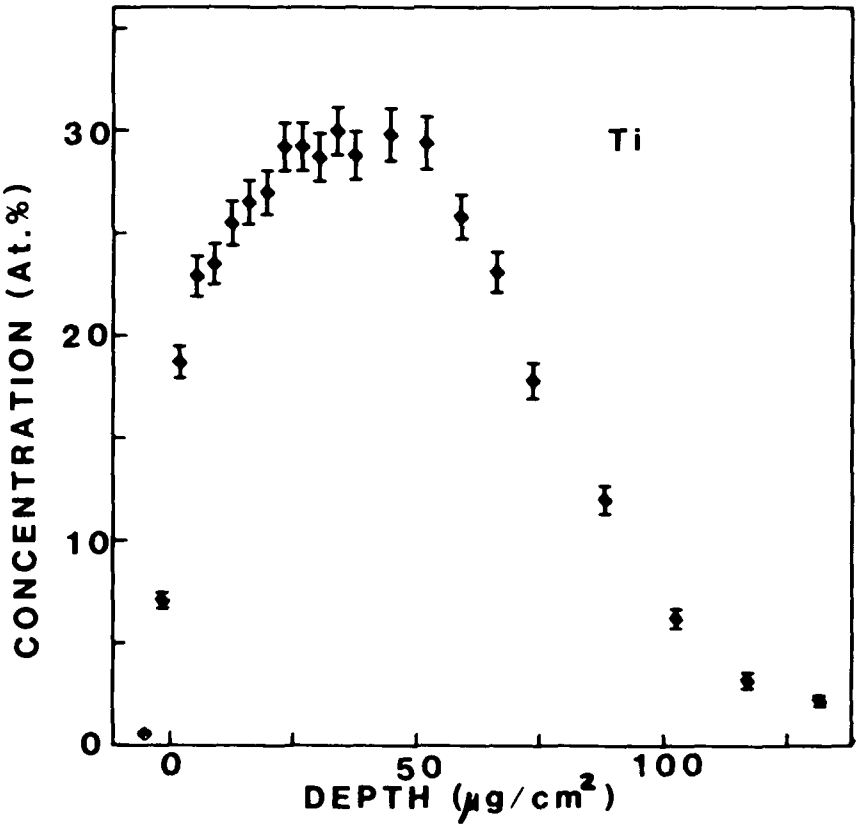

Figure 5. Profiling of Ti with the nuclear reaction $^{48}Ti(p,\gamma)^{49}V$.

Discussion

We have shown that the tribological properties of a through-hardened bearing steel, AISI 52100, can be improved with a high-dose implantation of Ti ($4.6 \times 10^{17}/cm^2$ at 190 keV). Ti implantation reduces the kinetic coefficient of friction, μ_K, by more than one half for the dry steel-on-steel case, and eliminates stick-slip behavior for the hexadecane-lubrication case. Lubrication sliding wear data show large reductions in wear which lasts until a thin surface layer (about 100 nm) is penetrated.

The Auger and nuclear reaction depth profiling analyses provide some clues as to the cause of these improved friction and wear characteristics. They show that the implantation of 4.6×10^{17} Ti ions/cm^2 at 190 keV into 52100 steel has produced a 22-30 at.% concentration of Ti from the surface to a depth of about 100 nm. As a result of the Ti implantation, $4\text{-}6 \times 10^{16}$ excess carbon atoms/cm^2 are present in the near surface. C concentrations range from about 20 at.% at the surface down to the bulk value of 4 at.% at about 100 nm. Furthermore Auger lineshape analysis indicates that the titanium is predominantly in the form of titanium carbide in the region of excess carbon concentration. Knapp, Follstaedt, and Picraux[12] have observed the same phenomenon of C-gettering in Ti-implanted high-purity Fe. They show that an amorphous surface is formed which is composed of Fe, Ti, and C. In their work, an amorphous layer is produced for 2×10^{17} Ti/cm^2 implanted at 190 keV with C concentrations of about 10 at.% concentration and resultant Ti concentrations of about 20 at.%. The similarity of their results with those presented here stongly suggests that a thin amorphous layer is reducing friction and wear in the Ti-implanted 52100 steel.

In addition, corrosion resistance may be enhanced with production of this amorphous layer as a result of Ti ion implantation. Wang *et al.*[13] show that ion implantation of 2×10^{17} Ti atoms/cm^2 at 55 keV improves the corrosion resistance of M50 bearing steel. The corrosion resistance is enhanced more than might be expected from electrochemical theory alone. Thus, it apears that ion implantation of Ti into bearing steel can beneficially improve corrosion as well as friction and wear.

Acknowledgement

We would like to thank J. K. Hirvonen for his continuous guidance and assistance during all phases of this work.

[12] J. A. Knapp, D. M. Follstaedt, and S. T. Picraux, "Amorphous Surface Layers in Ti-Implanted Fe," Materials Research Society, Cambridge, MA, 26-30 November 1979.

[13] Y.-F. Wang, C. R. Clayton, G. K. Hubler, W. H. Lucke, and J. K. Hirvonen, "Application of Ion Implantation for the Improvement of Localized Corrosion Resistance of M50 Bearing Steel," Thin Solid Films **63**, 11-18 (1979).

Section II.B

SURFACE HARDNESS AND ABRASIVE WEAR RESISTANCE OF ION-IMPLANTED STEELS

R. N. Bolster[1] and I. L. Singer[1]

[1]Surface Chemistry Branch
Chemistry Division
Naval Research Laboratory

This work was supported by the Office of Naval Research.

PREPRINT NO. 80-LC-8B-3
ASLE PREPRINT

Surface Hardness and Abrasive Wear Resistance of Ion-Implanted Steels

ROBERT N. BOLSTER (Member, ASLE) and IRWIN L. SINGER
Naval Research Laboratory
Washington, DC 20375

The hardnesses of nitrogen-implanted steel surfaces have been measured with an abrasive wear technique capable of characterizing surface layers as thin as 25 nm. Treated steel disks and reference disks were abraded with 1-5 μm diamond, and relative wear resistances were calculated from the mass losses. Surface hardness was obtained from a relationship between wear resistance and hardness.

The surface of a hardened and tempered carbon steel implanted with nitrogen ions (10^{17}/cm²) was significantly harder than with other treatments including quench hardening and nitriding. The hardness decreased to the bulk value over a depth corresponding to the initial implantation depth.

Nitrogen-implanted stainless-steel surfaces wore faster than unimplanted ones, possibly due to interference with transformation hardening which normally occurs during wearing. This "softening" effect persisted to depths several times the depth of implantation, and may help to explain the reduction of sliding wear produced by the implantation of stainless steels. Analyses by Auger electron spectroscopy indicated nitrogen migrated toward the bulk during wear.

Titanium implanted in stainless steel (4.6×10^{17} ions/cm²) produced a very hard surface with more than 10 times the abrasive wear resistance of the bulk metal.

INTRODUCTION

The resistance of steel surfaces to sliding wear can be greatly increased by implanting certain elements in the surface with a high-energy ion beam. For example, implantation of nitrogen ions into stainless steels has been shown to reduce the lubricated sliding wear rate by factors of up to 100 (1), (2). The observed increase in wear resistance has been attributed to the ability of nitrogen to harden steel surfaces (3). To study these effects, a technique for measuring the hardness of implanted layers was needed. Penetration techniques using diamond indenters sample too deeply into the surface (0.2 to 2 μm) to accurately measure the hardness of the implanted layer, which is typically only 0.1 μm deep. Therefore, an abrasive wear technique, akin to scratch-hardness testing (4), (5), was used.

Hardness has been correlated with abrasion resistance for a wide variety of metals and alloys (6), (7). Most such abrasive wear experiments have been done with large abrasive particles, 20 μm and greater, which penetrate several micrometers into the surface. In the present experiments, abrasives on the order of one micrometer in size were used to limit the wear process to the very thin layers of interest. The correlation between hardness and relative wear resistance with micrometer-size abrasives was verified with carbon steel and used to determine the hardness of implanted layers in stainless and carbon steels.

EXPERIMENTAL

Wear Studies

The abrasive wear technique was similar to that developed by Rabinowicz to study the relative effects of hardness on abrasive wear (4), (5). The alloys studied were in the form of disks, 12.7 mm in diameter and 2.8 mm thick. As shown schematically in Fig. 1, nine disks, three in each of three holders of equal mass, were abraded for a given pe-

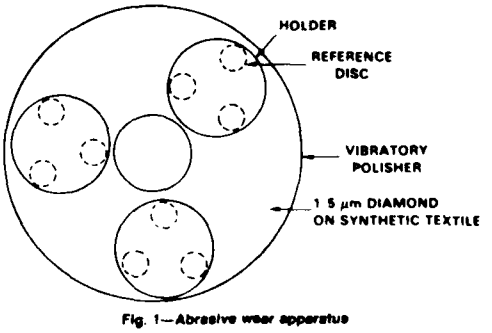

Fig. 1—Abrasive wear apparatus

Presented as an American Society of Lubrication Engineers paper at the ASME ASLE Lubrication Conference in San Francisco, California, August 18-21, 1980.

riod in a vibratory polisher on a nonwoven synthetic textile lap charged with diamond powder (1 to 5 μm) in paraffin oil. The atmosphere was air dried to a frost point of 200 K. The disks were then ultrasonically cleaned, rinsed and dried, and their mass losses were determined by weighing them with microgram precision. Each holder held at least one reference disk, and the relative wear resistance (RWR) of a modified (implanted or hardened) disk was calculated as the inverse of the wear rate of the modified disk normalized to that of the reference disk. Wear depth was calculated from the mass loss, area and density of each disk. Each μg of loss corresponded approximately to a depth of one nm. Wear depths thus could be determined with an uncertainty of a few nanometers, allowing wear rates to be determined with reasonable precision for layers as thin as 20–25 nm.

Sample Preparation

The carbon steel disks were prepared from a single bar of low-alloy carbon tool steel (similar to SAE 1095). After austenitizing at 1080 K under argon, they were quenched in oil. Three disks were tempered for an hour at 770 K, and three at 570 K. After being ground to their final thickness, the disks were smoothed by metallographic fine grinding and polishing procedures. The stainless steel disks were made from AISI-type-304 alloy and similarly ground and polished. Knoop hardness measurements were made at several radii on the disks and with various loads to ensure that they were uniform in hardness. The data reported here were obtained with a load of 2 kg on the indenter.

The surface finish on the disks, before implantation, was that achieved by lengthy polishing in 1–5 μm diamond. Polished disks were then implanted with 80 keV N_2^+ molecular ions (i.e., 40 keV N^+ ion) in the Naval Research Laboratory's 200 keV implanter. Average current densities of the rastered ion beam were in the range 3–5 μA/cm². The temperature of the disks might have risen 100–200 K from the prolonged exposure (~ one hour) to the ion beam. During implantation, the pressure in the target chamber was kept at 6×10^{-5} Torr.

Titanium implantation was done with a model 200-20A2F Varian Extrion ion implanter equipped with a hot cathode arc discharge source. The beam energy was 190 keV and the average current density 5 μA/cm². The chamber pressure was 5×10^{-5} Torr, and the samples were mounted on a water-cooled substrate holder.

Auger Analysis

Auger analysis was performed with a Scanning Auger Microprobe system. The UHV chamber was equipped with a CMA Auger analyzer, a rasterable ion gun, a Ti sublimator and LN₂ cooled cryopanels. The electron gun was operated at 2kV, at a current of about 0.6 μA, rastered over a spot size of 50 μm to reduce the intensity. Auger derivative spectra were recorded either directly, with a modulation amplitude of 3 eV, or by a peak-height recording multiplexer, with a 6 eV modulation amplitude.

The ion gun was operated at 2kV in an Ar atmosphere ($p = 5 \times 10^{-5}$ Torr), with a rastered beam, and at selected current densities between 2 and 30 μA/cm². Auger depth profiles were recorded during ion milling, with Ti sublimators operating and cryopanels cooled to liquid nitrogen temperature. These procedures reduced contamination of ion-milled surfaces by residual gas vapors to below detectable levels.

Quantitative analysis was accomplished with the usual normalization procedures (8). The normalization constants (sensitivity factors, S) are similar to those found in the PHI Auger handbook (9) and were verified for a variety of alloy steels and carbide powders of known composition. The value for carbon differs from the handbook value, which was established for a graphitic-like carbon lineshape and not a carbide-like lineshape. The value for N_{KLL} is smaller than the handbook value, but agrees to within 20 percent after correcting for electron beam ionization cross sections. Sensitivity factors are listed in Table 1 for the principal Auger spectra lines (e.g. the 650 eV line for Fe) of the detected species.

Accurate normalization constants are necessary to obtain even the relative concentration of nitrogen in steels of different alloy content, as is the case here. Analysis of the unimplanted steels gave atomic concentrations of Fe(72)Cr(20)Ni(7.9) for type-304 and Fe(97)C(3) for the carbon steel.

The depth scale for the Auger profiles was established by Michelson interferometry. Auger depth profiles were taken near the edges of partially masked steel surfaces. The depth of an ion-milled step was later measured with an interference microscope to an accuracy of about ± 5 nm. This procedure gave the depths at which several composition profiles had been terminated. Since no differences were observed in the milling rates of nitrogen-implanted and unimplanted steels, the depth was assumed proportional to milling time.

RESULTS

The results of numerous abrasive wear experiments with the carbon steel disks are shown in Fig. 2. Disks with a hardness of 400 kg/mm² were treated as the reference surfaces; bars through the other points indicate their standard errors. Mutton and Watson studied the wear of a similar steel (SAE 1080) against fixed 80 μm abrasives (10), and the curve in Fig. 2 is from their results, normalized to pass

TABLE 1—SENSITIVITY FACTORS FOR AUGER PEAK-TO-PEAK AMPLITUDES ACQUIRED AT A MODULATION AMPLITUDE OF 3 eV

AUGER LINE	Fe_{650}	C_{270}	Ni_{848}	C_{272}	N_{380}
S	0.17	0.34	0.16	0.47	0.31

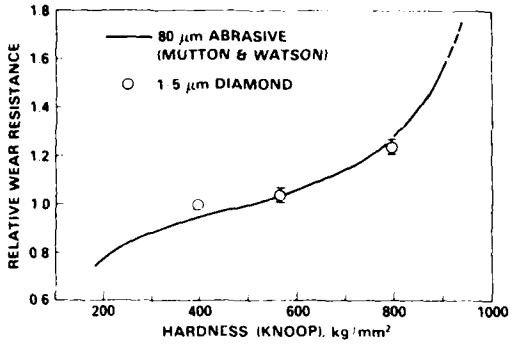

Fig. 2—Relative wear resistance of carbon steel disks of different hardness abraded with 1–5 μm diamond.

through the point for the disks of 570 kg/mm² hardness. The data taken with 1 to 5 μm diamond particles suggests that the wear was sufficiently abrasive in nature to be used as an indirect measure of surface hardness.

Wear resistance data were also obtained for both a nitrided carbon steel (ion-nitrided at 800 K for 12 hours) and the stainless steel. RWR results, relative to carbon steel of hardness $HK_{25} = 400$ kg/mm², are given in Table 2. The high RWR value of stainless steel is likely due to surface hardening during abrasion (*11*) and will be discussed later.

The effect of nitrogen implantation in the carbon steel was then examined. Disks having a bulk hardness of 400 kg/mm² were implanted to doses of 1 or 2×10^{17} nitrogen ions/cm² at 40 keV/ion, and their abrasive wear rates determined relative to identical unimplanted disks. RWR data for several sets of implanted carbon steel disks are shown in Fig. 3. The dashed line indicates the trend of the data. The wear resistance of the outermost 25 nm of the implanted surface was markedly higher than that of unimplanted reference disks, quench hardened disks (RWR ≈ 1.2), and nitrided disks (RWR ≈ 1.5), indicating the presence of a hardened surface layer. With continued abrasion, the wear resistances of the implanted disks decreased, reaching that of the reference disks after about 100 nm of the implanted disk was removed.

Auger depth profiles were taken to observe the exact depth to which nitrogen was implanted. A profile of a carbon steel disk, implanted to a dose of 2×10^{17} nitrogen ions/cm² at 40 keV/ion, is shown in the lower half of Fig. 3, curve (a). The profile has many of the features expected of implanted nitrogen in steel: it peaks at about 50 nm, then falls off like a Gaussian distribution. The nitrogen concentration at its maximum value was 14 ± 2 atomic percent. The near surface (< 40 nm) concentration, however, was considerably larger than expected. The expected profile, observed by the authors on only one occasion, is depicted by curve (b). Profiles such as curve (a) have also been obtained for nitrogen-implanted AISI 52100 steel, a 1.5 Cr 1C (percent by weight) bearing steel.

The depth to which the wear resistance was affected (100 nm) correlated well with the depth to which most of the nitrogen was implanted. Auger analysis of an implanted disk worn to a depth of 97 nm failed to detect nitrogen in the surface (sensitivity ca 0.2 atomic percent). Hence, most of the implanted nitrogen was removed from the surface during the first 100 nm of wear.

The abrasive wear technique was then used to determine the wear resistance of the stainless steel (type-304) disks implanted with 2×10^{17} nitrogen ions/cm² at 40 keV/ion. The RWR results for the implanted stainless steel, relative to unimplanted disks of the same steel, are shown in Fig. 4. Its behavior was markedly different from that of the carbon steel in several ways. Unlike the effect in carbon steel, nitrogen implantation reduced the RWR of the stain-

TABLE 2—RELATIVE WEAR RESISTANCE OF NITRIDED CARBON STEEL AND STAINLESS STEEL TO CARBON STEEL OF $HK_{25} = 400$ kg/mm²

	NITRIDED CARBON STEEL	TYPE-304 STAINLESS STEEL
RWR	1.5 ± 0.1	2.2 ± 0.1
HK_{25}(kg/mm²)	–	290

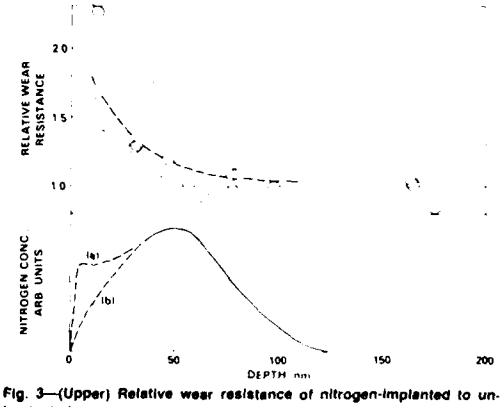

Fig. 3—(Upper) Relative wear resistance of nitrogen-implanted to unimplanted carbon steel vs depth. (Lower) (a) observed and (b) expected nitrogen concentration vs depth.

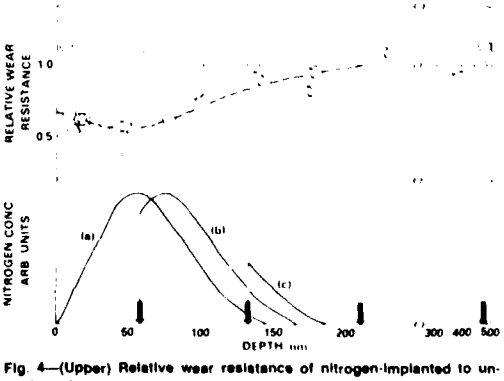

Fig. 4—(Upper) Relative wear resistance of nitrogen-implanted to unimplanted stainless steel vs depth. (Lower) Nitrogen concentration vs depth profiles of surfaces exposed to (a) no wear and (large arrows) various stages of wear. Note depth scale change at 250 nm.

less-steel surfaces. Moreover, the reduced RWR persisted to more than twice the depth of implantation.

The Auger depth profile shown in Fig. 4, curve (a), provided direct evidence that the reduced RWR persisted far deeper than the nitrogen was initially implanted. The profile of 40 keV nitrogen ions implanted to a dose of 2×10^{17}/cm^2 in stainless steel exhibited the expected Gaussian-like distribution with a mean penetration depth of 55 nm. The nitrogen concentration at 55 nm was 23 ± 2 atomic percent, about 70 percent larger than the peak value for the same dose of nitrogen in carbon steel. The oxide layer on the nitrogen-implanted surface (ca. 4–8 nm) was only slightly thicker than on surfaces of freshly polished stainless steel (ca. 2–3 nm).

To ascertain whether nitrogen might have migrated inward during abrasion, nitrogen profiles were taken on disks worn to depths of 58 nm, 134 nm, 210 nm, and lower. No measurable concentration of nitrogen (< 0.2 atomic percent) was detected on disks worn 210 nm or more. Profiles for wear depths of 58 nm and 134 nm are given by curves (b) and (c) in Fig. 4. Each curve was plotted with the surface (i.e. depth = zero) displaced by its wear depth. The profiles suggest that some of the implanted nitrogen migrated toward the bulk during wear. Not only was there more nitrogen below the surface than would be expected from the initial implant profile, but the depth distribution of remaining nitrogen retained the initial implant profile. The nitrogen appears to have migrated over these depths without dispersing. Much of the nitrogen, however, was lost from the outermost layers during abrasion. Profiles also indicated that the oxide layer on the abraded nitrogen-implanted surface had the same thickness as freshly polished stainless-steel surfaces.

Two sets of type-304 stainless-steel disks were separately implanted with titanium to doses of 4.6×10^{17} ions/cm^2. Analysis showed that the titanium reached a peak concentration of 30 atomic percent at a depth of 70 nm, and was detectable to 200 nm. A surprisingly large amount of carbon was found, as had been the case previously in titanium-implanted AISI 52100 steel (*12*). Much of the titanium in the first 150 nm appeared to be present as a carbide. A pronounced hardening of the surface resulted, as shown by the abrasive wear data in Fig. 5. Due to the very low initial wear rates, the RWRs were calculated by dividing the sum of the wear depths of the three reference disks by the sum of the wear depths of three implanted disks in each set, and a logarithmic scale was used for the ordinate. The effect of the titanium persisted to about 500 nm, apparently twice the depth affected by nitrogen. However, the detectability of persistence in the case of titanium may have been enhanced by the larger dose and its much greater effect on hardness. Migration would not be expected with this element.

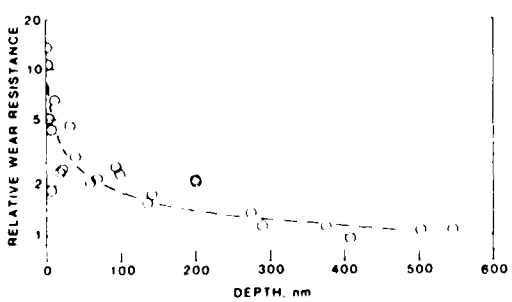

Fig. 5—Relative wear resistance of titanium-implanted to unimplanted stainless steel vs depth.

DISCUSSION

Two nitrogen-implanted steels—a tempered carbon steel and an austenitic stainless steel—showed quite different behavior to abrasion by micrometer-size diamond particles. The concentrations and mobility of the implanted nitrogen also differed. More nitrogen appeared to be retained in the highly alloyed stainless steel than in the low-alloy carbon steel. Based on the wear studies of hardenable carbon steel, it can be claimed that the nitrogen implants harden the surface of the carbon steel. Much of the speculation on increased wear resistance of nitrogen-implanted steels has centered on the formation of finely dispersed but mobile nitride-like species (*13*). Longworth and Hartley have, in fact, detected Fe nitrides in implanted Fe foils (*14*). These nitride-like species may have been responsible for hardening the carbon steel surface. Dearnaley et al (*15*) observed that the retention of implanted nitrogen increased as the alloy content of the steel was increased. The profile of nitrogen in the low-alloy carbon steel (Fig. 3) suggests that nitrogen may have migrated back toward the surface during implantation and been removed by sputtering or desorption, while that implanted in the stainless steel remained in place. Auger and X-ray photoelectron studies of nitrogen-implanted stainless steel (*16*) showed that nitrogen and chromium bonded as chromium nitride, which may account for the tenacity of the implanted nitrogen.

Nitrogen is much more soluble in γ iron and stainless steel than in the α phases (*17*), (*18*), another factor which would affect its concentration and mobility. The reduced RWR of nitrogen-implanted stainless steel suggests that the implanted surfaces were, in some sense, softer than the unimplanted surfaces. Auger results show the effect of implantation cannot be attributed to an oxide-rich surface layer as has recently been speculated (*13*). A comparison of the wear rate of stainless steel relative to the tempered carbon steel indicated the stainless surface had an anomalously large RWR for its bulk hardness. This large value was probably due to extreme surface hardening during abrasion. Surfaces of austenitic steels such as type-304 can harden excessively by undergoing structural transformations during abrasive wear (*11*). Transformation hardening may have been prevented, however, by the presence of implanted nitrogen, a solute atom known to stabilize the austenitic structure against transforming (*19*). When transformation did occur, the reduced solubility of nitrogen may have forced it to migrate deeper into untransformed austenite.

The ability of the nitrogen-implanted surface to resist hardening may also explain, in part, the improved sliding

wear resistance of nitrogen-implanted austenitic stainless steel on steel (*2*), (*20*). Unimplanted surfaces appeared to suffer severe wear (i.e. little or no run-in period) even under lubricated sliding conditions. Severe sliding wear on austenitic stainless steels, according to Hsu, et al (*21*), proceeds by delamination of a thin, brittle layer, identified to be transformed martensite, on a softer substrate. Implantation of nitrogen might prevent a surface from transforming and becoming brittle, thereby preventing this deleterious "hard skin on soft substrate" wear condition.

In addition to the increased resistance to sliding wear between metal couples, wear resistance of nitrogen-implanted surfaces persisting far beyond the implantation depth had been claimed (*22*). The persistence has generally been attributed to migration of the implanted species during the wear process (*3*). Recently, Lo Russo, et al (*23*) detected, with nuclear reaction analysis, about 20 percent of the initial implanted nitrogen dose in a case-hardening steel flat worn to a depth of 5 μm. Wear was produced by reciprocating sliding between two unlubricated flats. As suggested by Hartley (*13*), this wear condition was essentially *abrasive*. Interestingly, *the implanted slider, which* had a lower wear rate beyond the run-in period, showed a larger mass loss during run-in than the unimplanted surface (*24*).

The results of the authors' wear tests (Fig. 1), clearly more abrasive than Lo Russo's, also indicate that the implanted stainless steel initially lost mass more rapidly than the unimplanted steel. This decreased wear resistance persisted beyond the initial implant depth and was accompanied, according to curves (b) and (c), by an inward migration of nitrogen.

The remarkable hardening of the stainless steel by implanted titanium appears to parallel results obtained recently with AISI 52100 steel, where large reductions in friction and wear were found (*12*). These effects were attributed to the presence of hard, intermetallic titanium carbide, which was detected in these surfaces just as it was in the type 304 disks.

SUMMARY AND CONCLUSIONS

Wear with micrometer-size abrasives has been correlated with hardness and used to determine the hardness of surface layers as thin as 25 nm. The surface of nitrogen-implanted carbon steel was found to be harder than the bulk, while nitrogen implanted type-304 stainless steel surfaces were softer than unimplanted ones. The relative softness of the implanted stainless steel surfaces may have been due to interference with transformation hardening during wear. This mechanism may explain the beneficial effect of implantation seen with sliding wear, where work hardening can increase delamination and wear.

The hardening effect in carbon steel was confined to the initial depth of implantation. In the stainless steel, however, the softening effect persisted to twice the initial depth, and migration of the nitrogen was observed. Despite the migration observed in the stainless steel, the implanted nitrogen appeared to be more tightly bound there than in the low alloy steel.

Implantation of titanium in the stainless steel produced considerable hardening of the surface, apparently due to the formation of titanium carbide.

ACKNOWLEDGMENTS

The authors would like to acknowledge the advice and assistance of J. K. Hirvonen, B. B. Rath, J. S. Murday, C. A. Carosella, and colleagues in NRL's ion implantation program, P. Jindal of the ABAR Corporation (Feasterville, PA) for preparing nitrided disks, and D. A. Rigney and E. Rabinowicz for valuable discussions.

REFERENCES

(1) Dearnaley, G. and Hartley, N. E. W., "Ion Implantation into Metals and Carbides," *Thin Solid Films*, **54**, pp. 215–232 (1978).

(2) Hirvonen, J. K., "Ion Implantation in Tribology and Corrosion Science," *J. Vac. Sci. Technol.*, **15**, pp. 1662–1668 (1978).

(3) Hartley, N. E. W., "Ion Implantation Case Studies—Manufacturing Applications," in *Surface Treatments for Protection*, Institute of Metallurgists.

(4) Rabinowicz, E., "Abrasive Wear Resistance as a Materials Test," *Lubr. Eng.*, **33**, 7, pp. 378–381 (1977).

(5) Rabinowicz, E., Doherty, P., and Boyd, D. M., "Measurement of the Abrasive Wear Resistance of Hard Coatings," *Thin Solid Films*, **53**, pp. 301–302 (1978). (Abstract only.)

(6) Khrushov, M. M., "Principles of Abrasive Wear," *Wear*, **28**, pp. 69–88 (1974).

(7) Rabinowicz, E., *Friction and Wear of Materials*, John Wiley and Sons, Inc., New York (1965), pp. 169–176.

(8) Chang, C. C., "General Formalism for Quantitative Auger Analysis," *Surface Sci.*, **48**, pp. 9–21 (1975).

(9) *Handbook of Auger Electron Spectroscopy*, Physical Electronics Industries, Eden Prairie, MN, 2nd Edition (1976). Ed. Davis, L. E., p. 13.

(10) Mutton, P. J. and Watson, J. D., "Some Effects of Microstructure on the Abrasion Resistance of Metals," *Wear*, **48**, pp. 385–382 (1978).

(11) Richardson, R. C. D., "The Maximum Hardness of Strained Surfaces and the Abrasive Wear of Metals and Alloys," *Wear*, **10**, pp. 353–382 (1967).

(12) Carosella, C. A., Singer, I. L., Bowers, R. C., and Gossett, C. R., "Friction and Wear Reduction of Bearing Steel via Ion Implantation," presented at Materials Research Soc. Symp. on Ion Implantation, Boston, Mass., November 1979.

(13) Hartley, N. E. W., "Friction and Wear of Ion Implanted Metals," *Thin Solid Films*, **64**, pp. 177–190 (1979).

(14) Longworth, G. and Hartley, N. E. W., "Mossbauer Effect Study of Nitrogen Implanted Iron Foils," *Thin Solid Films*, **48**, pp. 95–104 (1978).

(15) Dearnaley, G., Goode, P. D., Hartley, N. E. W., Preston, G. W., Turner, J. F., and Watkins, R. E. J., "The Ion Implantation of Steel and Cemented Carbides," in *Ion Plating and Allied Techniques*, CEP Consultants Ltd. (1979). Ed. Hudley, R. (To be published.)

(16) Singer, I. L. and Murday, J. S., "The Chemical State of Ion Implanted Nitrogen in Fe/Cr/Ni Steel," *J. Vac. Sci. Technol.*, **16**, pp. 330–332 (1980).

(17) Gurney, N. S. and Turkdogan, E. T., "The Effect of Alloying Elements on the Solubility of Nitrogen in Iron," *J. Iron & Steel Inst.*, **180**, pp. 344–348 (1955).

(18) Eckel, J. F. and Cox, J. B., "Temperature Dependence of the Solid Solubility of Nitrogen in AISI Type 304 Stainless Steel," *J. of Materials*, **3**, pp. 605–614 (1968).

(19) Everhart, J. L., "Specialty Stainless Steels," *Materials Eng.*, October, pp. 22–30 (1971).

(20) Hirvonen, J. K., Carosella, C. A., Kant, R. A., Singer, I. L., Vardiman, R., and Rath, B. B., "Improvement of Metal Properties by Ion Implantation," *Thin Solid Films*, **63**, pp. 5–10 (1979).

(21) Hsu, K. L., Ahn, I. M., and Rigney, D. A., "Friction, Wear, and Microstructure of Unlubricated Austenitic Stainless Steels," in *Wear of Materials—1979*, ASME, New York (1979). Eds. Ludema, K. C., Glasser, W. A., and Rhee, S. K., pp. 12–26.

(22) Hartley, N. E. W., "Ion Implantation and Surface Modification in Tribology," *Wear*, **34**, pp 427–438 (1975)
(23) Lo Russo, S., Mazzoldi, P., Scotupi, L., Tosello, C., and Tosto, S., "Effect of Nitrogen-Ion Implantation on the Unlubricated Sliding Wear of Steel," *Appl. Phys. Lett.*, **34**, pp 627–629 (1979)
(24) Ref. (23), Fig. 1, or Ref. (13), Fig. 8

Presented at the ASME ASLE Lubrication Conference, San Francisco, California, August 18–21, 1980

Section II.C

THE CHEMICAL STATE OF ION-IMPLANTED NITROGEN IN Fe-18Cu-8Ni STEEL

I. L. Singer,[1] and J. S. Murday[1]

[1]Surface Chemistry Branch
Chemistry Division
Naval Research Laboratory

This work was supported by the Office of Naval Research.

Chemical state of ion-implanted nitrogen in Fe18Cr8Ni steel

I. L. Singer and J. S. Murday

Surface Chemistry Branch, Code 6170, Naval Research Laboratory, Washington, D. C. 20375

(Received 27 August 1979; accepted 5 November 1979)

Auger electron spectroscopy (AES) and x-ray photoelectron spectroscopy (XPS), in conjunction with ion milling, were used to determine the chemical state of nitrogen implanted at relatively high doses (10^{16}–10^{18}/cm^2) into type-304 steel. Nitrogen atoms were bonded in the nitrided state, at all doses, according to both AES and XPS. As the nitrogen concentration increased, the lineshape of the Cr *MVV* Auger spectra evolved from that of metallic Cr to Cr nitride; at highest doses, the Fe *MVV* lineshape could be identified as Fe nitride. Auger and XPS spectra of implanted 304 and thermally nitrided 304 were virtually identical at comparable nitrogen concentrations. The Cr($2p_{3,2}$) binding energies of both, however, were about 1 eV lower than found in Cr nitride but 0.5 eV higher than in metallic Cr.

PACS numbers: 82.80.Pv, 61.70.Tm, 61.70.Wp

I. INTRODUCTION

Steels implanted with nitrogen ions have exhibited greatly improved resistance to wear.[1–5] Since implants of inert ions[3,4] or self-ions[5] have not proven beneficial, the improvement is believed due, in part, to the chemical state of the N-implanted surface. Using Mossbauer spectroscopy, Longworth and Hartley[6] detected Fe nitrides in N-implanted Fe foils. Analytical studies of N-implanted steels by Dearnaley *et al.*,[7] however, suggest that alloying elements in the steel, not the Fe itself, may tie up the implanted nitrogen.

In the present study, we have examined the composition of an Fe18Cr8Ni steel surface implanted with high doses of nitrogen ions. Chemical analysis was performed with Auger electron spectroscopy and, to a lesser extent, XPS, and both in conjunction with inert ion milling. Chemical changes in the nitrogen-implanted surface with increasing implant dosages will be reported.

II. EXPERIMENTAL

The steel substrates used for this work were cut from AISI-type 304 stainless steel, an austenitic steel containing principally Cr (18%) and Ni (8%) by weight.[8] Finely polished substrates were implanted with 80 keV N_2^+ molecular ions (i.e., 40 keV/N^+ ion) in the Naval Research Laboratory's 200 keV implanter. Average current densities of the rastered ion beam were in the range 1–15 μA/cm^2. During implantation, the pressure in the target chamber was kept at 10^{-3} Pa or less.

One of the polished 304 substrates was nitrided by an ion-nitriding process.[9] The substrate was heated to 525 °C and exposed to an ammonia-hydrogen plasma for 12 h. The nitrided surface was repolished only enough to regain its luster (less than 5 μm of the 100 μm case was removed). In addition, an Fe foil, a Cr substrate, and several commercially prepared, ceramic powder specimens (CrN, Cr_2N, $Fe_2N + Fe_4N$) were acquired[10] as reference standards.

Auger electron spectroscopy was performed in a Physical Electronics Inc. (PHI) Model 545 Scanning Auger Microprobe. Spectra were taken in the derivative mode with a 2 keV electron-beam and with currents less than 1 μA. The electron analyzer was operated with modulation amplitudes of 1 eV at low electron energies (0–100 eV) and 3 eV at high energies (100–1000 eV). Auger spectra were taken during or immediately after ion milling in an Ar or Ne gas atmosphere at chamber pressures of 7 mPa. The ion beam was operated at 2 keV and at selected current densities between 1–30 μA/cm^2, as measured with a Faraday cup.

X-ray photoelectron spectroscopy (XPS) was performed in a PHI Model 548 Auger/ESCA spectrometer equipped with a 1 keV ion gun. The x-ray source was operated with an Al anode, and spectra were taken in the retard mode with a pass energy of 50 eV, corresponding to an overall energy resolution of about 1.2 eV.

Chemical information was extracted from both Auger and XPS spectra. Lineshapes of Auger valence spectra, i.e., spectra resulting from valence electron transitions, were used to fingerprint the chemical state of certain elements. The method has been described previously for chemically modified Fe alloy surfaces.[11–13] XPS binding energies were measured relative to the Au $4f_{7/2}$ electron level (BE = 84.0 eV). The binding energy of the Fe $2p_{3/2}$ electron level was used as a secondary reference; a value of 707.0 ± 0.2 eV was obtained on ion-milled 304 substrates in agreement with several recently published values.[14,15] Binding energies for the chromium nitride powder samples could not be reproduced as accurately as for steel substrates probably because of charging or binding energy shifts due to excessive oxygen contamination.

III. RESULTS AND DISCUSSION

Auger electron spectroscopy, in conjunction with inert-ion milling, was used to examine the composition of 304 substrates implanted with nitrogen to doses from 10^{16} to 10^{18} N^+/cm^2. Composition profiles of all samples showed the presence of a surface carbon-contaminant overlayer and an oxide film. The thickness of the oxide film varied depending on sample implantation conditions. Composition of the oxide layer and

 0022-5355/80/010327-03$01.00

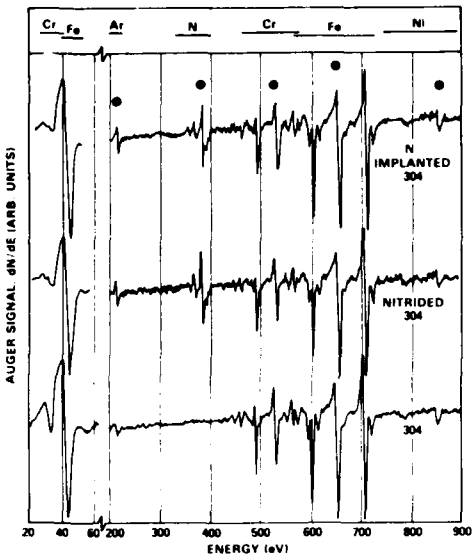

FIG. 1. Auger spectra for three 304 substrates: top: nitrogen implanted 304, 10^{17} cm^2 at 40 keV, spectrum recorded at depth near maximum nitrogen amplitude, middle: nitrided 304, bottom: 304. High energy spectra (200–900 eV) taken with modulation amplitude of 3 eV during Ar ion milling (2 keV at 20 μA cm^2), low energy spectra (20–60 eV) at 1 eV modulation with ion beam off.

the oxide/metal interface closely resembled thermal oxides, with thickness and composition corresponding to different temperatures of growth.[16]

Composition vs depth profiles of the subsurface layer easily detected nitrogen implanted at lowest doses ($\sim 2 \times 10^{16}$ cm^2). Nitrogen depth profiles were roughly Gaussian for doses $\geq 2 \times 10^{17}$/cm^2, with peak concentrations at about 55 nm below the surface. At a dose of 10^{18}/cm^2, the profile was skewed, looking more like the profile of implants in surfaces subjected to sputtering during implantation.[17]

The chemical state of the atoms in the nitrogen-alloyed sub-surface layer has been inferred principally from Auger spectra. An Auger spectrum of 304, implanted to 10^{17} /cm^2, is shown in Fig. 1 (upper trace). The spectrum was taken after approximately 55 nm of the substrate was removed by 2 keV Ar^+ ion milling. For comparison, spectra of ion-milled, nitrided 304 (middle trace), and ion milled, 304 (lower trace) are also shown in Fig. 1. The high energy portions (200–900 eV) of Fig. 1 were recorded during ion milling to minimize O and C buildup on the clean surface. The low energy portions (20–60 eV) were recorded with the ion beam off; the ion beam appeared to distort the low energy spectra. The high energy portion of the spectrum shows the presence of the three main elements of 304: Fe, Cr, and Ni. In addition, it shows implanted nitrogen and argon; the argon signal is attributed to the atoms imbedded during Ar-ion milling. The low energy portion of the spectrum, presented on an expanded energy scale, shows the MVV Auger spectra of Cr and Fe.

The spectra of N-implanted 304 and nitrided 304 had several features in common which were not found in spectra of 304. Both spectra had similar N_{KLL} lineshapes and, at implant doses of about 10^{17} cm^2, almost equal amplitudes. Their Cr_{MVV} lineshapes were similar to each other but differed from that in 304. The peak-to-peak amplitude ratios of I_{Cr} I_{Fe} (LMM spectra) in both were smaller than in 304, while the ratios I_{Ar} I_{Fe} were larger. The latter two features may be a consequence of the nitrogen chemistry and, or the ion-milling process, and will be treated in a later paper.

TABLE I. Experimental binding energies (in eV) of Cr and Fe $2p_{3/2}$ electron levels and N 1s electron level in 304 substrates and reference compounds. Experimental uncertainty is ±0.2 eV.

	Binding energy (eV)		
	Cr($2p_{3/2}$)	N(1s)	Fe($2p_{3/2}$)
304 (10^{17} N$^+$/cm^2)[a]	574.8	397.7	707.1
304 (nitrided)[a]	574.8	397.2	707.1
304 (bulk)[a]	574.6		706.8
Cr[a]	574.1		
Cr[b]	574.2		
CrN[b]	575.7	396.8	
Cr_2N[b]	576.1	397.4	

[a] Substrates subjected to 1 keV Ar^+ ion bombardment.
[b] Taken from Table I of Ref. 22, experimental uncertainty stated to be ±0.1 eV.

Nitrogen in N-implanted 304 appeared to be in a nitrided state, based on its N_{KLL} Auger lineshape. The N_{KLL} lineshape, at all detected amplitudes ($0.01 < I_N$ $I_{Fe} < 1.4$), resembled the N_{KLL} lineshape of nitrided 304. This lineshape, shown in Fig. 1, was also virtually indistinguishable from N_{KLL} lineshapes observed in spectra of chrome nitrides, iron nitrides, or niobium nitride.[18] The lineshape differed, however, from N_{KLL} spectra of a nonmetallic nitride, BN,[19] and of compounds containing N–O ligands.[20]

XPS data also indicated nitrogen in a nitrided state. The

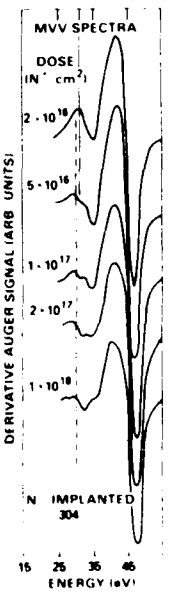

FIG. 2. Cr_{MVV} and Fe_{MVV} Auger spectra of N implanted 304 at doses from 2×10^{16} cm^2 to 10^{18} cm^2. Analyzer operated at a modulation amplitude of 1 eV.

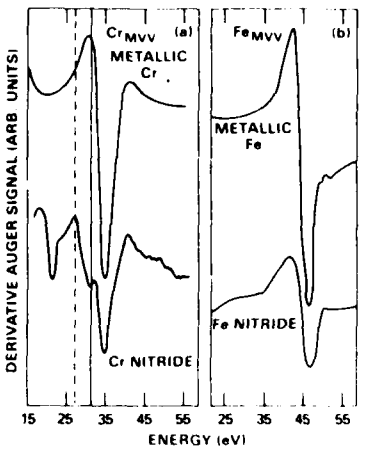

FIG. 3. MVV Auger spectra of (a) metallic Cr and Cr Nitride and (b) metallic Fe and Fe nitride. Analyzer operated at modulation amplitude of 1 eV.

binding energy of the N(1s) level in N-implanted 304 was found to be 397.7 ± 0.2 eV. This binding energy BE is characteristic of nitrogen in a nitrided state.[21,22] The N(1s) binding energy of nitrided 304 was further shifted downward by 0.5 eV from that of N implanted 304. The measured binding energies for the two substrates and for several reference compounds are listed in Table I. In addition, N(1s) spectra of both substrates also showed a "shoulder" at a binding energy near 400 eV. This shoulder may be attributed to a weakly adsorbed N species, observed on freshly polished *nitrided* 304 surfaces and on Fe surfaces exposed to nitrogen-containing gases.[23] In summary, both AES and XPS data indicated that nitrogen implanted into 304 exists as a nitrided species.

Auger analysis further suggested that the nitrogen was most likely tied up chemically with the chromium. Evidence for this was found in the MVV lineshape changes shown in Fig. 2. With increasing doses of N ions, the peak in the MVV curve at 32 eV (solid line) became attenuated, and at 22 eV. At the same time, a new peak developed at 28 eV (dashed line) and the overall amplitude of the 28–36 eV peak decreased relative to the 38 eV–46 eV peak. We associate this spectral feature with the nitriding of Cr and not Fe since it appeared in nitrided Cr [(Fig. 3(a)] but not in nitrided Fe [(Fig. 3(b)]. At implant doses greater than 2×10^{17} cm^2, the Fe might also have become nitrided, the rounding of the Fe_{MVV} peak on the low energy side of the Fe_{MVV} spectra of Fig. 2 is consistent with a similar rounding in the Fe nitrided spectrum of Fig. 3(b).

With XPS, the chemical state of Cr in the N^+-implanted substrate could not be clearly identified. The Cr (3*s*) and Cr (3*p*) spectra were partially obscured by overlapping x-ray satellites of the corresponding Fe spectra. The Cr $2p_{3/2}$ data, listed in Table I, shows that the binding energy was 1 eV lower than in reference Cr nitrides and 0.5 eV higher than in metallic Cr. However, the same value was found for nitrided 304, which is believed to contain CrN precipitates.[24] This discrepancy may be due to sputtering artifacts (there was no mention of sputtering for the Cr nitride reference data), or it may be that the Cr binding energy for Cr nitride precipitates in 304 are shifted in energy from bulk Cr nitride.

IV. SUMMARY AND CONCLUSIONS

Auger analysis on conjunction with inert ion milling was used to examine the composition of 304 implanted with N to doses ranging from 10^{16}–10^{18} cm^2. Below the oxide layer, a unique nitrogen alloyed subsurface layer was formed. Nitrogen concentration vs depth profiles were Gaussian-like in shape for doses up to 2×10^{17} cm^2, but at an implant dose of 10^{18} cm^2, the nitrogen profiles appeared sputter-limited. The chemical states of the implanted N and the metallic host atoms, Fe and Cr, were identified principally by their Auger lineshapes. N was observed in a nitrided state at all doses. Cr appeared to be the metallic species bonded to N at doses up to 2×10^{17} cm^2, and Fe, too, appeared bonded to N at 10^{18} cm^2. The technique, however, was not capable of indicating whether the metal atom–nitrogen interaction occurred between solutionized atoms or within metal nitride precipitates.

ACKNOWLEDGMENTS

The authors thank Crucible Steel Corporation for providing the 304. Dr. P. C. Jindal of ABAR Corporation for nitriding our substrates, and Drs. R. A. Kant, R. Vardiman and J. K. Hirvonen for assisting in the implantation and for valuable discussions.

[1] G. Dearnaley and N. E. W. Hartley, Thin Solid Films **54**, 215 (1978).
[2] N. E. W. Hartley, Wear **34**, 427 (1975).
[3] J. K. Hirvonen, J. Vac. Sci. Technol. **15**, 1662 (1978).
[4] N. E. W. Hartley, Thin Solid Films **64**, 177 (1979).
[5] J. K. Hirvonen, C. A. Carosella, R. A. Kant, I. Singer, R. Vardiman, and B. B. Rath, Thin Solid Films **63**, 5 (1979).
[6] G. Longworth and N. E. W. Hartley, Thin Solid Films **45**, 95 (1978).
[7] G. Dearnaley, P. D. Goode, N. E. W. Hartley, G. W. Proctor, J. F. Turner, and R. F. J. Watkins, International Plating and Allied Techniques Conference (London, July 1979). Edited by R. Hurley, to be published.
[8] Crucible Steel Corporation, heat # S55184. Type 304 wt.% C (0.055), Mn (1.75), P (0.028), S (0.005), Si (0.50), Ni (8.48), Cr (18.18), Mo (0.36), N_2 (0.05), Fe (remainder).
[9] P. C. Jindal, J. Vac. Sci. Technol. **15**, 313 (1978).
[10] Ceramic powders purchased from Materials Research Corporation, Orangeburg, N.Y.
[11] C. Leygraf, G. Hultquist, and S. Ekelund, Surf. Sci. **51**, 409 (1975).
[12] M. Seo, J. B. Lumsden, and R. W. Staehle, Surf. Sci. **50**, 541 (1975).
[13] F. G. Shafrin and J. S. Murday, J. Vac. Sci. Technol. **14**, 246 (1977).
[14] N. S. McIntyre and D. G. Zetaruk, Anal. Chem. **49**, 1521 (1977).
[15] K. Asami and K. Hashimoto, Corros. Sci. **17**, 559 (1977).
[16] G. Betz, G. K. Wehner, E. Toth, and A. Joshi, J. Appl. Phys. **45**, 5312 (1974).
[17] H. Liebl, J. Vac. Sci. Technol. **12**, 385 (1975).
[18] I. Singer and J. S. Murday, to be published.
[19] B. H. Suden and R. Bastasz, J. Vac. Sci. Technol. **16**, 940 (1979).
[20] J. Ganer and J. S. Murday, unpublished results.
[21] *Handbook of X-ray Photoelectron Spectroscopy*, edited by C. D. Muldenberg, Perkin-Elmer Corporation, Eden Prairie, MN, 1979.
[22] M. Romand and M. Roubin, Analusis **4**, 308 (1976).
[23] F. Honda and K. Hirokawa, J. Electron Spectrosc. **10**, 175 (1977).
[24] B. Mortimer, P. Grieveson, and K. H. Jack, Scand. J. Metall. **1**, 201 (1972).

Section II.D

SURFACE HARDENING OF BERYLLIUM BY ION IMPLANTATION

R. A. Kant,[1], J. K. Hirvonen,[1] A. R. Knudsen,[1]

and J. S. Wollam[2]

[1] Materials Modification and Analysis Branch
Radiation Technology Division
Naval Research Laboratory

[2]Charles Stark Draper Laboratory
Cambridge, Massachusetts

This work was supported by the Office of Naval Research
and by the Navy Strategic Systems Project Office.

Thin Solid Films, 63 (1979) 27–30

SURFACE HARDENING OF BERYLLIUM BY ION IMPLANTATION*

R. A. KANT, J. K. HIRVONEN AND A. R. KNUDSON
Naval Research Laboratory, Washington, D.C. 20375 (U.S.A.)
J. S. WOLLAM
Charles Stark Draper Laboratory, Cambridge, Mass. 02139 (U.S.A.)
(Received April 13, 1979; accepted April 25, 1979)

The effectiveness of ion implantation for the production of a hard wear-resistant surface on instrument grade beryllium of high strength (HP-40) was explored. Samples of beryllium were implanted with boron and were subjected to microhardness tests in both the as-implanted state and after annealing. The implanted region was examined using Rutherford backscattering to determine the depth distribution of the implanted boron. By using ion implantation to produce a buried layer containing boron, the limitations imposed by solubility and diffusivity are avoided and much greater boron concentrations than those attainable with conventional thermal treatments are generated.

1. INTRODUCTION

The feasibility of using ion implantation to harden the near-surface region of instrument grade beryllium (HP-40) was investigated. This study was motivated by a need to provide a means of reducing the wear experienced by gas-bearing surfaces during starting and stopping, while avoiding porosity and adhesion problems sometimes encountered with hard coatings. Attempts have been made to diffuse boron thermally from an outer layer (diffusion source) into beryllium to harden the surface. However, it appears that beryllium atoms may preferentially diffuse outward into the boron (rather than the boron diffusing into the beryllium), which would make this technique unsuitable for the preparation of desired surface alloys.

Implantations were carried out and microhardness tests and Rutherford backscattering studies were made to determine the effect of sputtering on the maximum attainable boron concentration and the effect of thermal annealing on the redistribution of the implanted boron.

2. MICROHARDNESS TESTS

The boron distribution for these tests was composed of four overlapping gaussian boron distributions implanted at energies ranging from 90 to 250 keV at fluences between 1.2×10^{17} and 1.7×10^{17} ^{11}B atoms cm^{-2}. The energies and fluences were chosen to produce a relatively uniform boron distribution of approximately 10 at.% concentration extending into the beryllium host to about 0.8

* Paper presented at the International Conference on Metallurgical Coatings, San Diego, California, U.S.A., April 23–27, 1979

μm. Samples were also implanted at proportionally higher fluences to produce 20 at.% and 40 at.% concentrations. Microhardness tests were made by impressing a pyramidal (Knoop) diamond stylus into the surface of the sample under a fixed load of 5, 10 or 25 g, measuring the dimension of the resultant depression and converting this to a microhardness value which is related to the yield stress of the material. Such measurements are difficult to quantify when the thickness of the layer to be measured is less than ten times the depth of penetration of the stylus. Nevertheless comparative measurements serve as useful guides.

Figures 1 and 2 are plots of the microhardness test results obtained on as-implanted samples and on samples annealed for 1 h at 650 C. As expected the results for the lighter loads more properly indicate the changes produced by the implantation. Both figures show an overall increase of hardness with increasing boron concentration. In addition thermal annealing produces a further net increase of hardness at the highest concentrations.

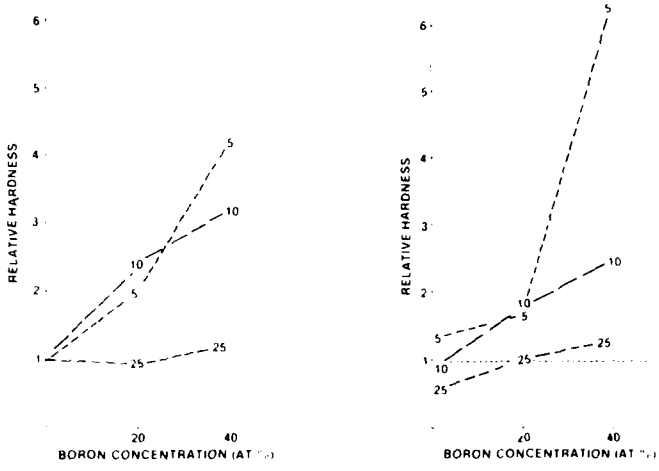

Fig. 1. Relative hardness of as-implanted HP-40 as a function of the initial peak boron concentration. The figures on the curves are hardness values normalized to the unimplanted hardness values obtained at each load.

Fig. 2. Relative hardness of implanted HP-40 annealed for 1 h at 650 C as a function of the initial peak boron concentration. The figures on the curves are hardness values normalized to the unimplanted hardness values obtained at each load.

The microhardness values obtained for near-surface regions can be influenced by several competing factors. The implantation process is expected to produce increases of hardness due to radiation damage and to compressive stress introduced by forcing a large number of impurity atoms into a host lattice. Thermal annealing reduces near-surface damage produced during sample preparation (e.g. by polishing) as well as radiation damage produced during implantation. Post-implantation heating can also facilitate the formation of surface oxides or of beryllium boride precipitates producing precipitation hardening. All of these factors are believed to be involved and yield the results shown in Fig. 2; however, the most significant net result is the hardening seen for the annealed sample of highest fluence.

This is presumably caused by the formation of a layer of a (hard) beryllium compound, the formation of beryllium boride precipitates causing hardening, or both of these. Microstructural studies in progress are expected to reveal which processes are occurring.

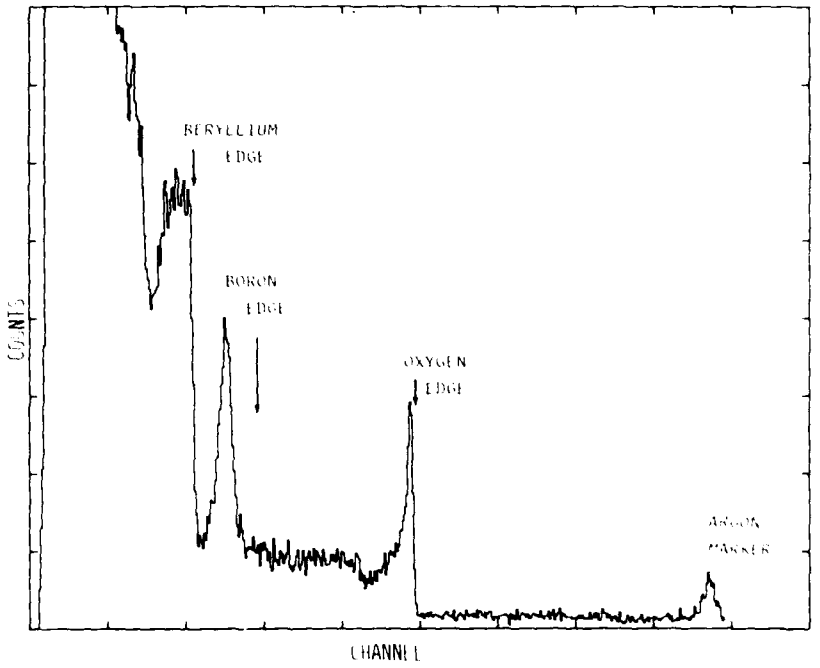

Fig. 3. Backscattering spectrum of as-implanted beryllium (4×10^{17} B atoms cm^{-2})

3. ION BACKSCATTERING ANALYSIS

Helium ion backscattering (3 MeV) was used to (1) measure the depth profile of the implanted boron, (2) study the effects of annealing on the boron distribution and (3) evaluate the limitation imposed by sputtering on the achievable boron concentration. Figure 3 is the backscattering spectrum of a sample implanted with 75 keV boron to a fluence of 4×10^{17} B atoms cm^{-2} and Fig. 4 is the spectrum of the same sample after annealing at 650°C for 20 min. Several conclusions can be drawn from these spectra. The argon marker implanted before the boron implantation was not observed to shift in energy (*i.e.* depth) due to the boron implantation, indicating that the sputtering rate due to the boron implantation is very low. This implies that higher concentrations of boron can be achieved. A comparison of the boron signals before and after annealing shows that annealing reduces the peak concentration and appears to move the boron towards the surface. In addition, the shape of the boron signal in Fig. 4 is consistent with that expected if boron were precipitating out[1], presumably as a beryllium boride. These results indicate that it should be possible to attain a boron concentration high enough to favor the formation of a layer of the

hardest beryllium boride BeB_2. The B–Be phase diagram indicates that BeB_2 may be present in the annealed layer containing 40 at.% implanted boron.

By using ion implantation to produce a buried layer containing boron, the limitations imposed by solubility and diffusivity are avoided and much greater boron concentrations than those attainable with conventional thermal treatments are generated. Time and temperature exposures are also greatly reduced compared with conventional diffusion. Whether implantation will prove to be an appropriate fabrication technique for this particular use will require further study. Nevertheless, this example serves to demonstrate the potential advantages of ion implantation as a surface-modifying technique for small critical parts. These potential advantages include the following: no macroscopic dimension changes, adhesion superior to that for coatings (because of no abrupt interfaces) and none of the porosity problems that are associated with some coatings for this application.

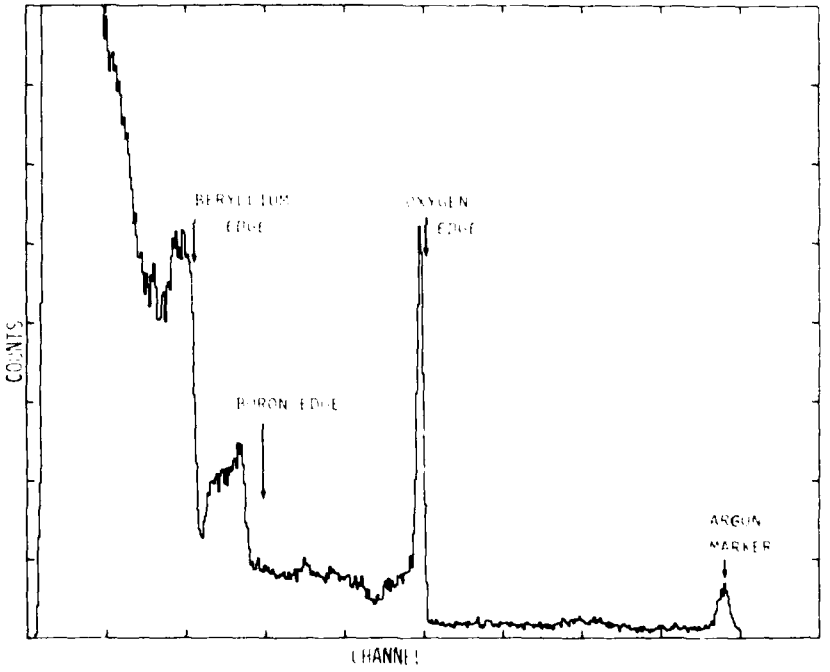

Fig. 4. Backscattering spectrum of boron-implanted beryllium annealed at 650°C for 20 min (4×10^{17} B atoms cm^{-2}).

ACKNOWLEDGMENTS

This work was supported in part (CSDL) by the Office of Naval Research under contract N00014-77-C-0388 and in part (NRL) by the Strategic Systems Project Office.

REFERENCE

1. S. M. Myers, *J. Vac. Sci. Technol.*, *15* (5) (1978) 1650.

Section II.E

THE EFFECT OF ION IMPLANTATION ON FATIGUE BEHAVIOR OF Ti-6Al-4V ALLOY

R. G. Vardiman[1]

[1]Alloy Transformation and Kinetics Branch
Material Science and Technology Division
Naval Research Laboratory

This work was supported by the Office of Naval Research.

The Effect of Ion Implantation on Fatigue Behavior of Ti-6 Al-4V Alloy

R. G. Vardiman
Alloy Transformations and Kinetics Branch
Material Science and Technology Division

Fatigue is a frequent cause of failure in metals and is very sensitive to surface effects. The technique of ion implantation is known to be effective in improving the surface properties of metals and alloys. The present study is one of the first to demonstrate substantial fatigue life improvement by ion implantation.

Carbon and nitrogen have been implanted in α - β processed Ti-6 Al-4V. A dose of 2 x 10^{17} atoms/cm^2 at 75 keV was used for each implant. This gives a maximum concentration of the implanted species of approximately 25 at.% at a depth of 70 to 80 nm beneath the surface.

The microstructure of the implanted layer was examined by transmission electron microscopy (TEM) using an implanted TEM specimen which had been partly thinned on one side. Final thinning experimentation was done from the opposite side. The structure found for the nitrogen implants consisted of a dense, poorly resolved damaged layer when viewed in bright field (Fig. 1a). Some electron diffraction patterns showed faint diffuse rings, and imaging in dark field with a beam from an area of the two closely spaced, innermost rings revealed second phase particles, typically about 10 nm in size (Fig. 1b). The diffraction pattern indicated a face-centered cubic structure with an estimated lattice parameter very close to that of TiN. Although another phase, Ti_2N can exist in the concentration range developed with these implants, it was not detected, and conditions apparently do not favor its formation.

The N^+ implanted samples were annealed in vacuum for four hours at 500°C. The diffraction patterns from the N^+ implanted samples were somewhat stronger and sharper, but particle size was only slightly increased as might be expected from the low mobility of nitrogen in titanium. Also, no noticeable change was found in the damage structure.

Carbon implanted samples showed the same dense damage structure, but, in addition, second phase particles were visible in bright field (Fig. 2). The amount of second phase appeared to be greater than in the case of nitrogen implantation. Diffuse rings were again found in the electron diffraction pattern and, in this case, corresponded to the structure and lattice parameter of TiC. After a one hour anneal at 400°C in ultra-high vacuum, their size range increased sharply (Fig. 2b), thus showing the greater mobility of carbon over nitrogen in α -Ti.

Implanted fatigue specimens of Ti-6 Al-4V were tested in rotating beam fatigue with the results shown in Fig. 3. It can be seen that although both implant species improved fatigue life, the carbon implant gives superior results at all stress levels, with an endurance limit increase of about 20 percent and a factor of 4 to 5 improvement in lifetime at the higher stress levels. Specimens given the heat treatment mentioned

previously showed no significant change in lifetime. It is natural to attribute the superiority of carbon implantation to the greater amount of second phase produced as compared to nitrogen implantation.

Carbon doses less than 1×10^{17} atoms/cm^2 do not give the full lifetime increase. The effect saturates at 1×10^{17}, and higher doeses do not change the fatigue life further, as shown in Fig. 4.

Many of the fatigue fracture surfaces have been examined in the scanning electron microscope. For all cases where the lifetime exceeded 2×10^5 cycles, the origin of the fatigue crack was found to occur between 25 and 150 μm below the surface irrespective of whether the specimen had been implanted or not. Such subsurface crack origins in titanium alloys have been reported by others and apparently give the same fatigue life as cracks which originated at the surface. The fact that fatigue life is increased despite the origination of the fatigue crck well below the implanted region indicates a complex effect of implantation on the failure mechanism.

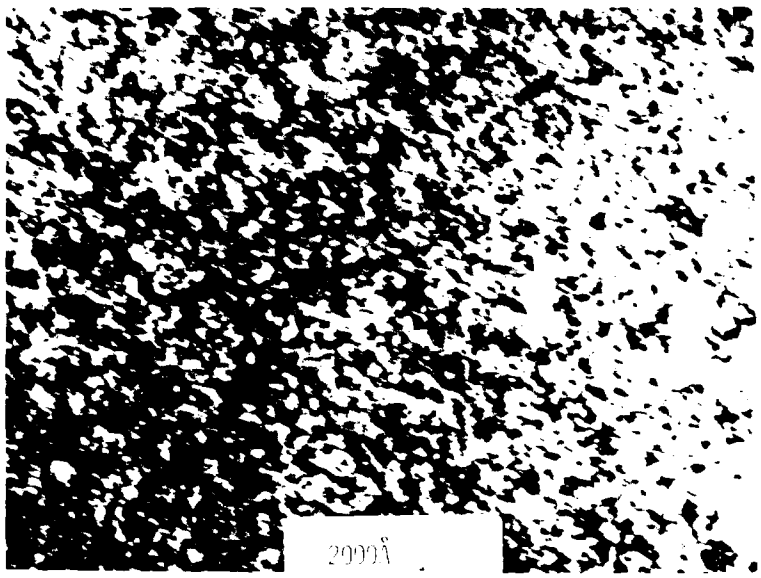

(a)

(b)

Fig. 1 Ti-6Al-4V implanted with 2×10^{17} at./cm^2 of nitrogen, TEM foils; (a) bright field, (b) dark field using beam from a section of the innermost diffuse rings of the diffraction pattern shown in inset.

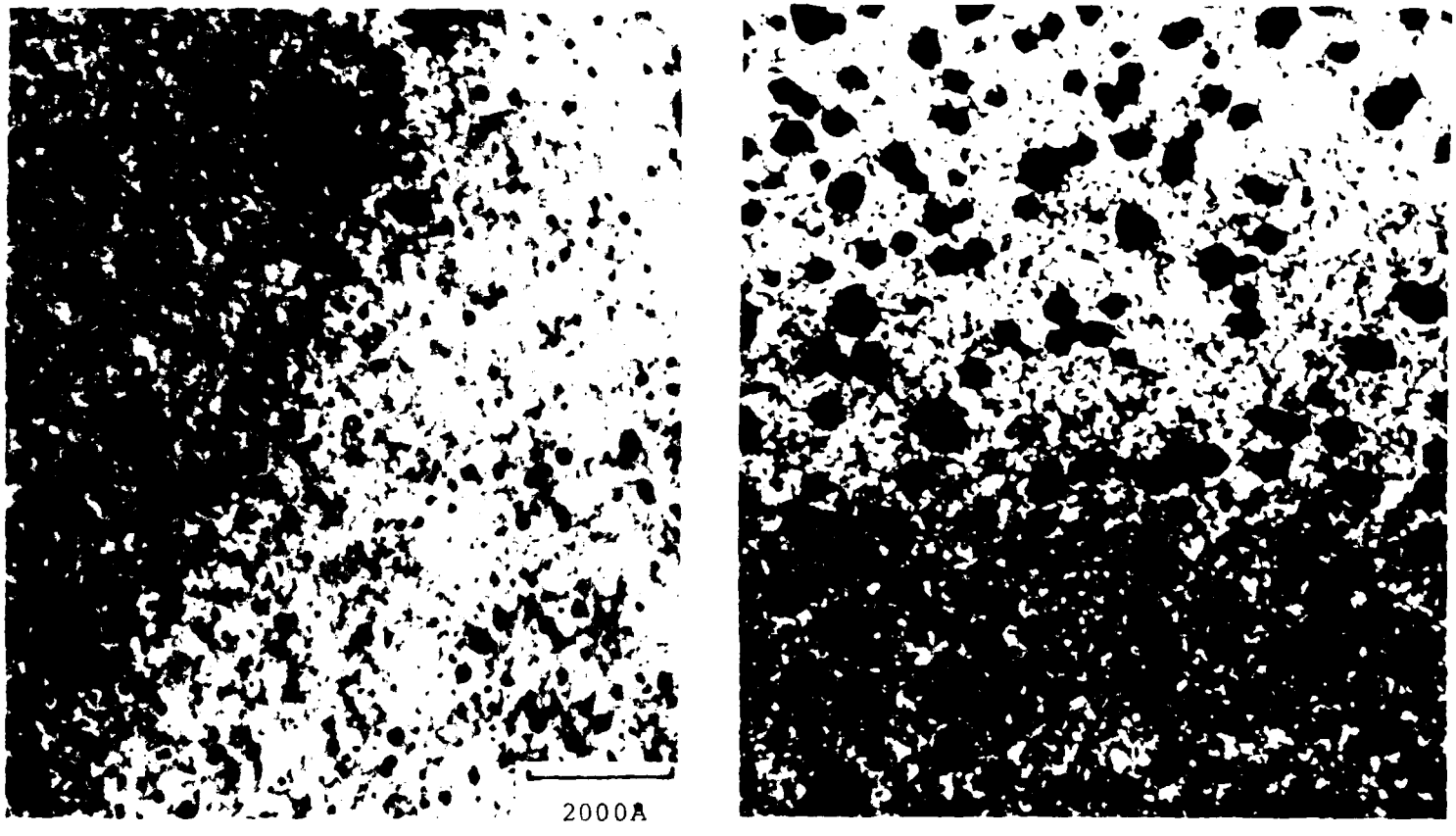

(a) (b)

Fig. 2 — Ti-6Al-4V implanted with 2×10^{17} at./cm^2 of carbon, TEM foils: (a) bright field, as implanted, (b) bright field, annealed 1 hour at 400°C.

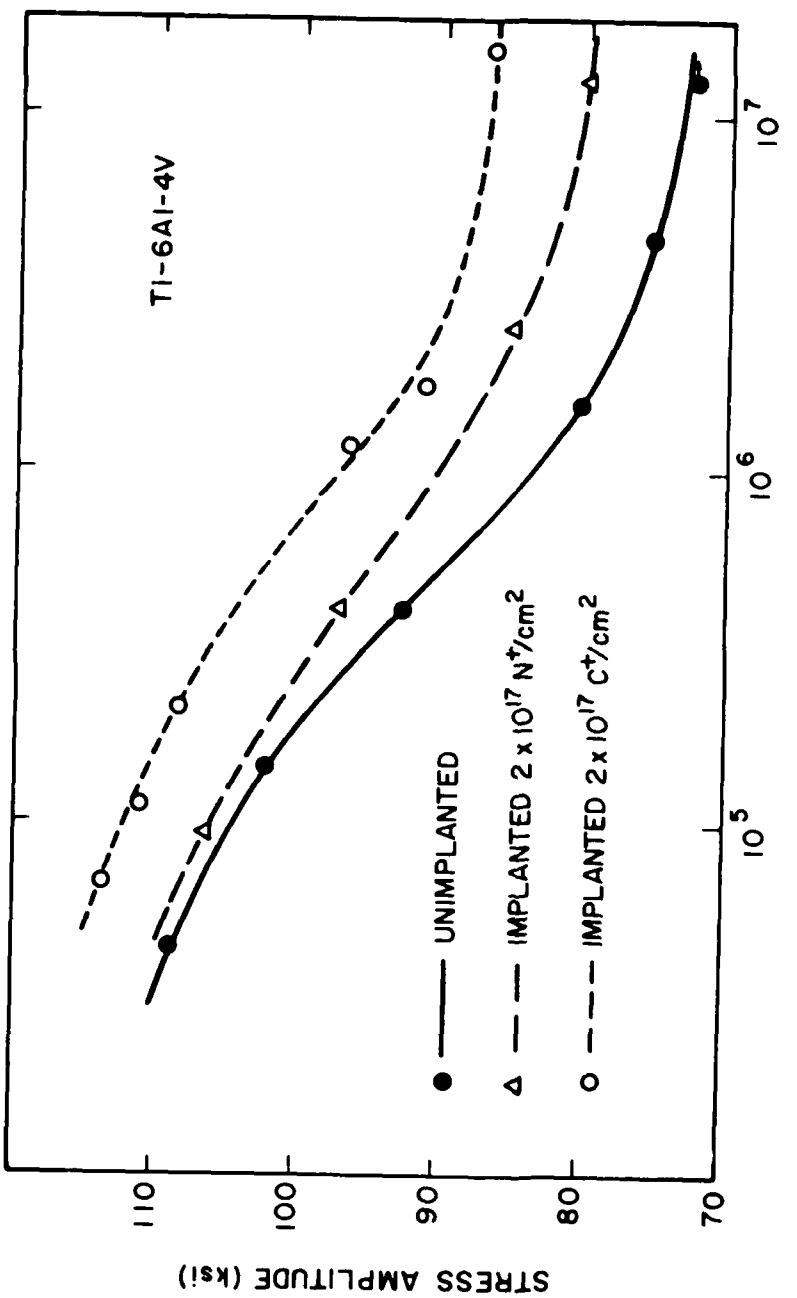

Fig. 3 — Maximum stress vs. cycles to failure for mill annealed Ti-6Al-4V in conditions indicated. Rotating beam fatigue.

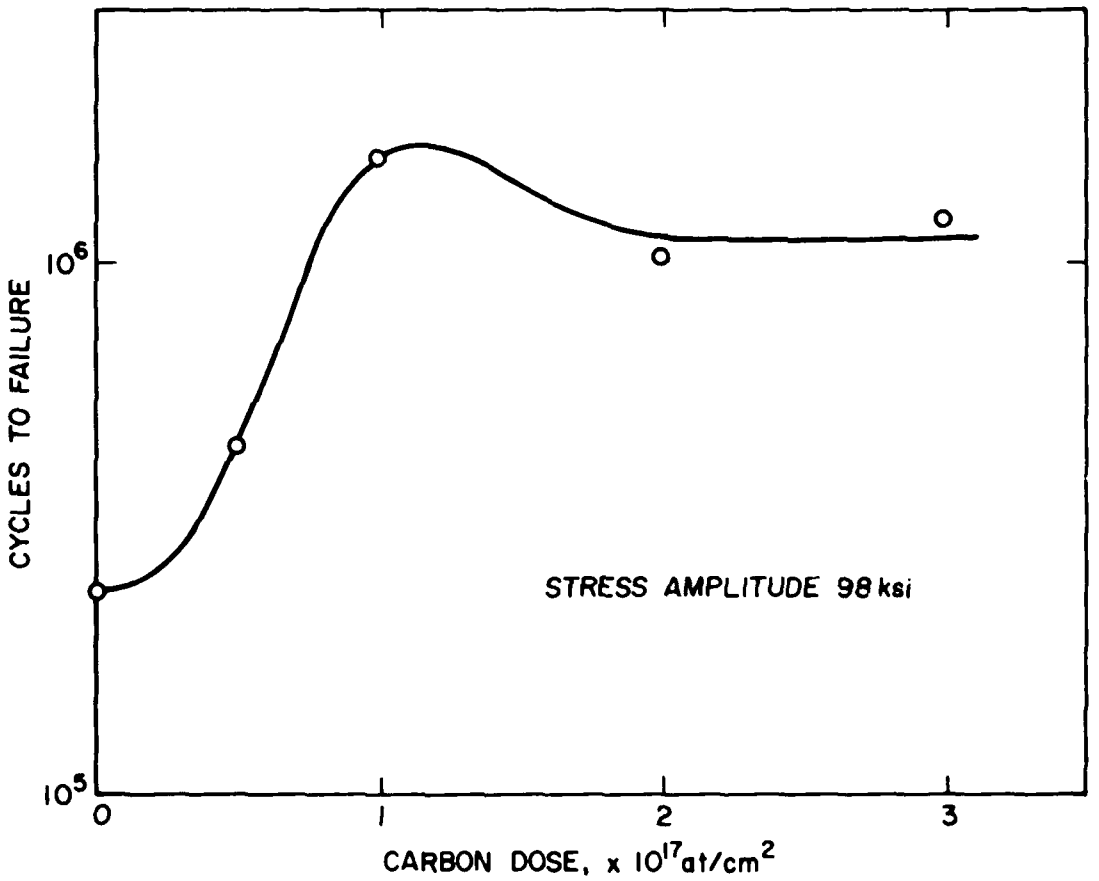

Fig. 4 — Cycles to failure vs. implanted carbon dose, mill annealed Ti-6Al-4V samples.

Section III.A

CORROSION CONTROL BY ION IMPLANTATION

E. McCafferty,[1] G. K. Hubler,[2] and J. K. Hirvonen[2]

[1]Advanced Materials Technology Branch
Material Science and Technology Division

[2]Materials Modification and Analysis Branch
Radiation Technology Division
Naval Research Laboratory

This work was suported by the Naval Air Propulsion Center, Trenton, N.J.
and the Office of Naval Research

CORROSION CONTROL BY ION-IMPLANTATION

E. McCafferty, G. K. Hubler, and J. K. Hirvonen
Naval Research Laboratory, Washington, DC 20375

ABSTRACT

An exciting new approach to corrosion control is the modification of the surface of metals by ion implantation. Ion implantation is a process by which high velocity ion beams of any desired alloying element are bombarded into the surface region of the substrate metal. The Naval Research Laboratory is involved in a broad research program on the application of ion implantation for the improvement of material properties, including resistance to aqueous corrosion. This paper outlines the characteristics and advantages of the ion implantation method and illustrates the approach with two examples of corrosion research in progress at the Naval Research Laboratory. The first of these is a fundamental study on the effect of implanted palladium on the corrosion of titanium in hot, concentrated acids. Implanted Pd reduces the corrosion rate of Ti by a factor of 1,000, with the improvement due to retention of Pd at the surface. The second example is a practical study on the use of ion implantation to improve the corrosion resistance of bearing alloys used in aircraft engines. Preliminary results indicate that Cr implantation substantially reduces pitting corrosion of M50 steel in chloride-contaminated lubricating oil.

Introduction

Aqueous corrosion is caused by electrochemical reactions occurring at the metal surface. One method of corrosion control is to introduce by alloying elements which improve the inherent thermodynamic stability of the surface, or promote the formation of protective films. One general problem with bulk alloying is that elements which improve corrosion resistance may not be those which give the desired structural properties of the material. In many cases this problem can be surmounted through the use of inhibitors or surface treatment techniques. Ion implantation is a new method of surface treatment in which high velocity ion beams of any desired alloying element are bombarded into the surface region of the substrate metal. Ion implantation offers the advantage of modifying the surface composition without altering bulk properties because the implanted region is typically only hundreds to thousands of angstroms deep.

Despite the rapid acceptance of ion implantation in some fields, such as in the manufacture of semiconductor devices (1), comparatively little attention has been paid the possibility of controlling aqueous corrosion by means of ion implantation.

The purpose of this paper is to provide some background on the ion implantation method and to illustrate the approach with two examples of corrosion research in progress at the Naval Research Laboratory. One of these examples is a laboratory investigation on the implantation of palladium into titanium. The second is a more practical study on the use of ion implantation to improve the corrosion resistance of M50 alloy bearings used in aircraft engines.

The Ion Implantation Method

Ion implantation is a process by which virtually any element can be injected into the near-surface region of any solid by means of a beam of high-velocity ions (usually tens to hundreds KeV) striking a target mounted in a vacuum chamber.

Figure 1 is a schematic representation of the Naval Research Laboratory ion implantation apparatus. Atoms of the desired species are ionized in the ion source and injected into an acceleration stage. Since many ions in addition to the desired species are accelerated, an ion analysis magnet is necessary to separate the desired ions. Further down the beam line the ion beam is rastor scanned by means of electrostatic deflection plates to ensure that a uniform distribution of atoms is implanted laterally along the surface. By collecting the ion current at the target in a Faraday cage, and by knowing the area over which the beam is scanned, the number of ions implanted can be measured (usually quoted in units of ions/cm^2). The target chamber is equipped to either heat or cool the substrates during implantations which are carried out in a vacuum of about 10^{-6} Torr. The NRL ion implantation facilities consist of a 200-KeV implanter and a 5-MV Van de Graaff accelerator. The maximum area which can presently be implanted at one time is a 2-inch x 2-inch area. A second, commercially manufactured, production-type ion implantation apparatus currently being installed is expected to implant areas as large as 10 square inches.

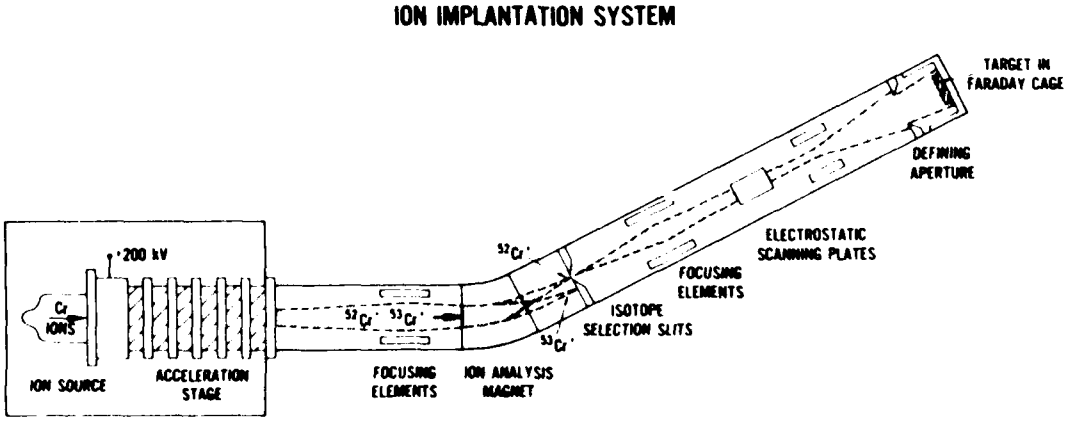

Fig. 1. The Naval Research Laboratory ion implantation system.

The bombarding ions lose energy in collisions with substrate electrons and atoms. Penetration depths of tens to thousands of angstroms are achieved before the incident ions lose all their energy and come to a stop. The depth of penetration depends on the accelerating voltage, type of ion, and nature of the substrate. The maximum concentration of implanted atoms is located beneath the substrate surface, and the depth-concentration profile usually follows a gaussian distribution. The surface concentration of implanted ions that can be achieved ranges from extremely dilute alloys to 50 atomic percent. Table 1 summarizes the various characteristics of the ion implantation process.

Some distinct advantages of ion implantation as used in corrosion science are that special alloys may be formed at the surface of a metal which inhibit corrosion, without the alteration of desired bulk properties. There is no problem with adhesion of the surface layer as there is with deposited coatings since there is no abrupt interface present between the implanted-alloy layers and the substrate. These and other advantages of the ion implantation method are summarized in Table 2.

The Naval Research Laboratory is currently involved in a broad program on the use of ion implantation to improve various properties of engineering materials. Some of the corrosion related aspects of that program are listed in Table 3.

Table 1 - ION IMPLANTATION PARAMETERS

Implanted elements	- Virtually any element from hydrogen to uranium can be implanted.
Ion energies	- Normally 2 to 200 KeV. Energies up to 5 MeV may be obtained with the Van de Graaff accelerator.
Implantation depths	- Vary with ion energy, ion species and host material. Ranges normally 100 angstroms to 10,000 angstroms.
Range distribution	- Approximately gaussian. Choice of energies allow tailored depth distribution profiles.
Concentration	- From trace amounts up to 50% or more.
Host material	- Any solid material can be implanted, including metals, semiconductors, and insulators.

Table 2 - ADVANTAGES OF ION IMPLANTATION

1. No sacrifice of bulk properties.
2. Solid solubility limit can be exceeded.
3. Alloy preparation independent of diffusion constants.
4. No coating adhesion problems since there is no interface.
5. No change in sample dimensions.
6. Depth concentration distribution controllable.
7. Composition may be changed without affecting grain sizes.
8. Precise location of implanted area(s).

Table 3 - RESEARCH ACTIVITIES AT THE NAVAL RESEARCH LABORATORY ON THE EFFECT OF ION IMPLANTATION ON AQUEOUS CORROSION

System	Applications	Investigators
Pd into Ti	Resistance to hot salt corrosion; resistance to crevice corrosion	E. McCafferty G. K. Hubler
Various ions into M50 alloy	Improve the pitting resistance of bearing alloys used in aircraft engines	J. K. Hirvonen W. Lucke G. K. Hubler R. Valori (NAPC) V. Agarwala (NADC) C. Clayton (SUNY)
N, Y, and Pt into Ti and Ti-6Al-4V	Improve fatigue lifetime	R. G. Vardiman T. W. Crooker R. A. Kant B. B. Rath
Various ions into aluminum alloys and high-strength steels	Improve resistance to pitting and general corrosion	E. McCafferty G. K. Hubler
Various ions into Fe foils	Reduce hydrogen permeation rate through Fe foils (hydrogen embrittlement)	M. Zamanzadeh (Penn State U.) H. W. Pickering (Penn State U.) G. K. Hubler

A Fundamental Study: Palladium Implanted Titanium

There have been but a few studies (2-4) on the effect of ion implantation on aqueous corrosion resistance. The system chosen for initial study in the Naval Research Laboratory program was palladium implanted into titanium. This model system was selected because it is well known that small additions of Pd in bulk alloys (0.1 atomic percent) produce a dramatic reduction in the corrosion rate of titanium in hot, concentrated acids (5,6).

Our results show that ion implantation with palladium reduces the corrosion rate of titanium by a factor of about 1,000. This improvement suggests applications where crevice corrosion, with its concomitant local acidity (7), would be a problem. Indeed, palladium-titanium bulk alloys have better crevice corrosion resistance than titanium in hot chloride solutions (8,9).

This section will present some of the results of this investigation. More detail is provided elsewhere (10,11). Samples of pure titanium rod (3/8 inch diam.) were mounted in epoxy molds and polished to a mirror finish. These surfaces were implanted with palladium to a fluence of 1×10^{16} ions/cm^2 at an energy of 90 KeV. The resulting palladium concentration profile was approximately gaussian shaped and centered at a depth of 240 angstroms beneath the titanium surface. The concentration of palladium at that depth was 5 atomic percent, with less than 0.1 atomic percent Pd at the titanium surface.

Figure 2 shows electrode potentials *vs.* Hg/Hg_2SO_4 as a function of immersion time for pure Ti, pure Pd, and Pd-implanted Ti samples in boiling 1M H_2SO_4. The time axis is plotted logarithmically for illustration purposes only. The steady-state open-circuit corrosion potential of palladium is approximately 1000 mV more noble than that of pure titanium. The steady-state corrosion potential of the implanted sample is much closer to that of pure palladium than that of pure titanium. Moreover, in the first few minutes of immersion, the implanted samples showed a rapid shift from an electrode potential near that of pure Ti to a potential close to that for pure Pd. After 1 minute in the case of two of the implanted samples and after 1.5 minutes for a third, the electrode potential was -1.0 volts *vs.* Hg/Hg_2SO_4 and tending toward the potential of pure titanium. In the next few seconds in each case, however, the electrode potential reversed toward the noble direction as the Ti-rich surface dissolved away to expose a new surface region containing an increased concentration of Pd.

The buildup of palladium at the surface during the corrosion process was determined by Rutherford backscattering of helium ions. This is a technique in which a beam of monoenergetic helium ions is allowed to impinge on a surface at a constant angle. The number of backscattered helium ions collected for a given number of incident ions is proportional to the concentration of dopant atoms which cause the scattering. The energy of backscattered particles can be related to the depth of the dopant atom.

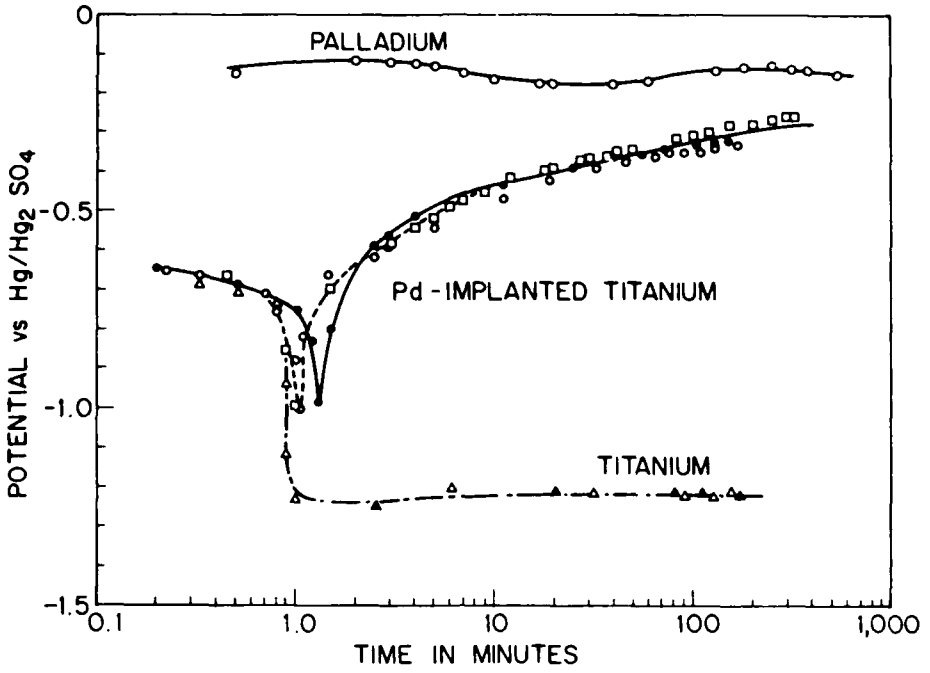

Fig. 2. Open-circuit corrosion potentials as a function of immersion time in boiling 1M H_2SO_4 for pure titanium, pure palladium, and palladium-implanted titanium.

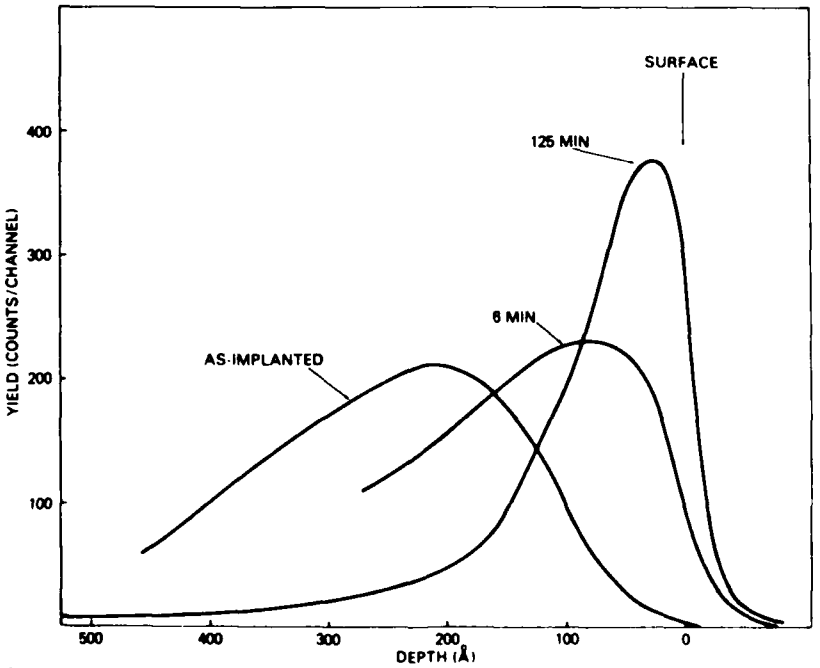

Fig. 3. The energy spectrum of helium ions backscattered from ion-implanted Pd in pure Ti for an implanted sample and after two different immersion times in boiling 1M H_2SO_4.

Figure 3 shows backscattering depth-concentration profiles for an as-implanted sample and for samples corroded for two different immersion times. The increased peak height in the Pd profile with time indicates that Pd is being built up at the surface. The area under the curves, which is proportional to the total amount of Pd retained in the sample, is the same for all three curves indicating that no Pd is lost during the corrosion process. The maximum surface concentration of Pd built up during this process was about 20 percent. In the longest experiment run to date, Pd was retained for as long as 8 hrs.

Figure 4 shows potentiostatic anodic polarization curves for pure titanium, pure palladium, and palladium-implanted titanium in boiling 1M H_2SO_4. All curves were determined after steady-state open circuit potentials were first established (2 to 2-1/2 hrs. immersion). The anodic curve for pure titanium shows the normal active-passive behavior which has been typically observed (5,6,12). Well defined Tafel slopes were not observed in the active region, but the corrosion rate at the open-circuit potential was determined by colorimetric analysis of solution to be 3.7 mA/cm^2, on the basis that the overall anodic reaction is $Ti \longrightarrow Ti^{+3} + 3e^-$ (12). The implanted samples display a passive current density of 2 to 6 $\mu A/cm^2$, which may be estimated to be the corrosion rate at the open-circuit potential. Thus, implantation with Pd lowers the corrosion rate of Ti by a factor of about 1,000.

To summarize this section, ion implantation of titanium with palladium reduces the open-circuit corrosion rate in boiling 1 M sulfuric acid by a factor of about 1,000. The open-circuit corrosion potential is shifted approximately 0.9 volts in the noble direction and is a mixed potential between pure titanium and pure palladium. Electrochemical measurements and Rutherford backscattering analysis indicate that the improvement is due to the initial preferential dissolution of titanium and the retention and buildup of implanted palladium.

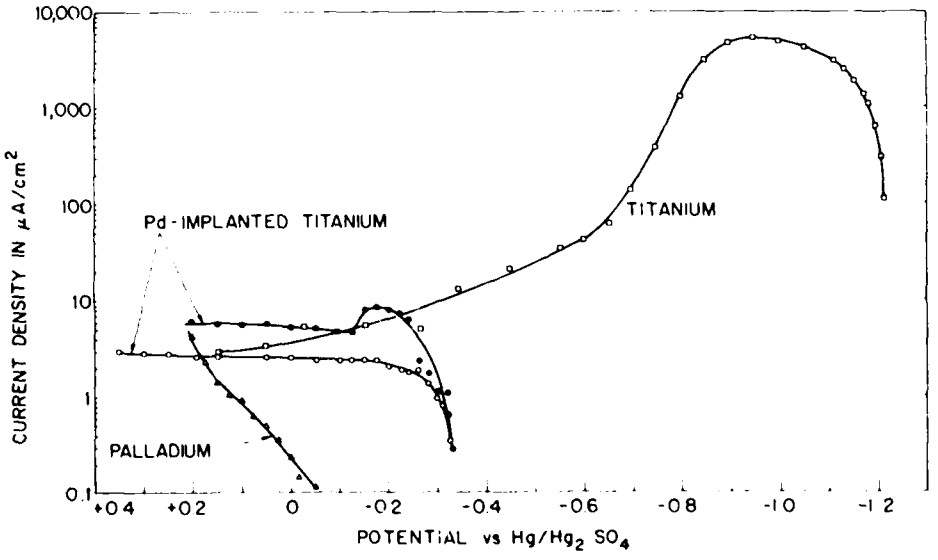

Fig. 4. Anodic polarization curves for titanium, palladium, and palladium-implanted titanium in boiling 1M H_2SO_4.

An Application: Corrosion-Resistant Bearings

Pitting corrosion in M50* alloy steel bearings used in turbojet engines has been found to be a severe problem. The difficulty arises when salt spray condensate accumulates in the engine lubricants of aircraft not in use. The Naval Research Laboratory has recently begun a cooperative program with the Naval Air Propulsion Center (Trenton, N.J.) to improve the corrosion resistance of bearing alloys by ion implantation. This section will describe the preliminary results and will outline work to be done in the near future.

Initial work demonstrated that implantation did not degrade the rolling contact fatigue lifetime of the material as has been found for some coatings. The fact that implantation produces no macroscopic dimensional changes and can be applied to otherwise finished components are two additional reasons that ion implantation appears potentially advantageous for this application.

Figure 5 shows the arrangement of a laboratory-simulated field service test. The cylindrical surface resting on the flat side of the upright cylinder is intended to simulate a roller bearing-on-race geometry. The cylinders were positioned in place and were totally immersed for 2 hrs. in oil contaminated with 3 ppm chloride. While still in place, the two parts were removed from the oil and allowed to drip dry. A meniscus of contaminated oil was retained between the two parts, as shown in Fig. 5. The two parts with the meniscus intact were exposed to alternate cycles of moist air at 100°F (8 hrs.) and 4°F (16 hrs.) for a total of 2 weeks.

When both the flat and cylindrical surfaces were unimplanted M50 alloy, there was severe corrosion, as shown in Fig. 6, which is a top view photograph of the flat surface. The attack occurs in two areas - in a line of pits underneath the line of contact between the cylindrical and flat surfaces, and in the thin layer of oil outside this region. As seen in the figure, the attack in both regions was substantially reduced when the surfaces were ion implanted with Cr to produce a surface concentration of 20% to 25%. (See Fig. 6).

Future work will involve corrosion testing the following implantations into M50 steel:

Mo, Mo+Cr, Ni, Ta, Ti, Al, Re, P+Cr.

The choice of ions to be implanted includes those species (such as Mo) known to improve pitting resistance of conventional alloys as well as some (e.g., Ta) which form corrosion resistant metastable alloys incapable of being produced by conventional metallurgical means. The optimization of implantation parameters (e.g., ion species, ion dose (concentration), and energy) will be determined by a combination of conventional electrochemical characterizations of implanted surfaces as well as further simulated field service corrosion tests. Selected ions which are promising will finally be implanted into actual (spherical) bearings. As a corollary investigation, selected ions from the above list will also be implanted into selected gear alloys such as case-hardened 9310 steel.

---

*Nominal composition of alloying elements: 4%Cr, 4%Mo, 1%V.

1. Test pieces (both M50 alloy steel) were placed in contact as indicated by the dotted line.

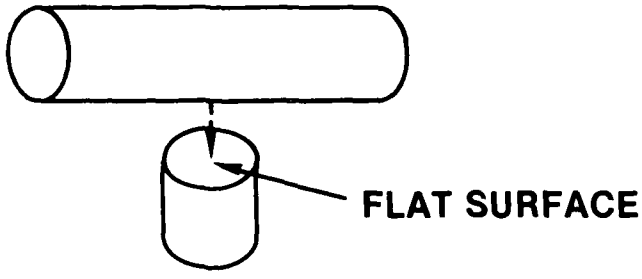

2. Both pieces in place were immersed in chloride-contaminated oil for 2 hrs., removed, and allowed to dry.

3. A meniscus of contaminated oil was retained between the two parts:

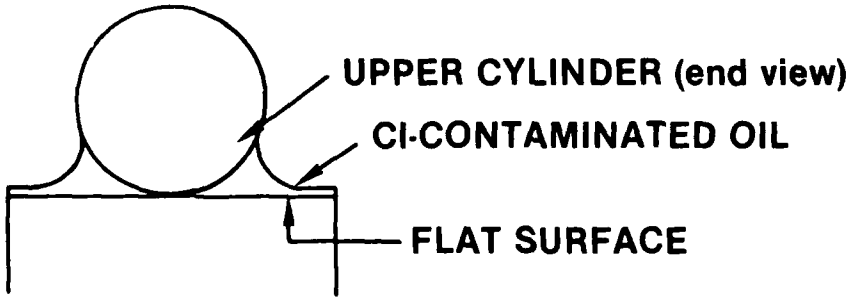

4. The above arrangement was exposed to moist air cycled between 100°F and 4°F for 2 weeks.

Fig. 5. Laboratory-simulated field service test of corrosion of bearings.

PROBLEM: PITTING CORROSION IN M50 ALLOY BEARINGS

APPROACH: PRODUCE CORROSION-RESISTANT SURFACE ALLOYS BY ION IMPLANTATION

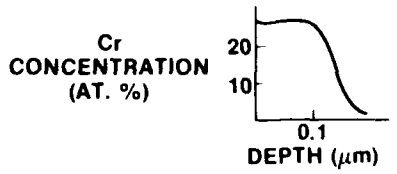

RESULTS: M50 SURFACES FOLLOWING SIMULATED FIELD SERVICE TEST

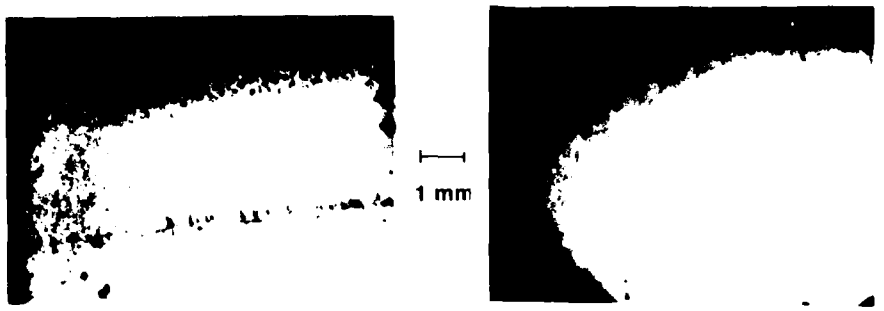

Fig. 6. Results of the tests outlined in Fig. 5. When both parts were the M50 alloy, the flat surface suffered severe localized attack. A line of pits was located at the meniscus center, and additional pitting was observed in the thin layer near the edge of the flat surface. Ion implantation with Cr eliminated both areas of attack (right photograph).

Summary and Prospectus

The characteristics and possible advantages of the ion implantation process have been outlined in this paper. Two examples of ongoing corrosion research at NRL have been given. The first of these, the Pd-implanted titanium work, has been primarily directed toward gaining a better fundamental understanding of the effect of implantation on a well-characterized system, although there may be applications in improving the hot salt corrosion resistance and crevice corrosion resistance of titanium alloys. The second study, which is still in its preliminary stages, is more applied and is specifically aimed at improving the corrosion resistance of bearing alloys presently used in aircraft engines.

It is too early to assess the utility of the ion implantation approach for controlling aqueous corrosion. Initial applications will most likely involve small critical parts, such as bearings, or perhaps special parts such as within crevices, screw threads, or the like. Although ion implantation equipment technology is presently capable of being scaled up for large size components, it remains to be seen if there is both scientific merit and economic justification for such development for corrosion control. In addition to these applications, however, the ability to implant various ions into the metal surface offers a unique research tool for a better understanding of corrosion mechanisms.

References

(1) See, for example: Dearnaley, G. F., Nelson, J. H., and Stephen, J., "Ion Implantation," North-Holland Publishing Co., 1973.

(2) Ashworth, V., Baxter, D., Grant, W. A., and Proctor, R. P. M., Corrosion Sci., 16, 775 (1976).

(3) Covino, B. S., Jr., Sartwell, B. D., and Needham, P. B., Jr., J. Electrochem. Soc., 125, 366 (1978).

(4) Covino, B. S., Jr., Needham, P. B., Jr., and Conner, G. R., J. Electrochem. Soc., 125, 370 (1978).

(5) Stern, M. and Wissenberg, H., J. Electrochem. Soc., 106, 759 (1959).

(6) Tomashov, N. D., Altovsky, R. M., and Chernova, G. P., J. Electrochem. Soc., 108, 113 (1961).

(7) Brown, B. F., Corrosion, 26, 249 (1970).

(8) Griess, J. C., Jr., Corrosion, 24, 96 (1968).

(9) Takamura, A., Corrosion, 23, 306 (1967).

(10) McCafferty, E. and Hubler, G. K., J. Electrochem. Soc., 125, 1892 (1978).

(11) Hubler, G. K. and McCafferty, E., "The Corrosion Behavior and Rutherford Backscattering Analysis of Palladium-Implanted Titanium," paper presented at the Conference on "Ion-Implantation and Ion Beam Analysis Techniques in Corrosion," Manchester, England, June 28-30, 1978 (to be published).

(12) Kelly, E. J., "Proceedings of the Fifth International Congress on Metallic Corrosion," Tokyo, 1972, p. 137, N.A.C.E., Houston, Texas (1974).

Acknowledgments

The authors are pleased to acknowledge the interest and financial support of R. Valori of the Naval Air Propulsion Center, Trenton, N.J., and of Phillip A. Clarkin of the Office of Naval Research.

Section III.B

APPLICATION OF ION IMPLANTATION FOR THE IMPROVEMENT OF LOCALIZED CORROSION RESISTANCE OF M50 BEARING STEEL

Y. F. Wang,[1] G. R. Clayton,[1] G. K. Hubler,[2]

W. H. Lucke,[2] and J. K. Hirvonen[2]

[1]Department of Materials Science and Engineering
State University of New York at Stony Brook
Stony Brook, N.Y.

[2]Materials Modification and Analysis Branch
Radiation Technology Division
Naval Research Laboratory

This work was supported in part by the Office of Naval Research (SUNYSB) and by the Naval Propulsion Test Center, Trenton, N.J. (NRL)

Thin Solid Films, 63 (1979) 11–18

APPLICATIONS OF ION IMPLANTATION FOR THE IMPROVEMENT OF LOCALIZED CORROSION RESISTANCE OF M50 BEARING STEEL*

Y. F. WANG AND C. R. CLAYTON

Department of Materials Science and Engineering, State University of New York at Stony Brook, Stony Brook, N.Y. 11794 (U.S.A.)

G. K. HUBLER, W. H. LUCKE AND J. K. HIRVONEN

Radiation Technology Division, U.S. Naval Research Laboratory, Washington, D.C. 20375 (U.S.A.)

(Received April 13, 1979, accepted April 25, 1979)

Pitting corrosion of M50 alloy steel bearings used in turbojet engines has been found to be a severe problem. The difficulty arises when salt-spray condensates accumulate in the engine lubricants of aircraft not in regular use. Ion implantation was applied to this problem because in the early stages of this work it was shown to be able to maintain both the dimensional stability and the contact fatigue lifetime of the M50 bearings.

Qualitative tests, which simulated the geometry and thermal cycle conditions leading to pitting of the M50 bearing surface, were performed using oil containing 3 ppm NaCl. Initially it was found that chromium surface alloys containing 20–25% chromium substantially reduce the level of attack. Prior to further corrosion simulation tests, potentio-kinetic studies were carried out on M50 implanted with chromium, molybdenum and titanium in order to screen both the passivating tendency of the surface alloys formed and their resistance to localized forms of corrosion. Singular additions of chromium, molybdenum and titanium were found to increase the resistance of M50 to localized breakdown significantly. The highest resistance to localized breakdown was found for a multi-implantation of chromium and molybdenum.

1. INTRODUCTION

Pitting corrosion of M50 alloy steel bearings used in turbojet engines has been found to be a severe problem. The difficulty arises when salt-spray condensates accumulate in the engine lubricants of aircraft not in regular use. Ion implantation was applied to this problem because in the early stages of this work it was shown to be able to maintain both the dimensional stability and the rolling contact fatigue lifetime of the M50 bearing alloy.

Qualitative tests, which simulated the geometry and thermal cycle conditions leading to pitting of the M50 bearing surface, were performed using oil containing 3 ppm NaCl. These experiments consisted of putting two cylindrical bearings in contact with one another as shown in Fig. 1. Pitting was found to occur along the line of contact between the cylinders and general staining occurred outside the

*Paper presented at the International Conference on Metallurgical Coatings, San Diego, California, U.S.A., April 23–27, 1979.

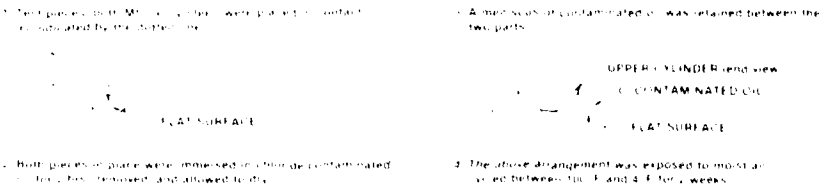

Fig. 1. Laboratory-simulated field service test of the corrosion of bearings.

meniscus of the (contaminated) oil. In a first attempt to apply ion implantation to this problem both specimens were implanted with chromium to a fluence of 10^{17} ions cm^{-2} at 75 keV. Figure 2 shows that pitting was totally prevented in the implanted surfaces after 4 weeks of this simulated field test, whereas considerable pitting had occurred in the unimplanted bearing surface after the same period of time.

(a) (b)

Fig. 2. Optical photographs of the flat surfaces of M50 test samples after a simulated field service test: (a) The unimplanted sample shows generalized corrosion outside the oil meniscus region and pitting under the line of contact; (b) The chromium implanted sample shows complete immunity. (Magnification: 6×.)

Prior to further corrosion simulation tests, potentio-kinetic studies were carried out on M50 implanted with chromium, molybdenum and titanium as a first stage in screening both the passivating tendency of the surface alloys formed and their resistance to localized forms of corrosion.

It has long been established that small percentages (less than 5 at %) of molybdenum added to stainless steel markedly reduces susceptibility to pitting and crevice corrosion in chloride solutions[1–5]. In our studies we considered double implantation of chromium and molybdenum to see if M50 would benefit from the synergic behavior found between molybdenum and chromium in conventional stainless steels. In addition to this we considered separate implantation of chromium, molybdenum and titanium. Titanium was chosen because its alloys are known to have good localized corrosion resistance.

2. EXPERIMENTAL

2.1. *Material*

The composition of the M50 steel is given in Table 1. The steel was produced by vacuum induction melting followed by vacuum remelting to form a homogeneous alloy.

TABLE I
PERCENTAGE COMPOSITION OF M50

Element	*Amount* (%)	*Element*	*Amount* (%)
Carbon	0.80–0.85	Molybdenum	4.00–4.50
Manganese	0.15–0.35	Vanadium	0.90–1.10
Silicon	0.10–0.25	Nickel	0.15 max
Phosphorus	0.015 max	Cobalt	0.25 max
Sulfur	0.010 max	Tungsten	0.25 max
Chromium	4.00–4.25	Copper	0.10 max

2.2. Ion implantation

Samples were cut from M50 rods of diameter $\frac{3}{8}$ in with a silicon carbide cut-off wheel to produce "buttons" $\frac{1}{4}$ in tall. One end of the button was polished with 600 grit paper and given a final mirror finish with 0.3 μm γ-alumina polish. The samples were then degreased in acetone, cleaned in detergent solution and washed in distilled water. The dried samples were then ion implanted. The implantation procedure has been outlined in ref. 6. The fluences and energies used are given in Table II.

TABLE II
FLUENCES AND ENERGIES OF IONS IMPLANTED IN M50 STEEL

Sample	*Ion*	*Fluence* (ions cm^{-2})	*Energy* (keV)
Cr (H_2SO_4)	Cr	2×10^{17}	150
Cr (Cl test)	Cr	1.5×10^{17}	150
Mo	Mo	5×10^{16}	100
Ti	Ti	2×10^{17}	85
Cr, Mo	Cr	1.5×10^{17}	150
	Mo	5×10^{16}	100

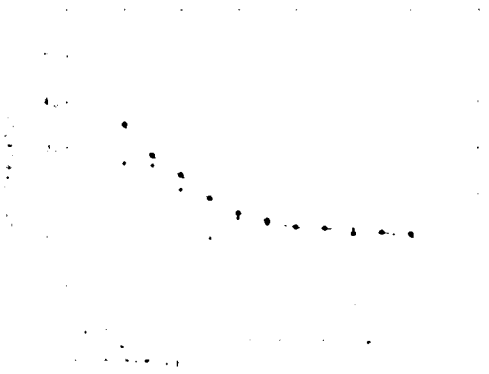

Fig. 3. Profiles of chromium in the chromium-implanted M50 alloy obtained by ESCA using argon ion etching. 75 keV Cr^+ ions. ●, 10^{17} ions cm^{-2}; ▲, 2×10^{17} ions cm^{-2}; base rate.

Figure 3 shows the implant distribution of chromium in M50 for fluences of 10^{17} and 2×10^{17} ions cm^{-2}. These profiles were obtained with electron spectroscopy for chemical analysis (ESCA) using argon ion etching (4 keV current,

20 μA; base pressure, 10^{-6} Torr). Sensitivity factors relating to the relative photoelectron cross section of the $2p^{3/2}$ suborbitals of iron and chromium were used to normalize the peak heights and enable, therefore, a semiquantitative determination of the concentrations of iron and chromium in the surface alloy[7]. To account for the incipient chromium in the M50, a plot of the ratio of chromium to iron found in the M50 is plotted with the profiles. The profiles show that a high concentration of chromium (greater than 20 at.%) is achieved in the first few hundred ångströms. Further work to determine implant distributions is being carried out.

2.3. *Anodic polarization studies*

2.3.1. *Active passive behavior*

Anodic polarization was carried out in hydrogen-saturated 1 N sulfuric acid solution at 26°C using a conventional Greene cell. The samples were masked with epoxy resin to prevent attack on unimplanted surfaces. All potentials were recorded relative to the saturated calomel electrode (SCE). Removal of the air-formed film was achieved by charging at −300 mV below the open-circuit potential E_c for 10 min. Samples were then allowed to stabilize at open-circuit. This usually took approximately 5 min. Anodic scanning then followed at 1 mV s^{-1}.

2.3.2. *Localized breakdown in chloride solution*

A similar procedure was carried out in CH_3COOH–CH_3COONa solutions (also hydrogen saturated) in a range of pH from 4 to 6 to determine a solution pH where M50 shows an extensive passive range. A solution of pH 6 produced a very small active range and an extensive range of passivity. To this solution 0.1 M NaCl was added so that breakdown potentials due to localized attack by chloride ions, by either crevicing or pitting, could be determined. Anodic sweeps were carried out at 1 mV s^{-1}. The surfaces were then examined by optical microscopy or scanning electron microscopy (SEM).

3. RESULTS AND DISCUSSION

The polarization curves are shown in Figs. 4 and 5 and the salient features of the anodic kinetics and the breakdown potentials for the chloride solution are given in Table III.

TABLE III
PASSIVE CURRENT DENSITIES AND BREAKDOWN POTENTIALS

Sample	E_c (mV)	E_b (mV)	I_{pc} (μA cm^{-2})
M50	673	225	3.0×10
Cr	555	+125	3.3×10
Mo	540	+55	2.0×10^{2}
Ti	628	0	5.2×10
Cr, Mo (I)	97	+1225	1.7×10
			2.3×10
Cr, Mo (II)	360	+450	4.3×10

3.1 *Active passive behavior*

The M50 curve shows a broad active anodic peak which is characteristic of the

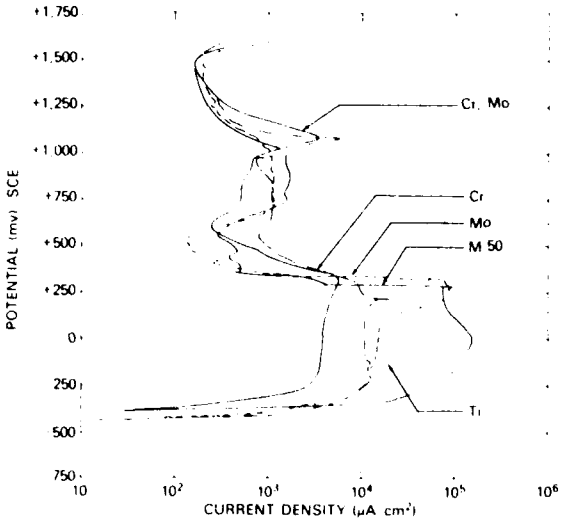

Fig. 4 Potentio-kinetic anodic polarization curves produced in hydrogen-saturated 1 N H_2SO_4 for M50 steel, and for M50 steel implanted with titanium, chromium, molybdenum and chromium + molybdenum.

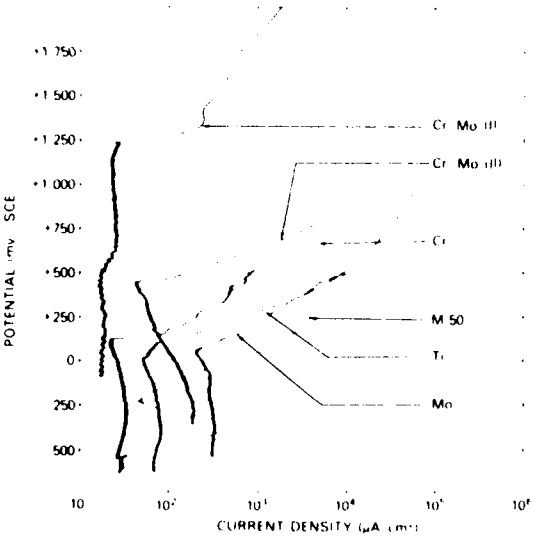

Fig. 5 Potentio-kinetic anodic polarization curves produced in a buffer solution of pH 6 containing 0.1 M NaCl for M50 steel, and for M50 steel implanted with titanium, chromium, molybdenum and chromium + molybdenum.

limiting current behavior usually attributed to the formation of an ionic diffusion layer or a non-protective salt layer. In the case of M50 this appears as a black voluminous deposit. This film remained at the onset of passivity. At around + 470

mV the black film is seen to breakdown and reform. This corresponds to a small anodic current maximum and is accompanied by a reduction in the passive current density. At +550 mV an increase in current density is observed which terminates at +750 mV in a stable region of passivity. The transpassive region was characterized by oxygen evolution only. No evidence of chromium dissolution was observed, which may indicate that the chromium in M50 is largely tied up.

Pure titanium is known to be active in deaerated sulfuric acid[8]. The passive film requires both oxygen and water for it to form. When alloyed to M50, titanium appears to dominate the anodic behavior because no passive range was observed.

Molybdenum was seen to alter the shape of the active peak. In addition to this the surface remained shining up to +125 mV, when black spots of deposit were observed prior to the sudden formation at the passive potential of a black film. This film eventually failed at 1250 mV, prior to the onset of oxygen liberation. In the passive region molybdenum was seen to reduce the passive current density.

Chromium was found to reduce the critical current density in the active region by nearly one order of magnitude. The shape of the active peak was similar to that of M50. The surface alloy produced a single passive region which extended up to +975 mV where chromium dissolved transpassively. The benefit of chromium addition was obvious from the permanent shining surface of the sample prior to transpassive pitting.

The double-implanted surface alloy of chromium and molybdenum produced a single passive region and a transpassive peak, effects both attributable to chromium. Again the shape of the active peak was broad. However, unlike the separate chromium and molybdenum surface alloys, an increase in the Tafel slope for active dissolution was observed for this alloy. This produced a greater reduction in the limiting current density than achieved in the separate chromium and molybdenum surface alloys. Of course this may be due to the relative dilution of iron. Surface analysis of these alloys will soon be carried out.

3.2. Anodic polarization in CH_3COOH–CH_3COONa buffered at pH 6 + 0.1 M NaCl

It can be seen in each curve that alloying removed the active nose observed for the M50 sample. All alloys self-passivated in this solution. The passive film formed on M50 in this solution is seen to break down rapidly at −225 mV. In every case examined the surface alloy was seen not only to form a passive film more readily at pH 6 but also to produce a film more stable to chloride ion attack. The breakdown potentials E_b and passive current densities I_{ps} are given in Table III. It can be seen from the breakdown potentials that the resistance of the M50 surface decreased according to the alloying elements in the following way: Cr,Mo > Cr > Mo > Ti > M50. In general it was found that the breakdown potential observed corresponded to crevice corrosion at the epoxy resin alloy interface rather than to pure pitting. However, pits were observed in all but one of the systems studied. A discrimination between pitting potentials and crevice potentials cannot therefore be made in this work. However, the experiments do give a preliminary guide to the resistance to chloride ion attack of the passive films formed by the surface alloys. It was observed that the metal–epoxy resin interface of chromium surface alloys was seriously attacked by crevice corrosion and by a small number of pits at the center. Only pits were observed for molybdenum surface alloys.

i.e. chromium seemed to improve the resistance to pitting and molybdenum prevented crevice corrosion of the samples. It was reasonable to expect the Cr, Mo double-implanted surface alloy to have a good resistance to localized corrosion. Indeed, it would appear that Cr, Mo double implantation produced the surface alloy most protective against localized corrosion. Two curves are shown for the Cr, Mo surface alloy. The first sample did not break down until + 1225 mV, when it crevice corroded at a region of the epoxy resin/surface alloy interface. A SEM micrograph of this attack is shown in Fig. 6. No other attack was observed even at higher magnification. It was noticed that minor fluctuations were observed in the current density in all the implanted M50 samples, probably due to rapid breakdown and repair of the passive film. It is interesting to note that the fluctuation in the passive density becomes more rapid at about + 625 mV in the Cr, Mo (I) surface alloy, corresponding to a second passive film region. In case (II) breakdown was at 50 mV below the transition to the second passive region. This may indicate that the irreproducibility lies in part in the inability of sample (II) to form the second modified region of passivity.

Fig. 6. A SEM micrograph showing crevice corrosion at the Mo, Cr surface/epoxy resin interface in a buffer solution of pH 6 containing 0.1 M NaCl solution. (Magnification 525 ×.)

It is clearly necessary to carry out more extensive surface analysis of these surface alloys before electrochemical analysis. In particular, analysis of the passive film is needed in order to interpret the observed anodic behavior.

4. CONCLUSIONS

Single high fluence (2×10^{17} ions cm^{-2}) implants of Cr^+ ions into M50 prevented pitting in a chloride-contaminated oil simulated field test.

All of the surface alloys produced by implantation in this work improved the localized corrosion resistance. The order of resistance to localized attack is given by Cr, Mo > Cr > Mo > Ti > M50.

The improvements in localized corrosion resistance in chloride solutions are caused by the improved resistance to chloride ion attack of the passive film formed on the surface of M50 at pH 6.

ACKNOWLEDGMENTS

This work was sponsored in part (SUNYSB) by the U.S. Office of Naval Research and in part (NRL) by the Naval Propulsion Test Center, Trenton, N.J. We gratefully acknowledge the equipment support of the National Science Foundation for the purchase of the V.G. ESCA 3MK2.

REFERENCES

1 H. H. Uhlig, *Corrosion and Corrosion Control*, Wiley, London, 1963, p. 272.
2 J. B. Lumsden and R. S. Staehle, *Scr. Metall.*, *6* (1972) 1205.
3 A. E. Yaniv, J. B. Lumsden and R. W. Staehle, in R. W. Staehle and H. Okuda (eds.), *Passivity and its Breakdown on Iron and Iron Base Alloys, U.S.A. Japan Seminar, Honolulu, 1975*, NACE, Houston, Texas, 1976, p. 72.
4 H. Okada, H. Oeawa, I. Itoh and H. Omata, in R. W. Staehle and H. Okuda (eds.), *Passivity and its Breakdown on Iron and Iron Base Alloys, U.S.A. Japan Seminar, Honolulu, 1975*, NACE, Houston, Texas, 1976, p. 82.
5 K. Sugimoto and Y. Sawada, *Corros. Sci.*, *17* (1977) 425.
6 G. Dearnaley, J. H. Freeman, R. S. Nelson and J. Stephen (eds.), *Ion Implantation*, North-Holland, New York, 1973.
7 J. E. Castle and C. R. Clayton, in R. P. Frankenthal and J. Kruger (eds.), *Passivity of Metals, Proc. 4th Int. Symp. on Passivity, Warrenton, Va., 1977*, The Electrochemical Society, Princeton, N.J., 1978, p. 714.
8 G. C. Palit and K. Elayaperumal, *Corros. Sci.*, *18* (1978) 162.

Section IV.A

REFRACTIVE INDEX PROFILES AND RANGE DISTRIBUTIONS OF SILICON IMPLANTED WITH HIGH ENERGY NITROGEN

G. K. Hubler,[1] P. R. Malmberg,[1] and T. P. Smith III[1]

[1]Materials Modification and Analysis Branch
Radiation Technology Division
Naval Research Laboratory

This work was supported by the Air Force Materials Laboratory
and the Naval Material Command

AD-A090 714 NAVAL RESEARCH LAB WASHINGTON DC F/G 13/8
THE USE OF ION IMPLANTATION FOR MATERIALS PROCESSING.(U)
OCT 80 F A SMIDT
UNCLASSIFIED NRL-MR-4341 NL

2 OF 2

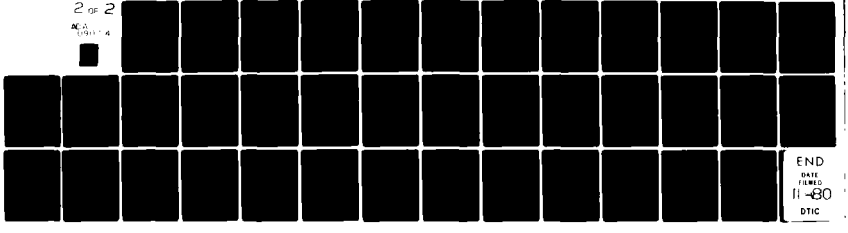

END
DATE FILMED
11-80
DTIC

Refractive index profiles and range distributions of silicon implanted with high-energy nitrogen

G. K. Hubler, P. R. Malmberg, and T. P. Smith, III[a]
Naval Research Laboratory, Washington, D.C. 20375

(Received 22 March 1979; accepted for publication 7 June 1979)

Single-crystal silicon has been implanted with nitrogen ions at MeV energies, to fluences between 0.25×10^{18} and 1.65×10^{18} ions/cm^2 at a substrate temperature of 700°C. Infrared transmission and reflection spectra in the range of 1.25–40 μm were measured and interference fringes were observed which are produced by the interference of light which has been multiply reflected between the front surface and the buried layers. By detailed theoretical analyses of the interference fringes we obtain refractive-index profiles, which, under suitable interpretation, provide accurate measurements of the range and straggling of the implanted ions. Rutherford backscattering measurements on the same samples confirm this interpretation. Between the energies of 0.67 and 3.17 MeV, the measured values of the projected range agree with theory after adjusting the electronic stopping power, but the straggling measurements are lower by ~30%. It is demonstrated that the asymmetry of the range distribution can be measured with this technique as well.

PACS numbers: 78.20. – e, 78.65.Jd, 61.80.Mk, 61.70.Tm

I. INTRODUCTION

The formation of silicon nitride by high-fluence implantation of nitrogen into silicon has been reported by several authors.[1–5] In these studies, samples were implanted at low energies (50–280 keV), were usually implanted with the substrate at room temperature, and subsequent annealing steps were used to promote silicon nitride formation. The resulting layers were studied by means of infrared absorption,[1–4] Rutherford backscattering,[2] optical microscopy,[4,5] and electron diffraction.[1,3]

This present work was begun with the intention of extending the previous studies to higher beam energies (~2 MeV). The higher energies were chosen to produce larger thicknesses of second-phase material which would simplify sample preparation and increase the sensitivity for all of the techniques mentioned above. High substrate temperatures (~700 °C) were used because it was thought that the high temperature would promote silicon nitride formation directly, without subsequent annealing.

A silicon sample was implanted with 1.5-MeV nitrogen ions to a fluence of 1.25×10^{18} ions/cm^2 at a substrate temperature of 700 °C. The infrared (*i-r*) transmission spectrum of this sample is shown in Fig. 1. The absorption band centered at 900 cm^{-1} is strong evidence for significant silicon nitride formation and has been observed by others.[1–4] However, the transmission spectrum also reveals large amplitude oscillations (30% peak-to-valley) between the wave numbers of ~1500 and 4000 cm^{-1} which are the result of the interference of light multiply reflected between the front surface and the buried implanted layer. At wave numbers less than ~1500 cm^{-1}, the dispersion caused by silicon nitride absorption distorts the periodicity and amplitude of the interference fringes.

The large amplitude fringes indicated that the refractive index of the buried layer was substantially different than that of pure silicon. It was decided to study the interference fringes in more detail, and to make silicon nitride formation a secondary objective. Therefore, questions regarding the microstructure and electrical properties of the implanted nitrogen layers will not be addressed here, and the discussion of ir spectra will be limited to wave numbers greater than about 2000 cm^{-1}, where it can be assumed that dispersion caused by the silicon nitride absorption band is negligible.

A series of samples were implanted with N ions to fluences between 2.5×10^{17} and 1.65×10^{18} ions/cm^2 and for energies betwen 0.67 and 3.17 MeV. The refractive-index profiles of the implanted layers were determined from least-square computer fitting of the interference spectra. The fitting function was a Gaussian-shape refractive-index profile which was shown to mirror the nitrogen concentration profile by means of Rutherford backscattering measurements. Therefore, the results of the computer fits were expressed as

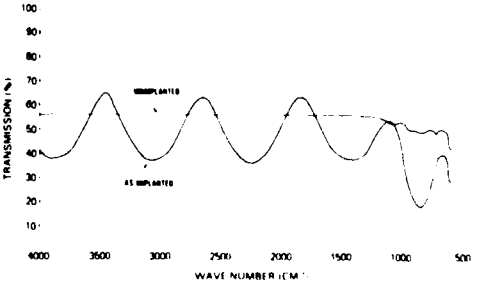

FIG. 1. Infrared transmission spectrum of unimplanted silicon, and silicon implanted with 1.25×10^{18} nitrogen ions/cm^2 at an energy of 1.5 MeV. The substrate temperature during implantation was 700 °C.

[a]Present address, 4443 Campus Ave #5, San Diego, CA 92116.

TABLE I. Characteristics of implanted layers as determined by computer fits to the i-r spectra

Sample fit[a]	Energy (MeV)	Fluence (10^{15}/cm^2)	R or I	R_p (μm)	ΔR_p (μm)	$n(R_p)$ (exp.)	k ($\times 10^{-4}$)	$n(R_p)$ (calc.)	Comments
1a	0.67	0.80	I	1.106	0.097	2.42	0.06	2.53	
1b			I	1.112	0.076	2.46	3.3		2000-8000 cm^{-1}, symmetric Gaussian
1c			I	1.161[b]	0.135[c] 0.045	2.40	0.82	2.45	2000-8000 cm^{-1}, asymmetric Gaussian, median of profile = 1.103 μm
2	0.67	1.00	I	1.065	0.089	2.22	0.05	2.28	
3	0.83	1.65	I	1.236			4.2		ΔR_p, $n(R_p)$ fixed, surface spallation
4	1.07	1.16	R	1.444 (1.451)[b]	0.105	2.27	0.42	2.31	
5	1.40	0.25	I	1.780	0.105	3.12	0.28	3.14	
6	1.40	0.60	I	1.770	0.096	2.79	0.25	2.72	
7	1.40	1.25	I	1.754	0.100	2.11	1.60	2.20	
8a	1.50	1.25	I	1.842	0.106	2.21	1.70	2.25	F = 1.014
8b			R	1.706 (1.715)[b]	0.107	2.11	0.31	2.26	1000 °C, 1 h anneal, HF wash, back surface lapped
9	3.17	0.53	I	2.989	0.114	2.88	0.25	2.87	F = 0.778
10a	3.17	1.55	I	2.963	0.113	1.93	0.38	2.12	
10b			R	2.941 (2.956)[b]	0.114	1.93	0.11	2.14	
						3.43			n of unimplanted silicon at 3000 cm^{-1}

[a] Number refers to sample, letter refers to fitting procedure.
[b] Depth of maximum refractive-index change where the two half-Gaussian distributions are joined (see text).
[c] Value of R_p corrected for 20° angle of incidence of reflection attachment.
[d] Standard deviations of the surface directed and bulk directed half-Gaussians, respectively (see text).

the nitrogen ion projected range R_p, and straggling ΔR_p. Good agreement is obtained between measured R_p values and stopping power theory when the electronic stopping power is arbitrarily adjusted to fit the data. Values of ΔR_p for the adjusted theory are about 40% higher than the measurements. It is also shown that the interference fringes are sensitive to the asymmetry of the range distribution as well. This is the first determination of implanted-ion range distributions by reflection interference-fringe analysis.

II. BACKGROUND

Thin film interference fringes in reflection and transmission spectra produced by ion implantation have been observed in both the visible[6] and infrared[7-11] wavelength regions. Crowder *et al.* used the spacing between fringe maxima and minima to determine the depth of disordered silicon layers produced by low-energy (approximately 280 keV) implants of Si, P, and As ions.[7-10] In that experiment, the ion fluence was sufficient to completely disorder silicon from the front surface down to a depth corresponding to the projected range of the implanted ions. The fringes arise from interference between light reflected by the front surface and light reflected at the disorder-to-crystalline interface. The latter reflection is produced by the discontinuity in the refractive index since the refractive index of disordered silicon is about 15% greater than that of crystalline silicon.[8] For light normally incident to the surface, the depth d of the reflecting interface is given by the simple expression

$$d = \frac{1}{2n}\frac{1}{L_1 - L_2}, \tag{1}$$

where n is the refractive index of disordered silicon and L_1 and L_2 are the wave numbers of two successive fringe maxima or minima. (Per usual convention, wave number is defined as the reciprocal of the wavelength in units of cm^{-1} and is proportional to the light frequency). Since phase terms entering into the thin-film interference equations are of the form $\exp(2\pi i dL)$, the interference fringes are a periodic function of wave number L.

Kachare *et al.* obtained data similar to that of Crowder for the systems nitrogen and phosphorous implanted into GaAs, and GaP[11,12] and Spitzer *et al.*[14] and Hubler *et al.*[5] have obtained fringes for phosphorus and silicon implanted into silicon. Kachare *et al.* extended the interference-fringe analysis further by fitting a thin-film interference model for three layers to the data. Layer 1 was air, layer 2 was the disordered substrate, and layer 3 was the semi-infinite crystalline substrate, with an infinitely thin boundary layer between the crystalline and disordered regions. Good fits were obtained with this model and they were able to extract the thickness of the disordered layer and its refractive index. However, the refractive index of layer 3 required to give these fits did not agree with the refractive index of crystalline silicon. The authors attributed this to the possibility that the data were sensitive to the fact that the disorder-to-crystalline interface is not abrupt, but changes smoothly between ordered and disordered material over a finite dimension. This suggestion was shown to be correct when Hubler *et al.*[5] connected the disorder/crystalline material smoothly with a half-Gaussian refractive-index shape and obtained good fits to i-r reflection data for phosphorus and silicon implanted silicon and for a substrate refractive index equal to that of silicon.

In the work reported here a high substrate temperature was used during implantation which maintained the silicon in the crystalline state down to the depth of the implanted nitrogen ions. Therefore, the fringes in Fig. 1 are due to reflection from a buried layer whose index of refraction has been changed from that of pure crystalline silicon in contrast

to the data of Crowder *et al.*, Kachare *et al.*, and Hubler *et al.* which represent a uniform layer out to the surface. Equation (1) is still approximately valid to estimate the depth of the implanted ions because most of the optical path is through the Si cover layer and the width of the buried layer is small compared to its depth.

III. EXPERIMENTAL PROCEDURES

Implantations were carried out on the NRL 5-MV Van de Graaff accelerator at six particle energies between 0.67 and 3.17 MeV into the ⟨111⟩ face of 0.38-mm-thick float-zone single crystals of silicon. The silicon was 10-Ω cm resistivity, p-type, and electropolished by the manufacturer leaving a mirror finish on both sides. The conditions for these implants may be found in Table I. Because the molecular N_2^+ beam was more abundant than the monatomic, the molecular beam was used for all energies except the 3.17-MeV implant (where accelerator voltage limitations made use of the N^+ ion beam necessary). Samples were heated by the power in the ion beam ($\simeq$ 5–15 W). Heat loss was controlled by varying the heat shielding. For low power the sample was almost completely wrapped with two layers of 0.025-mm tantalum except for a window for the beam, whereas at high power there was minimal heat shielding. Adjustment of temperature for each shielding condition was done by varying the beam current. The temperature was judged by observing the color of the samples through a window and maintaining it at a medium red which should be about at 700–800 C.[18] One direct optical pyrometer measurement was made and agreed well with 700 °C.

The beam was scanned at 10 kHz horizontally and 100 Hz vertically by means of electrostatic deflection plates. This produced good lateral uniformity of fluence over the implanted area. The size of the surfaces implanted with nitrogen varied between 0.4 and 1.0 cm^2. Beam current collected on the target holder was integrated for fluence determinations with an accuracy of $\pm$ 5% and the samples were implanted at a 7° tilt angle to minimize effects of channeling. Prevention of contamination of the target surface during prolonged implantations was achieved with the heating of the target, a vacuum of 10^{-6} Torr, and a liquid nitrogen cold trap near the target. Normally it was impossible to determine the position of the implanted area on the sample surface by visual observation.

Infrared transmission and reflection measurements were made by means of a Beckman IR-20AX double-beam spectrometer for frequencies between 600 and 4000 wave numbers. This spectrometer was purged of water vapor and CO_2 by circulating room air through columns of activated alumina. For frequencies between 4000 and 8000 wave numbers, a Beckman IR-4 double-beam spectrometer was used. The quoted accuracy of these instruments is $\pm$ 1% in absolute transmission, and the reproducibility is $\pm$ 0.2%.

For reflection measurements a specular reflection attachment was employed which had a fixed angle of incidence to the sample normal of 20°. A front surface Al mirror provided the 100% reflection standard. To obtain the absolute reflection R from the sample, the reflection from the mirror was taken to be that of an aged high-vacuum evaporated Al film.[19]

IV. THEORETICAL MODEL AND DATA ANALYSIS

As discussed in the introduction, the substrate implant temperature of 700 °C is well above the temperature for rapid regrowth of disordered silicon, which is about 600 °C. Therefore, we expect that there will be a crystalline cover layer extending from the surface down to the buried nitrogen layer. This was confirmed by a glancing-angle electron-diffraction measurement on one implanted sample which revealed a ⟨111⟩ oriented single-crystal surface.

Also from results previously mentioned, we know that silicon nitride absorption bands are created in the buried layer. Since the index of refraction of Si_3N_4 is less than Si, we may expect to find the effective refractive index of the buried layer less than Si. Therefore, the i-r reflection and transmission spectra were computed assuming a model similar to the 3-layer model of Kachare (layer 1 was crystalline silicon, layer 2 was silicon nitride, and layer 3 was crystalline silicon). This model proved to be inadequate because no physically reasonable set of parameters could be found which reproduced the data in Fig. 1.

Since the implanted N profile is predicted to be Gaussian in shape, it might be assumed that the refractive-index profile is likewise a Gaussian. Direct analytical calculation of results to be expected from such a Gaussian distribution did not appear practical, and therefore an approximate method was necessary. Accordingly, a computer code was written to allow the calculation of interference at normal incidence in reflection (R) and transmission (T) from multilayer thin films using the expressions of Heavens.[20] This code calculates R and I from an arbitrary number of layers, the only inputs being the indices of refraction n_j, extinction coefficients k_j, and layer thicknesses Z_j for a total of l layers.

The calculations are performed for the wave-number region greater than 2000 cm^{-1} where it can be assumed that

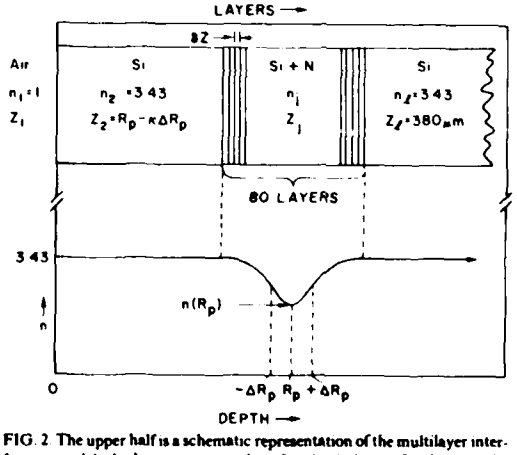

FIG. 2. The upper half is a schematic representation of the multilayer interference model which approximates the refractive-index profile shown in the lower half of the figure.

all $k_j = 0$. The variation with wave number of the index of refraction of the substrate n_s was included in the model by fitting the data of Salzberg and Villa[21] to a Cauchy equation with the result

$$n_s = \left[4.1476 + \frac{5.8876 \times 10^9}{(27\,973)^2 - L^2} \right]^{1/2}. \tag{2}$$

This reproduces the experimental silicon refractive index as a function of frequency to better than three decimal places. Figure 2 indicates some details of the input information of the calculations. As shown in the lower portion the index of refraction is characterized by the three parameters: R_p, the distance to the peak of the Gaussian; ΔR_p, the standard deviation of the Gaussian; and $n(R_p)$, the refractive index at the Gaussian peak. As a practical matter for the calculation, the Gaussian is truncated in the wings at κ standard deviations. This refractive-index profile is approximated by dividing the implanted region into many uniform layers of equal thickness $Z_j = \delta z$, but with different indices of refraction as determined by the Gaussian distribution. Thus, the quantities n_j in the implanted region are taken as

$$n_j = n_s - [n_s - n(R_p)] \times \exp\left[-\tfrac{1}{2} \left(\frac{-\kappa \Delta R_p + \delta z(j-1)}{\Delta R_p} \right)^2 \right]. \tag{3}$$

Convergence tests have shown that R and T are calculated to better than 0.1% accuracy if $\kappa = 4$ and $\delta z < \Delta R_p/10$. Thus, about 80 layers are required to approximate the Gaussian.

This model was used as the fitting function to a nonlinear least-squares fitting code to determine the parameters R_p, ΔR_p, and $n(R_p)$. The results of a fit are illustrated in Fig. 3. (This sample had the back surface lapped to eliminate rear surface reflections and had been annealed at 1000 °C for 1 h in a partial pressure of oxygen followed by an HF wash.)

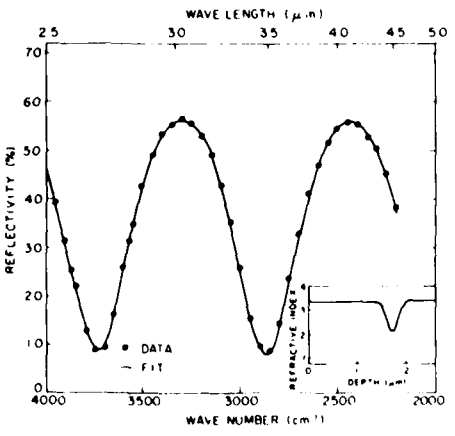

FIG. 3. Reflectivity of silicon implanted with 1.5-MeV nitrogen ions to a fluence of 1.25×10^{15} ions/cm^2. The substrate temperature during implantation was 700 °C and was annealed after implantation at 1000 °C for 1 h in a partial pressure of oxygen. The oxide was removed by an HF acid wash and the rear surface was lapped to eliminate rear surface reflections. The smooth curve is the result of fitting the data to the model described in the text. The fitting function was the refractive index profile shown in the insert.

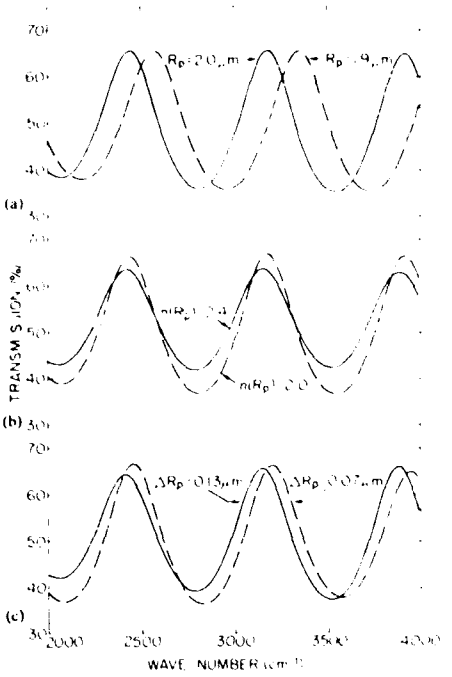

FIG. 4. Variations in interference-fringe amplitudes and phases caused by deviations in the parameters away from the parameter set [$R_p = 2.0\,\mu$m, $n(R_p) = 2.0$, and $\Delta R_p = 0.1\,\mu$m]. (a) $R_p = \pm 0.1\,\mu$m. (b) $n(R_p) = \pm 0.4$. (c) $\Delta R_p = \pm 0.03\,\mu$m.

The quality of the fit shown in Fig. 3 is very good and the insert shows the refractive-index profile computed from the best fit parameters. (This is sample 8b in Table I). For computer fits to reflectivity data, the fitted R_p value must be corrected for the small optical-path difference between the computed 0° and the actual 20° angle of incidence θ, to the surface normal imposed by the reflection attachment on the i-r spectrometer. For small angles this correction takes the form

$$R_{preal} \cong \frac{n_s R_{phot}}{(n_s^2 - \sin^2\theta)^{1/2}}, \tag{4}$$

and its value appears in parentheses below R_p in Table I.

To calculate i-r reflection or transmission for samples polished on both sides, the method of Berning was employed which sums the rear surface reflections incoherently with those of the front surface layers to eliminate interference with the rear surface reflections.[22] The interference fringes caused by front surface-rear surface reflections do not appear in our experimental spectra because the frequency resolution of the spectrometer was adjusted to be greater than the fringe spacing.

It is instructive to ask what features of the data each of the three fitting parameters are sensitive to. Figure 4 shows the computer generated i-r transmission spectra for variations around the parameter values $R_p = 2.0\,\mu$m, $\Delta R_p = 0.1\,\mu$m, and $n(R_p) = 2.0$. In Fig. 4(a) the change

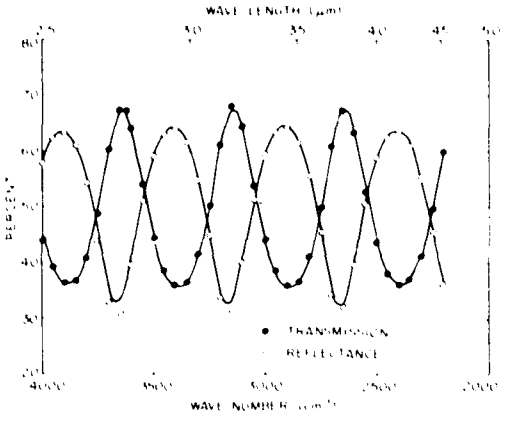

FIG. 5. Infrared transmission and reflectance of silicon implanted with 3.17-MeV nitrogen ions to a fluence of 1.55×10^{17} ions/cm^2. The substrate temperature during implantation was 700 °C. The solid curves are calculated fits using a model which assumes a Gaussian shape for the refractive index changes in the implanted layer.

induced by reducing R_p by 0.1 μm is shown. It is apparent that the phase of the fringe pattern is very sensitive to R_p, and the fringe spacing is also changed. This is useful information in that it provides an estimate of the sensitivity of this method to the parameters involved. For example, we calculate that a change in R_p of + 10 nm increases chi square by a factor of 2 and produces a phase shift with respect to the data. A conservative estimate of the precision of this parameter is + 15 nm. Similarly, Fig. 4(b) shows the generated i-r spectra for an increase in $n(R_p)$ of 0.4 and in Fig. 4(c) the spectra for changes of + 30 nm in ΔR_p. We estimate the precision of these parameters to be + 0.06 and + 10 nm, respectively. In any fitting procedure it is desirable to have nominally independent features in the data controlled by different parameters. This model approaches this state of affairs in that in Fig. 4 it is seen that the fringe spacing and phase are chiefly controlled by R_p, the fringe amplitude by $n(R_p)$, and the modulation of the fringe amplitude by ΔR_p.

One test of the model is to fit reflection and transmission data from the same sample, and require that R and T at all frequencies sum to 1.0, and require that the nonlinear least-squares fits yield the same values of the parameters R_p, ΔR_p, and $n(R_p)$. Figure 5 presents the results of such a test for a sample (10a,b, Table I) implanted to a fluence of 1.55×10^{17}/cm^2 at an energy of 3.17 MeV. The values in Table I for the fitted parameters show excellent agreement in ΔR_p, $n(R_p)$, and R_p after correcting for the 20° angle of incidence by means of Eq. (4). Note in Fig. 5 the phase shift between R and T that arises from the 20° angle of incidence of the reflection attachment.

As a further check on the optical-range measurement method, a sample was subjected to Rutherford backscattering (RBS) analysis using 2.9-MeV α particles scattered at an angle of 165°. Figure 6 shows the backscattered energy spectrum obtained from this sample which was implanted at 1.4 MeV to a fluence of 6×10^{16} ions/cm^2 (sample 6, Table I). The detected particles have been scattered from the silicon. The presence of implanted nitrogen is revealed by a decreased signal, and an inverted nitrogen profile is directly evident in the data. Sufficient nitrogen has been introduced so that measurements extracted from these data must be corrected for the added energy losses in the backscattered beam due to the nitrogen. The corrected value gives R_p = 1.72 μm and ΔR_p = 0.10 μm, in good agreement with the i-r method. Similar RBS spectra on samples annealed at 1000 °C for 1 h in vacuum indicate that no redistribution of nitrogen occurs. This agrees with the i-r data for sample 8 which show that, within errors, ΔR_p and $n(R_p)$ do not change upon annealing.

V. RESULTS AND DISCUSSION

In Fig. 7 we present the i-r transmission data for six samples implanted with nitrogen ions at 700 °C to different fluences and energies. The points represent data and the smooth curves are the result of fitting the data to the model described in Sec. IV. The least-squares adjusted curves are in excellent agreement with the data. Note that the spacing of the fringe maxima and minima decreases as the implanted-ion energy increases, as one would expect as the depth of the reflecting layer increases. Also, the peak-to-valley amplitude of the fringes grow in a regular fashion as the ion fluence increases, indicating that the refractive index of the buried layer is reduced more and more below that of silicon.

Table I summarizes the results of all the computer fits including the fits to the i-r spectra in Figs. 3,5, and 7. For two of the samples, the normalization of the data was unavailable and an additional normalization parameter F had to be included in the fits. The parameter was a constant multiplying the calculated R and its value is indicated in Table I. For the sample implanted at 0.83 MeV, ΔR_p and $n(R_p)$ were fixed, and only R_p was varied since a portion of the surface had spalled off. The model would not be expected to apply in this case, except as regards R_p. Experimentally, we observe that spallation will occur when the local atomic concentration of nitrogen exceeds about 60 at. %, which corresponds to about the concentration of nitrogen in crystalline Si_3N_4.

Returning to Table I, note that R_p decreases as the fluence increases for the implant energies 0.67, 1.4, and 3.17 MeV. This trend, appearing as it does in all cases where

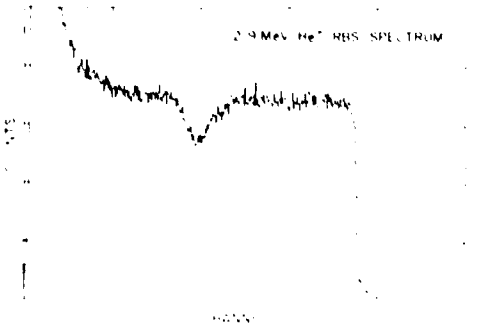

FIG. 6. Energy spectrum of He ions backscattered at a 165° angle from nitrogen-implanted silicon (1.4 MeV, 6×10^{16} cm^{-2}).

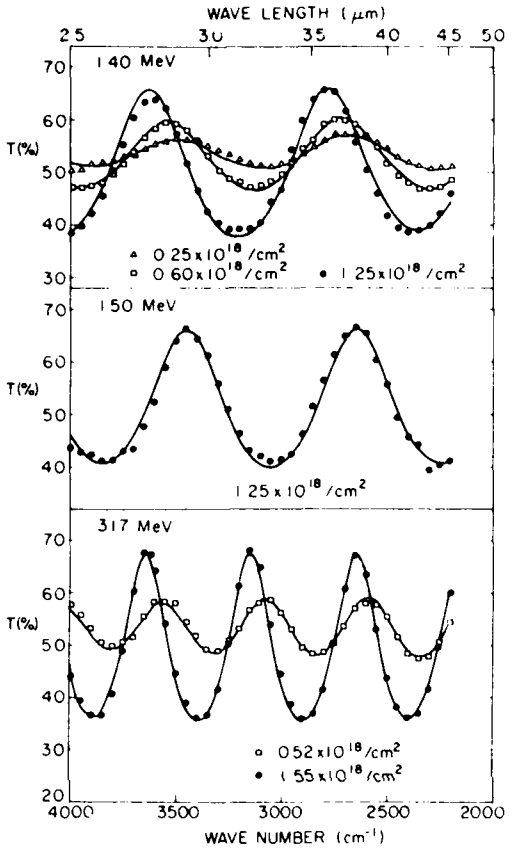

FIG. 7. Infrared transmission spectra of nitrogen implanted silicon. The smooth curves are the result of fitting the data to a model described in the text.

fluence dependent data were taken, is suggestive of the removal of surface atoms by sputtering. The fluence dependence of implanted depth is the net result of three processes; (i), the removal of surface atoms by sputtering, (ii), the lattice expansion caused by the addition of the implanted nitrogen, and (iii) progressively reduced penetration of the nitrogen due to the formation of the silicon nitride which has a somewhat higher stopping power than silicon. Calculations using a simplified model indicate that the third process (which reduces measured depth) is a smaller effect than the second process (which increases it). Thus, if the differences due to the fluence are taken at face value, sputtering is the predominant effect.

The area of each Gaussian determined from the parameters ΔR_p and $n(R_p)$ in Table I is plotted in Fig. 8 versus fluence. The area is proportional to the change in optical path through the buried layer from that of crystalline silicon. Different energy implants are noted by different symbols. The data points are well represented by a straight line indicating that the magnitude of the change in optical-path length is directly proportional to the nitrogen fluence. It is

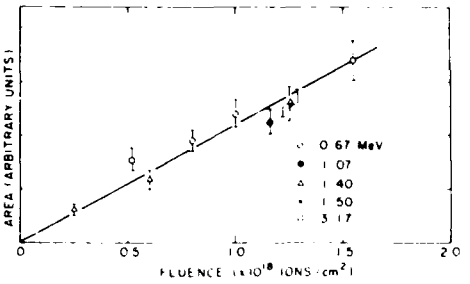

FIG. 8. Area under Gaussian refractive-index profile [area $\propto n(R_p) \times \Delta R_p$] as a function of fluence for several different nitrogen implantation energies. The area is proportional to the change in optical path through the buried layer from that of crystalline silicon.

also interesting to note that the peak refractive indexes for the highest fluences (samples 7,8, and 10) correspond closely to the refractive index of crystalline Si_3N_4 which is 2.0.[24]

The data in Table I provide precision measurements of R_p and ΔR_p, the first and second moments of the range distribution of implanted nitrogen in silicon. Figures 9 and 10 show a comparison of these data with the tabulations of Johnson and Gibbons (JG),[25] Northcliff and Schilling (NS),[26] and Gibbons, Johnson, and Mylroie (GJM).[27] The experimental range values in Fig. 9 fall well below all the table values. This is to be expected in the light of Z_1 (projectile) oscillations in the electronic stopping power.[28] The electronic stopping power for nitrogen in silicon is near a maximum in the Z_1 oscillations, thus reducing the nitrogen

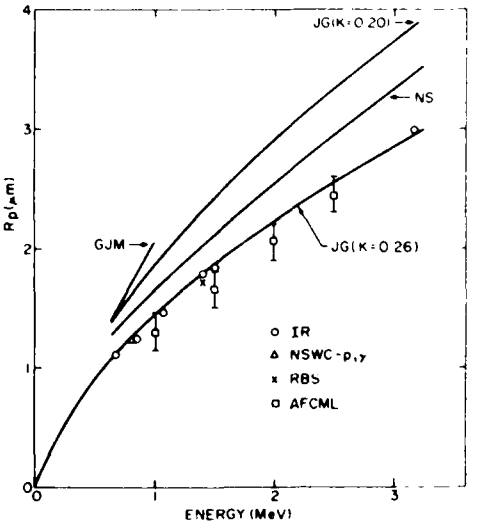

FIG. 9. Experimental projected range measurements for nitrogen ion implanted into silicon as a function of energy compared to tabulated range values from Gibbons, Johnson, and Mylroie (GJM), Johnson and Gibbons, [JG ($K = 0.2$)], Northcliff and Schilling (NS), and adjusted Johnson and Gibbons, [JG ($K = 0.26$)]. The I-r and RBS points are from this work, the (p,γ) point is from the data of I. and *et al.*, and the AFCRL points are from the data Rossild *et al.*

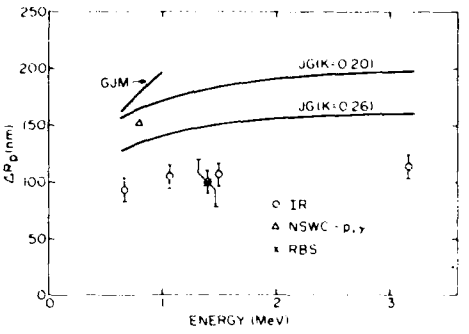

FIG. 10. Experimental range straggling measurements for nitrogen ions implanted into silicon as a function of energy compared to the tabulated straggling values from Gibbons, Johnson, Mylroie (GJM), Johnson and Gibbons [JG ($K = 0.2$)], and adjusted Johnson and Gibbons [JG ($K = 0.26$)]. The i-r and RBS points are from this work and the (p,γ) point is from Land *et al.*

range. The large discrepancy between the range tables and experimental ranges for low Z ions in silicon has been noted by others.[28] Also included in Fig. 9 are range measurements by Roosild *et al.* (AFCRL) utilizing a staining technique,[30] a range measurement performed by Land *et al.* (NSWC) by means of the (p,γ) resonance profiling technique,[31] and the RBS measurement mentioned previously. The latter two values agree well with the i-r range measurements and the other four values agree within the specified measurement errors.

The curve labeled JG ($K = 0.20$) is the predicted projected range from the JG tables which uses the LSS estimate of the electronic stopping parameter K in the expression

$$d\epsilon/d\rho = K\epsilon^{1/2} \tag{5}$$

where ϵ and ρ are the LSS reduced energy and range variables, respectively.[32] The K was arbitrarily adjusted by making a one parameter fit of LSS theory to the i-r projected range data.[33] The curve labelled JG ($K = 0.26$) is the calculated projected range for this adjusted K value and agrees well with the i-r data.

Figure 10 presents the i-r measurements of ΔR_p along with the tabulated values from GJM and JG. The LSS theory, with the electronic stopping parameter adjusted (JG,$K = 0.26$), is 40% higher than the i-r data indicate. This difference implies that the atomic collision cross section for the nitrogen in silicon system has been overestimated by the Thomas-Fermi atomic model used in LSS theory to compute the slowing down contribution from nuclear stopping. This is consistent with measurements by Grob *et al.* which show that LSS theory overestimates the nuclear stopping contribution for nitrogen in silicon by as much as 50% for nitrogen energies below 1 MeV.[34] The point labelled NSWC (p,γ) is from Land *et al.*[31] The RBS data point (corrected for straggling of the α particle beam) is in agreement with the i-r data.

The large changes observed in the implanted layer refractive index appear to be associated with changes in density and polarizability. A simple model to predict the parameter $n(R_p)$ may be constructed by assuming the buried layer is a mixture of $Si_3(Si_3N_4)$. Then the Lorentz-Lorentz equation,[35]

$$\frac{n^2 - 1}{n^2 + 2}\frac{M}{\rho} = \frac{4\pi}{3}\frac{A\alpha}{\epsilon_0}, \tag{6}$$

may be used to compute $n(R_p)$, where ρ is the density, M is the effective molecular weight, α is the polarizability of the mixture, A is Avogadro's number, and ϵ_0 is the dielectric constant of space. For the density at R_p we assume a linear increase between $\rho = 2.3$ g/cm^3 for Si to $\rho = 3.1$ g/cm^3 for Si_3N_4 for nitrogen concentrations between 0 and 60%, respectively. The nitrogen concentration at R_p is computed from the measured ΔR_p and fluence, or from RBS measurements, where applicable. The polarizabilities are taken as 1.3×10^{-24} cm^3 per atom for Si_3N_4 and 3.7×10^{-24} cm^3 for Si. The polarizability of the mixture is taken as the sum of these two polarizabilities weighted by the value x and y. The results of these calculations are presented in Table I. There is good agrement with experiment throughout the range of energies and fluences investigated.

In Sec. IV, features in the interference fringes were discussed in terms of independence of the fitting parameters R_p, ΔR_p, and $n(R_p)$. These three parameters characterize the data well in the wavelength region between 2.5 and 5.0 μm (4000–2000 cm^{-1}). In this region the wavelength of the light within silicon ranges between about 0.7–1.5 μm. These wavelengths are somewhat greater than the dimensions of the buried nitrogen layer (e.g., $\approx 2 \times \Delta R_p = 0.2\,\mu$m) so that the interference effects are sensitive chiefly to the maximum index change and the optical path through the layer rather than to the detailed profile of the buried layer. This must be the case since for the data in Figs. 3,5, and 7 there is little room for improvement in the quality of the fits and additional model parameters would not be meaningful. (Some sensitivity to the refractive-index gradient in the implanted region is maintained at these wavelengths since the simple 3-layer model discussed in Sec. II did not reproduce the data.) Thus, in an empirical sense, the interference fringes in this frequency region are primarily sensitive to the first and second moments of the nitrogen range distribution. However, at smaller wavelengths, it may be anticipated that the fringes will become more sensitive to details in the shape of the concentration profile, and thus additional parameters may be needed.[8]

To test this possibility an i-r transmission spectrum was measured for sample 1 in the wavelength region 1.25–4 μm and is shown as the data points in Fig. 11. Now the wavelength of light inside silicon varies between 0.36 and 1.2 μm and at the smaller value is approaching the dimensions of the width of the buried layer. The dashed line is a three-parameter fit (1b, Table I) performed in identical fashion with the previous fits but for data between the frequencies 2000–8000 cm^{-1}. The solid line is the result of adding one parameter to the model wherein the Gaussian refractive-index profile is allowed to have different standard deviations on either side of the centroid (1c, Table I). This fit results in a large improvement over the three-parameter fit. The nitrogen concentration profile obtained from the parameters of this fit is

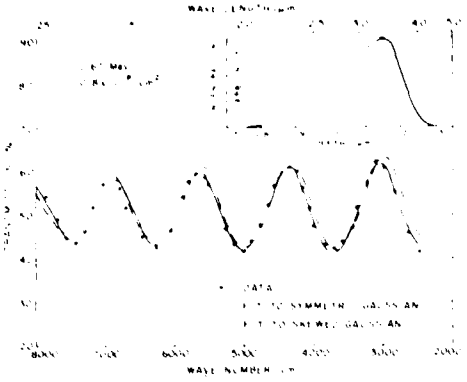

FIG. 11. Transmission of nitrogen implanted silicon between 1.25 and 5.0 μm in the infrared. The closed circles are data and the dashed curve is a calculated fit to a symmetric Gaussian refractive-index profile. The solid line is a fit to a Gaussian refractive-index profile with different standard deviations on either side of the centroid. Shown in the insert is the nitrogen concentration profile obtained from the skewed Gaussian fit.

shown in the insert of Fig. 11. Note the pronounced asymmetry of the profile toward the surface. Examining the RBS spectrum in Fig. 6 one can detect the asymmetry in this profile as well which supports the i-r data result. As a self-consistency check on the data analysis we observe that the effective optical path of the asymmetric profile (fit 1c) is equal within errors to the optical path of the symmetric profile (fit 1a). To illustrate this we note that the integrated areas under each profile are equal to within 8%, and the median of the symmetric profile of 1.106 μm agrees well with the median of the asymetric profile of 1.103 μm. The value of R_p in Table I for sample 1c is the depth of maximum concentration where the two half-Gaussians are joined and therefore is not the first moment of the range distribution.

The detection limit of the i-r technique is estimated to be about 0.7×10^{17} N/cm^3 (~ 6 at.% nitrogen peak concentration) for samples with the rear surface abraded. This limit corresponds to a 2% peak-to-valley interference-fringe amplitude and a change in the refractive index of $\pm$ 0.06. The minimum detectable change in the refractive index is relatively independent of the refractive index of the substrate. The minimum depth which can be profiled in Si is approximately 0.15 μm which is equivalent to 1/2 fringe appearing between 2000 and 8000 wave numbers. The i-r refractive-index profiling method should be applicable to other infrared transmitting materials as well, provided the impurity gives rise to an absolute refractive-index change greater than 0.06.

VI. SUMMARY

Interference fringes observed in infrared transmission and reflectance spectra of nitrogen implanted silicon samples for the frequencies between 2000 and 8000 cm^{-1} are caused by substantial refractive-index changes in the buried implanted layer. Refractive-index profiles of the implanted surfaces can be determined by computer fitting the interference spectra to an approximate model based on multilayer thin-film interference equations.

The shape of refractive-index profiles obtained in this manner are identical to the shape of the implanted nitrogen profiles within the errors of the measurements.

Computer fits of a thin-film interference model to experimental infrared spectra in the frequency range of 2000–4000 cm^{-1} yield precise measurements of the projected range (~ 1% error) and straggling (10% error) of the implanted nitrogen ions, and the method is nondestructive. Analysis of the infrared spectra over an expanded frequency range (2000–8000 cm^{-1}) yields a measurement of the asymmetry of the range distribution as well.

Measured projected ranges and straggling of the implanted nitrogen ions in silicon between the energies of 0.07 and 3.17 MeV are substantially smaller than predictions of LSS theory. Atomic shell effects account for most of this discrepancy, but a modification of the atomic collision cross section is in order to bring theory and experiment into good agreement.

The magnitude of the refractive-index change is consistent with a model that assumes the formation of silicon nitride in the implanted layer in an amount directly proportional to the local nitrogen concentration.

ACKNOWLEDGMENTS

The authors gratefully acknowledge N. D. Wilsey for his help with infrared techniques and spirited discussion, J. A. Sprague for electron-diffraction results, and C. N. Philippi for his continued interest and support. Discussions with R. Holm, W. G. Spitzer, and C. N. Waddell were extremely useful and are hereby acknowledged. We also thank C. A. Carosella and M. Rosen for useful comments on the manuscript. This work is supported by the Air Force Materials Laboratory and the Naval Material Command.

I. I. Edelman, O. N. Kuznetsov, I. V. Tezheiko, and E. V. Tubopytova, Radiat. Eff. **29**, 13 (1976).
J. A. Borders and W. Beezhold, *Ion Implantation in Semiconductors*, edited by I. Ruge and J. Graul (Springer Verlag, New York, 1971), p. 241.
I. A. Kruze, D. I. Tetel'baum, I. I. Zorin, E. V. Shitova, and P. V. Pavlov, Izv. Akad. Nauk. SSSR, Neorg. Mater. **11**, 1381 (1975).
N. A. Genkina, P. V. Pavlov, E. V. Shitova, I. A. Kruse, and I. I. Zorin, Izv. Akad. Nauk. SSSR, Neorg. Mater. **11**, 1988 (1975).
G. H. Schwuttke, Air Force Cambridge Research Laboratories Report AFCRL-70-0459, Bedford, Mass., 1970, (unpublished).
T. E. Seidel, G. A. Pasteur, and J. C. C. Tsai, Appl. Phys. Lett. **29**, 648 (1976).
B. L. Crowder and R. S. Title, *Ion Implantation*, edited by F. Eisen and L. Chadderton (Gordon & Breach, New York, 1971), p. 87.
G. K. Hubler, C. N. Waddell, W. G. Spitzer, J. E. Fredrickson, S. Prussin, and R. G. Wilson, J. Appl. Phys. **50**, 3294 (1979).
G. K. Hubler, P. R. Malmberg, C. A. Carosella, J. P. Smith, III, W. G. Spitzer, C. N. Waddell, and C. N. Philippi, *Proceedings of International Conference on Ion Beam Modification of Materials*, Budapest, Hungary (1978) (to be published), and G. K. Hubler and P. R. Malmberg, Bull. Am. Phys. Soc. **22**, 1242 (1977).
B. L. Crowder, R. S. Title, M. H. Brodsky, and G. D. Pettit, Appl. Phys. Lett. **16**, 205 (1970).
A. H. Kachare, W. G. Spitzer, and J. E. Fredrickson, J. Appl. Phys. **47**, 4209 (1976).
A. H. Kachare, W. G. Spitzer, J. E. Fredrickson, and J. K. Tuller, J. Appl. Phys. **47**, 5274 (1976).

[1]H.B. Dietrich, J. Comas, and P.R. Malmberg, Reports of NRL Progress, (August 1974), p. 17 (unpublished).
[2]W.G. Spitzer, C.N. Waddell, G.H. Narayanan, J.E. Fredrickson, and S. Prussin, Appl. Phys. Lett. **30**, 623 (1977).
[3]W. Primak, Phys. Rev. B **14**, 4679 (1976).
[4]V.M. Gusev, L.N. Strelatsov, and I.B. Khaibullin, Sov. Phys. Semicond. **5**, 737 (1971).
[5]H.J. Stein, *Ion Implantation in Semiconductors*, edited by I. Ruge and J. Graul (Springer-Verlag, New York, 1971), p. 2.
[6]*Handbook of Chemistry and Physics*, 22nd ed., edited by C.D. Hodgman (Chemical Rubber Publishing Company, Cleveland, 1937), p. 1308.
[7]H.E. Bennett, M. Silver, and E.J. Ashley, J. Opt. Soc. Am. **53**, 1089 (1963).
[8]O.S. Heavens, *Optical Properties of Thin Solid Films* (Academic, New York, 1955).
[9]C.D. Salzberg and J.J. Villa, J. Opt. Soc. Am. **47**, 244 (2957).
[10]P.H. Berning, *Physics of Thin Films* edited by G. Haas and R. Thun (Academic, New York, 1964), Vol. 2, p. 69.
[11]H.R. Phillipp, J. Electrochem. Soc. **120**, 295 (1973).
[12]M. Neuberger, *Handbook of Electronic Materials* (Plenum, New York, 1971), Vol. 5.
[13]W.S. Johnson and J.F. Gibbons, *Projected Range Statistics in Semiconductors*, Standford University, Stanford, California, 1970 (unpublished).
[14]L.C. Northcliffe and R.F. Schilling, Nucl. Data Tables, **A7**, 233 (1970).
[15]J.F. Gibbons, W.S. Johnson, and S.W. Mylroie, *Projected Range Statistics in Semiconductors and Related Materials*, 2nd ed. (Dowden, Hutchinson, and Ross, Inc., Stroudsburg, Penn., 1975).
[16]P. Hvelplund and B. Fastrup, Phys. Rev. **165**, 408 (1968).
[17]H.B. Dietrich and L.E. Plew, Appl. Phys. Lett. **29**, 406 (1976).
[18]S. Roosild, R. Dolan, and B. Buchanan, J. Electrochem. Soc. **115**, 307 (1968).
[19]D.J. Land and J.G. Brennan, Nucl. Inst. Methods **132**, 89 (1976).
[20]J. Lindhard, M. Scharff, and H.E. Schiott, Mat. Fys. Medd. Dan. Vid. Selsk. **33**, No. 14 (1963).
[21]This fit was kindly provided by David Land of the Naval Surface Weapons Center, Wash., D.C.
[22]A. Grob, J.J. Grob, and P. Siffert, Nucl. Inst. Methods **132**, 273 (1976).
[23]A.K. Sinha and E. Lugujjo, Appl. Phys. Lett. **32**, 45 (1978).

Section IV.B

HIGH-FLUENCE IMPLANTATIONS OF SILICON: LAYER THICKNESS AND REFRACTIVE INDICES

G. K. Hubler,[1] C. N. Waddell,[2] W. G. Spitzer,[2] J. E. Fredickson,[3]

S. Prussin,[4] and R. G. Wilson[5]

[1]Materials Modification and Analysis Branch
Naval Research Laboratory

[2]Physics and Materials Science Departments
University of Southern California
Los Angeles, California

[3]Physics-Astronomy Department
California State University
Long Beach, California

[4]TRW Semiconductors
Lawndale, California

[5]Hughes Research Laboratories
Malibu, California

This research was supported in part by the Naval Material Command,
the Air Force Material Laboratory (NRL), and by the
Air Force Office of Scientific Research, Air Force Systems Command (USC)

High-fluence implantations of silicon: Layer thickness and refractive indices

G. K. Hubler

Naval Research Laboratory, Washington, D.C. 20375

C. N. Waddell and W. G. Spitzer

Physics and Materials Science Departments, University of Southern California, Los Angeles, California 90007

J. E. Fredrickson

Physics-Astronomy Department, California State University, Long Beach, California 90840

S. Prussin

TRW Semiconductors, Lawndale, California 90260

R. G. Wilson

Hughes Research Laboratories, Malibu, California 90265

(Received 12 October 1978; accepted for publication 20 December 1978)

Refractive-index measurements are given for amorphous Si produced by ion implantation. Reflection interference measurements in the frequency range $250 \lesssim \nu \lesssim 7600$ cm^{-1} were made for several Si samples implanted with P-ion fluences between 1.0×10^{16} and 10×10^{16} ions/cm^2 and ion energies between 0.20 and 2.7 MeV and for Si implants of 1.0×10^{16} and 3.0×10^{16} ions/cm^2 and an ion energy of 0.30 MeV. The interference measurements were computer analyzed by using a model in which the damaged layer has a refractive index n_D and extinction coefficient k_D, and the substrate has a refractive index n_s and $k_s = 0$. The optical constants of the two regions are smoothly connected by a transition region approximated by a half-Gaussian curve of standard deviation σ_D. The finite-width transition region is necessary for fitting the data. Excellent fits are obtained for literature values of n_s and k_D with the chi-square being $\simeq 10^{-4}$. The value of k_D has little effect on the analysis. Within the experimental accuracy a single curve for $n_D(\nu)$ is obtained for the amorphous region where $n_D(\nu)$ is independent of the ion type, ion energy, ion fluence, or position in the amorphous layer. The thicknesses of the damaged layers deduced from the infrared data agree well with LSS values for $R_p + \sigma_p$ and with channeling results. Visual observations of the thicknesses also agree well for the high-energy implants but not for the lower-energy ones.

PACS numbers: 61.80.Jh, 78.20.Dj, 61.70.Tm, 78.65.Jd

I. INTRODUCTION

When silicon is implanted with a sufficiently large fluence of ions, the implanted region becomes highly disordered and has been characterized as amorphous.[1,2] A variety of techniques have been used to study the disorder and its effect on the physical properties of both implanted material and grown amorphous layers. These techniques include x-ray diffraction and electron microscopy,[1,3] optical absorption,[4,5] ion channeling,[1,6] Coates-Kikuchi lines,[1] physical appearance (color),[1,4] electron paramagnetic resonance,[7] and infrared refractive indices.[8-10] The present study consists primarily of the determination of changes in the refractive index of Si produced by high-fluence implantations, and it is, in large part, an extension of some earlier investigations of the effects of ion implantation on the optical properties of GaAs[11-13] and GaP.[12,14]

A series of Si samples were implanted with either Si^+ or P^+ ions to fluences ranging from 10^{15} to 10^{17} ions/cm^2. Phosphorus ions were implanted at energies of 200 keV, 300 keV, and 2.7 MeV; silicon ions were implanted at an energy of 300 keV. The reflection of infrared radiation from the implanted surface was measured for the frequency range 250–7600 cm^{-1}. The reflection spectrum consists of an interference fringe pattern produced by the interference of light multiply reflected between the front surface and the interface between the disordered and crystalline materials. The refractive index of the disordered material was determined from least-squares computer fitting of the interference spectra. The fitting program utilized the multilayer thin-film expressions of Heavens,[15] and it was found necessary to include a smooth matching of the refractive index of the disordered layer to that of crystalline substrate. The measured absorption of

 0021-8979/79/053294-10$01.10

TABLE I. Summary of implant conditions and "best-fit" parameters.

Si Sample	Ion	Energy (keV)	Fluence (10^{14} cm^{-2})	Temp (°K)	R_D (μm)	σ_D (μm)	χ^2 ($\times 10^{-4}$)	k_D	$n_D(\nu)$ 500 cm^{-1}	4000 cm^{-1}	7500 cm^{-1}
78-6 [a]	P^+	2700	1.74	200	2.52	0.041	0.83	k_M	3.82	3.87	4.00
					2.52	0.053	1.05	0	3.82	3.87	4.00
78-7	P^+	2700	1.74	200	2.54	0.035	1.69	k_M	3.80	3.84	3.96
					2.54	0.047	1.95	0	3.81	3.85	3.97
75-1 [a]	P^+	2700	6.4	~300	...	...	...	...	...	...	...
75-2	P^+	2700	6.4	~300	2.54	0.036	2.43	0	3.73	3.76	3.86
75-3 [a]	P^+	2700	6.4	~300	...	...	...	...	...	...	...
78-8	P^+	2700	10.0	200	2.61	0.032	2.28	k_M	3.77	3.82	3.95
					2.61	0.046	1.68	0	3.77	3.82	3.95
76-3	P^+	300	1.0	~300	0.507	0.037	0.69	0	3.79	3.84	3.98
76-4	P^+	300	1.0	~300	0.506	0.035	0.61	0	3.78	3.83	3.98
77-1	P^+	300	3.0	~300	0.551	0.044	0.93	0	3.81	3.86	4.03
77-2	P^+	300	3.0	~300	0.549	0.045	0.74	0	3.81	3.86	4.02
					0.143	<0.01 [b]			3.53	3.56	3.62
76-1 [a]	Si^+	300	1.0	~300	0.531	0.052	0.82	0	3.81	3.86	4.02
76-2	Si^+	300	1.0	~300	0.569	0.040	1.05	0	3.80	3.84	3.98
77-3	Si^+	300	3.0	~300	0.611	0.038	0.81	k_M	3.80	3.84	3.96
					0.612	0.041	0.75	0	3.80	3.84	3.96
77-4	Si^+	300	3.0	~300	0.624	0.030	0.57	0	3.76	3.80	3.91
77-5	P^+	200	1.0	~300	0.407	<0.01 [b]	1.54	k_M	3.75	3.78	3.86
					0.408	<0.01	1.41	0	3.75	3.78	3.86
77-6	P^+	200	1.0	~300	0.407	<0.01 [b]	1.03	0	3.76	3.79	3.86
76-5	None	...	...	...	...	...	...	...	3.42	3.44	3.50

[a] Double-layered sample

[b] See text for discussion

amorphous sputtered silicon was also included where significant. Thus, the results of the fitting process include the thickness of the disorder region and the width of the transition region as well as the frequency-dependent index of refraction of the disordered material.

The refractive index of the disordered layer is shown to be insensitive to the implantation parameters for the fluence range investigated. In a number of cases the layer thicknesses are compared to those obtained from channeling measurements, changes in physical appearance, and projected range calculations.

II. EXPERIMENTAL PROCEDURES

A series of samples were cut from four (111)-oriented wafers of high-resistivity ($\rho > 10^3\ \Omega$ cm) single-crystal silicon. The wafers were adjacent slices from the same ingot. The samples used in this study were implanted at three different laboratories so that implant conditions were not exactly the same for all samples. In each case, however, the samples were implanted at an angle of approximately 8° from the surface normal to minimize range straggling due to ion channeling.

The low-energy (200–300 keV) Si^+ and P^+ implantations (samples 76-1–76-4 and 77-1–77-6 of Table I)[14] were done with the samples heat sunk to a room-temperature mount. The ion beam was raster scanned in both the horizontal and vertical directions to ensure lateral uniformity of the ion fluence.

The initial high-energy implants (P^+ and 2.7 MeV) utilized a defocused ion beam and heat sinking to a water-cooled mount. The interference pattern observed from two (75-1 and 75-3) of the three Si samples had structure in the fringe amplitude indicating that the implanted material was optically a double layer. This was confirmed by ion-channeling measurements of one of the samples which showed that there was a thin lightly damaged crystalline layer on the surface followed by a heavily disordered region.[15] The GaAs and GaP samples implanted under the same conditions were also found to have double layers in the implanted regions.

Subsequent attempts to produce single-layer high-energy implants in Si demonstrated that close temperature control of the samples was essential. Inadequate thermal contact or a high beam flux resulted in a crystalline cover layer and a

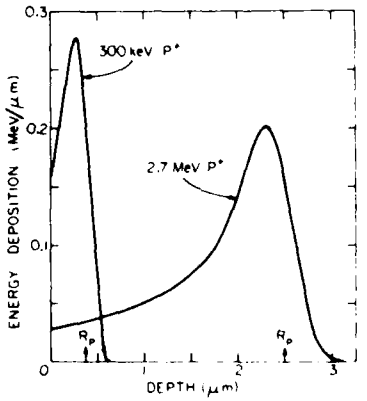

FIG. 1. Energy deposition per unit thickness resulting from nuclear displacements versus depth for P^+ ions of incident energy 300 keV and 2.7 MeV. Projected ranges for the P^+-ion distributions are indicated.

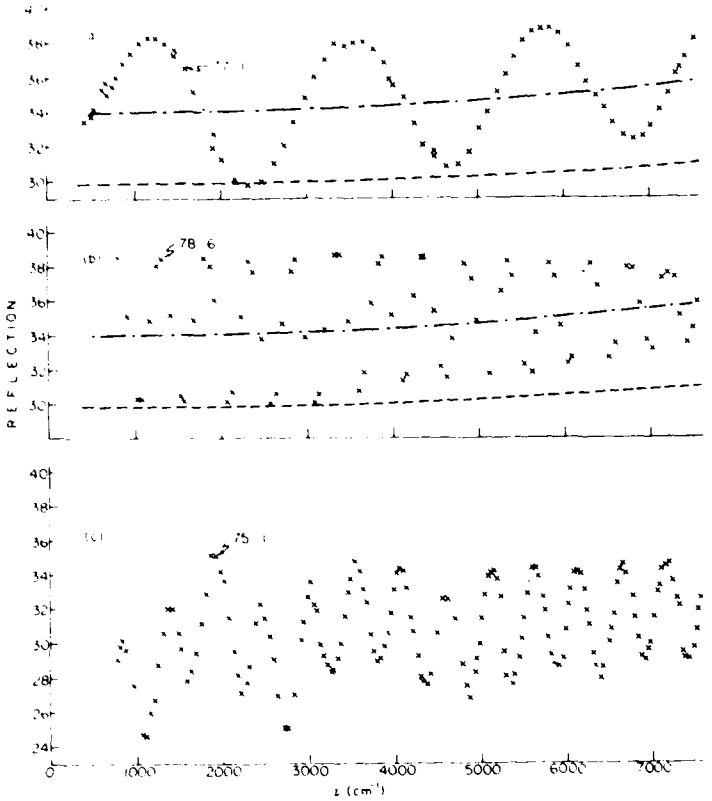

FIG. 2. Data for samples 77-1, 78-6, and 75-1 of Table I. The dashed curves are the reflectivity for a homogeneous material with $n = n_s$. The dashed-dot curves are for the reflectivity when $n = n_{ps}$ (see text for definitions).

buried disordered layer. These double-layer samples were easily identified with ir reflection measurements [see Fig. 2(c)]. The other samples used in this study (78-6–78-8) were implanted with the samples secured to a mount maintained at 200 °K by means of a thin layer of high-vacuum grease to provide thermal contact. The ion beam was raster scanned and the incident flux was limited to 0.6 μ A/cm^2.

The implant conditions from each sample are specified in Table I. In most cases the implantations were done with paired samples to provide a backup sample and to permit reproducibility comparisons. In all cases except two, which will be discussed, the results from similarly implanted samples were essentially identical.

The infrared reflection measurements were made at room temperature by using a dry-nitrogen purged single-beam spectrometer in which the energy reflected from the sample was compared to that reflected from a high-quality front-surface Al mirror. To obtain the absolute reflection R from the sample, the reflection from the mirror was taken to be that of an aged high-vacuum-evaporated Al film.[17] The reflection was measured with the beam at near normal incident to the implanted surface. The opposite surface of the sample was coarse lapped to eliminate multiple reflections between the front and rear surfaces.

The thickness of the disordered layer(s) of several samples was measured by means of the channeling-effect technique by using the facilities and methods of the group at the California Institute of Technology.[18] To obtain a measurement of the thickness of the layer having a different visual appearance, a region near one edge of the implanted surface was beveled at an angle of 20 mrad (50 : 1) by using a chemical polish to expose the implant-substrate interface. A microscope was used to determine the width of the "white" layer and the bevel angle was measured with an interferometer.

III. DISCUSSION

Before presenting the experimental results, it will be helpful to discuss some features of the results and of the model which has been developed to analyze the data.

It is well known that the displacement damage produced during ion implantation is concentrated near the end of the range of the ions. The spatial variation of damage increases as the energy of the ion is increased; this is illustrated in Fig. 1 in which we present calculations of the damage profile produced by 300-keV and 2.7-MeV P$^+$ ions in Si.[19] For the fluences utilized in this study ($\gtrsim 10^{14}$ ions/cm^2) the experiments indicate that there is a disordered region having

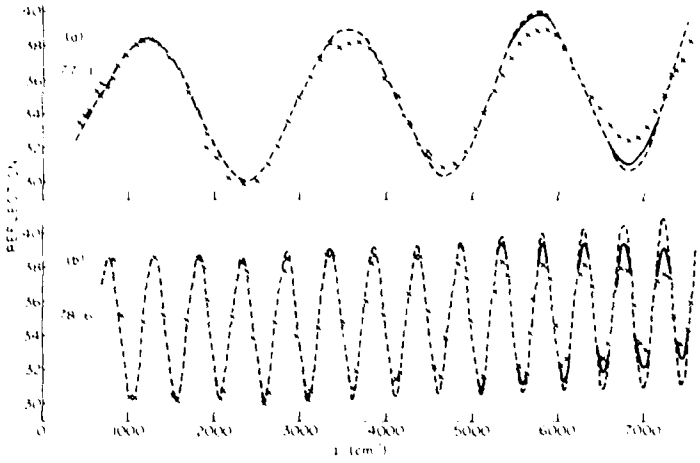

FIG. 3. Data for samples 77-1 and 78-6 of Table I. The dashed curves were calculated with the model given in the text by using $\sigma_D = k_D = 0$. The solid curve has $\sigma_D = 0$ and k_D given by Ref. 7.

uniform dielectric properties extending from the surface to a depth corresponding approximately to $R_p + \sigma_p$.[7,23] This indicates that the disorder has saturated. Previous studies indicate that the "amorphous region" starts in the region of greatest damage and propagates in both directions.[1] For the fluences studied here the saturation region has reached the surface. Confirmation of the damage saturation was provided by the particle-channeling measurements which showed that the particles backscattering from the damaged region with the incident beam aligned along the original ⟨111⟩ axis was the same as that from a randomly oriented Si crystal. The data presented in the next Sec. IV show that the depth of the heavily disordered region increases with fluence as expected.

Shown in Fig. 2 are three interference spectra—the first [Fig. 2(a)] is from 300-keV P^+ ions, the second [Fig. 2(b)] is from 2.7-MeV P^+ ions, and the third [Fig. 2(c)] is also from 2.7-MeV P^+ ions. The third illustrates the "structure" that can occur when there is an optical double layer in the disordered region. The lower dashed lines in Figs. 2(a) and 2(b) indicate the reflection that would be measured from an undamaged Si-air interface calculated from the equation

$$R = \left(\frac{n - 1}{n + 1}\right)^2, \tag{1}$$

with $n = n_c$, the index of refraction of crystalline Si.[22] The central dashed-dot lines indicate the reflection that would be obtained from Eq. (1) for a disordered Si-air interface with $n = n_D$, the value for the damaged layer. If the damaged layer is nonabsorbing, the dielectric properties of the disordered layer are uniform, the change in the index of refraction ($n_D - n_c$) is much less than n_D, and the interface between the damaged region and the crystalline substrate is sharp compared to the shortest wavelength used, then the interference spectra consist of fringes that oscillate about the reflection due to n_D with a minimum reflection equal to that from n_c. The amplitudes of the fringes in Figs. 2(a) and 2(b) are consistent with this simple model at low frequencies, but the amplitudes of the high-frequency fringes are reduced in both cases.

Two mechanisms that could be responsible for the decrease in amplitude of the high-frequency fringes are as follows: (i) absorption which increases with frequency and (ii) a transition region between the damaged layer and the substrate in which the index of refraction varies smoothly.

Comparison of Figs. 2(a) and 2(b) shows that the decrease in fringe amplitude is essentially the same for 300-keV and 2.7-MeV implants. The thickness of the damaged layer for the 2.7-MeV implant is ~ 5.5 times that for the 300-keV implant, so that an extinction coefficient $k(\nu)$ that fits the 2.7-MeV data would predict very little decrease in amplitude for a 300-keV implant. The extinction coefficient k has been measured for amorphous sputtered Si by Brodsky *et al.*,[24] and the measured $k(\nu)$ predicts a much smaller decrease in amplitude of the high-frequency fringes than is observed even for the 2.7-MeV implanted sample. This is illustrated in Fig. 3 in which the measured reflections for 300-keV and 2.7-MeV implants are compared with predictions for a sharp interface with $k = 0$ and with k equal to Brodsky's experimental values.

This result is consistent with the earlier analyses of the GaAs and GaP interference spectra since the decrease in amplitude of the fringes in these earlier studies could not be fitted when measured values of k were used for these materials.[7] In these earlier analyses, which assumed sharp dielectric discontinuities, the amplitude of the fringes was fitted by varying the effective value of the index of refraction of the substrate at the interface. The values for the effective refractive index obtained in this way were intermediate between the literature values for n_c and the index of refraction of the damaged layers.

If there is a transition region in which the index of refraction changes smoothly with depth, the amplitude of the reflected wave decreases as the wavelength approaches the

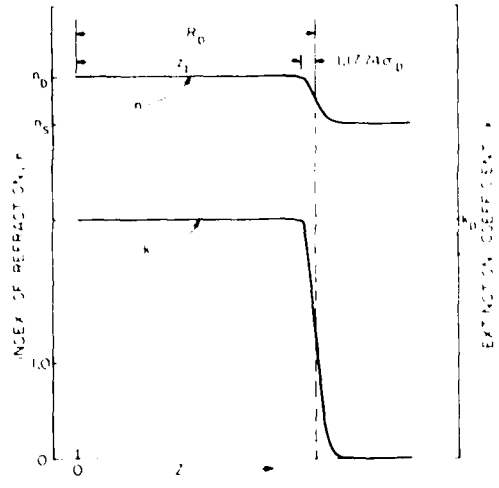

FIG. 4. Model for the variation with depth of the optical constants for the implanted samples of Tables I and III.

dimensions of the transition region. The decrease in amplitude does not depend upon the depth of the implant but only upon the width of the transition region. To describe the disordered layer and the transition region, a computer code was written which calculates the reflection R at normal incidence from the thin-film interference equations of Heavens.[7] This code computes R for an arbitrary number of layers having indices of refraction n_j, extinction coefficients k_j, and layer thicknesses Δz. Except where double layers were indicated by amplitude modulation of the interference pattern, the disordered region was taken as one uniform layer of index n_D and thickness z_1. Because the back surfaces of the samples were coarse lapped, the substrate was taken to be an infinitely thick layer of index n_s. The transition region was approximated by N layers of equal thickness Δz with n_j given by a half-Gaussian distribution of the form

$$n_j = n_s + (n_D - n_s)\exp[-(z_j - z_1)^2/2\sigma_D^2], \quad (2)$$

where $z_j = z_1 + (j-1)\Delta z$ and σ_D is the standard deviation. The extinction coefficient k is zero in the substrate and was assumed to have the same spatial dependence as n_D, with

$$k_j = k_D(\nu)\exp[-(z_j - z_1)^2/2\sigma_D^2]. \quad (3)$$

Figure 4 is a schematic representation of the model. The depth of the disordered region R_D was taken as the half-maximum position on the Gaussian, or $R_D = z_1 + 1.177\sigma_D$. The total width of the transition region was set equal to $4\sigma_D$.

In initial testing of the program it was found that the results converged for $N > 20$. All of the fits presented in this paper are for $N = 40$ layers in the transition region. The effect of the transition width on the amplitude of the high-frequency fringes is illustrated in Fig. 5 for $k = 0$, $n_D = 3.90$, $n_s = 3.45$, $R_D = 2.5\,\mu$m, and $\sigma_D = 0.025$, 0.05, and 0.1 μm. Comparison with the data presented in Fig. 2 indicates that a $\sigma_D \gtrsim 0.05\,\mu$m is appropriate.

The data presented in Fig. 2 also indicate that the reflection R increases at high frequencies due to the increase in $n(\nu)$. The indices of refraction for both the disordered and substrate regions were represented by a Sellmeier equation of the form

$$n = \left(A + \frac{B}{\Omega^2 - \nu^2}\right)^{1/2}, \quad (4)$$

where A, B, and Ω are constants, and ν is the frequency in units of cm^{-1}. The constants for the substrate were determined by a nonlinear least-squares fit of Eq. (4) to the values of $n(\nu)$ for crystalline silicon measured by Salt'zberg and Villa[8] with the result that $A_s = 4.1476$, $B_s = 5.8876 \times 10^4$ cm^{-2} and $\Omega_s = 27973$ cm^{-1}.

Assuming n_s to be given by Eq. (4) and the above constants, $k_s = 0$ at all measured frequencies, and k_D determined by absorption measurements, then the model incorporates five adjustable parameters: R_D, the depth of the disordered layer; σ_D, the "width" of the transition region; A_D, B_D, and Ω_D, which characterize the refractive index of the disordered region. The experimental reflection data were fitted with the model by using a nonlinear least-squares computer code which adjusted the values of selected parameters to minimize the reduced chi-square fit,

$$\chi^2 = \sum_{i=1}^{N} \frac{(R_{i\,\text{measured}} - R_{i\,\text{calculated}})^2}{N - N_p},$$

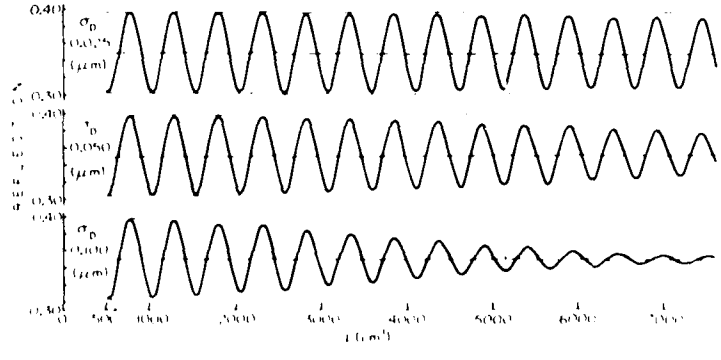

FIG. 5. Calculated curves for the model in Fig. 4 where $n_s = 3.45$, $n_D = 3.90$, and $\sigma_D = 0.025$, 0.050, and 0.100 μm. The influence of the transition region width is demonstrated.

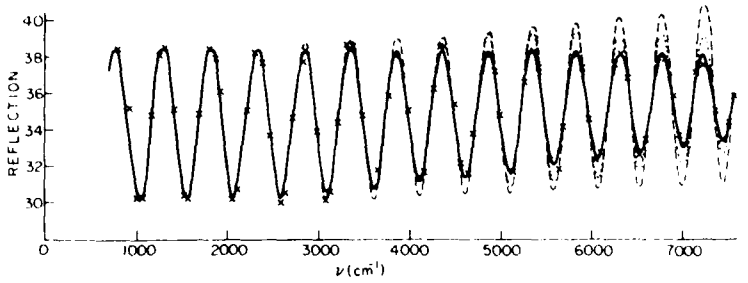

FIG. 6. Data for sample 78-6 with the solid curve being the best calculated fit—see parameter values in Table I. The dashed and dotted curves are for $\sigma_D = k_D = 0$ and $\sigma_D = 0$, $k_D = k$ (measured, from Ref. 7), respectively.

where N is the number of data points and N_p is the number of parameters varied. The number of data points used in each analysis was ~ 100. In the fitting of the data it was found the quantities A_D, B_D, and Ω_D could be simultaneously varied over a considerable range while maintaining a good fit to the data; however, the values of $n_D(\nu)$, R_D, and σ_D were well defined. Consequently, the results are given in terms of $n_D(\nu)$, R_D, and σ_D.

IV. EXPERIMENTAL RESULTS AND ANALYSES

A summary of implant conditions is presented in Table I. Samples 75-1–75-3 were implanted with a defocused ion beam; all others were raster scanned. Samples 78-6–78-8 were implanted at 200 °K; all others were implanted at room temperature. The fluences ranged from 1.0×10^{15} to 10.0×10^{16} ions/cm^2.

In all of the analyses which follow where k_D of the amorphous region was not set equal to zero, we have used the measurements of Brodsky *et al.* for the k for amorphous sputtered Si.[7,23] These measurements can be simply represented by the expression $k_D = c\nu^4$ with $c = 5.939\times10^{-18}$ cm^4. We have also measured the extinction coefficient for two Si samples implanted with 2.7-MeV P$^+$ ions and obtained values of k_D approximately 20% less than that obtained by Brodsky *et al.* for sputtered Si. This difference is not considered to be significant and has essentially no effect on the calculations.

In Fig. 6 the experimental results for sample 78-6 implanted with 2.7-MeV P$^+$ are compared with the best-fit calculation (solid curve) which utilized the measured values of the extinction coefficient k_D. The width of the transition region is $\sigma_D = 0.041\,\mu$m. If k_D is set equal to zero, the best-fit calculation is indistinguishable from the solid curve although the reduced χ^2 fit increases slightly from 0.83×10^{-3} to 1.05×10^{-3} and the width of the transition region increases to $\sigma_D = 0.053\,\mu$m. Also shown for comparison is the dashed curve for a sharp transition ($\sigma_D = 0$) and for no absorption ($k_D = 0$). The dotted curve presents the results of a calculation for a sharp transition ($\sigma_D = 0$) and k_D given by the measurements of Brodsky *et al.* It is clear that the measured decrease in the amplitude of the high-frequency fringes is greater than that which can be attributed to absorption and that it is necessary to include a transition region.

Referring back to Figs. 2(a) and 2(b), the dashed line is the predicted reflectivity R for a nonimplanted Si sample calculated from the values of n, measured by Saltzberg and Villa.[22] Measurements of nonimplanted samples were frequently repeated to serve as a check of the reproducibility of our measurements. These tests agreed well with the computed R and indicated that R could be determined with an accuracy of ± 0.005, which corresponds to an accuracy of n of ± 0.05.

The measured reflection R for sample 77-1 implanted with 300-keV P$^+$ ions is compared with the best-fit calculation (solid curve) in Fig. 7. The measured k_D was included and $\sigma_D = 0.044\,\mu$m was obtained. When k_D was set equal to zero, a best fit was obtained for essentially identical parameters. The reason for this result is made clear by the comparison of the dashed and dotted curves in Fig. 7. The dashed curve is for $\sigma_D = 0$ and $k_D = 0$; the dotted curve is for $\sigma_D = 0$ and $k_D = k_M$, the measured value. We see that the absorption has almost no effect in reducing the fringe amplitude at high frequencies. This result is expected because the thickness of the 300-keV implants is ~ 5.5 times less than that of the 2.7-MeV implants, and even in the thicker layer,

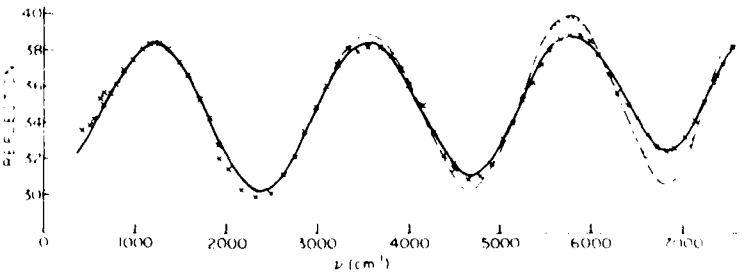

FIG. 7. Data for sample 77-1 with the solid curve being the best calculated fit—see parameter values in Table I. The dashed and dotted curves are for $\sigma_D = k_D = 0$ and $\sigma_D = 0$, $k_D = k$ (measured, from Ref. 7), respectively.

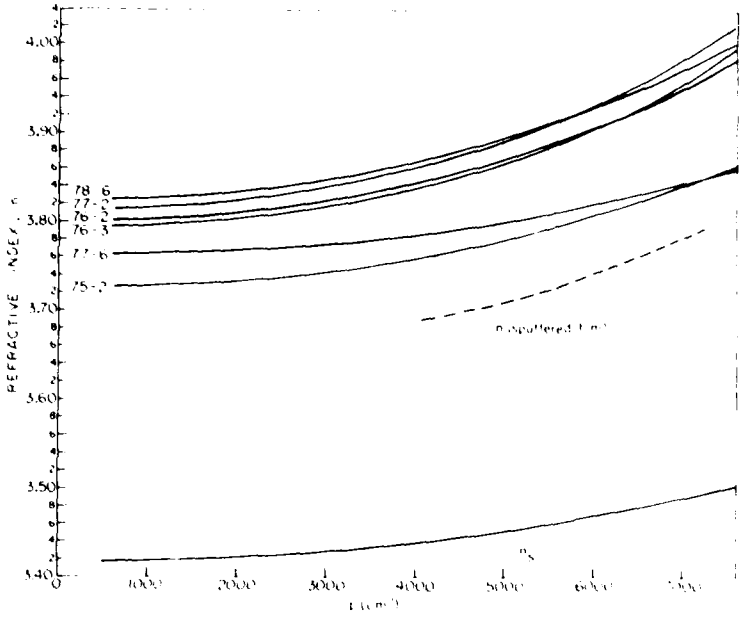

FIG. 8. Refractive index n_D versus frequency for a number of implanted samples. Also shown are the curves for a sputtered film (see Ref. 7) and crystalline Si (see Ref. 22).

the measured values of k_D do not account for the decrease in the high-frequency fringe amplitude.

Referring to Table I, we observe that the values of σ_D obtained for $k_D \neq 0$ are less than those obtained for $k_D = 0$. Except for three entries for which σ_D is indicated as being less than 0.01 μm, we see that the width of the transition is independent of ion species (P^+ or Si^+), energy, and fluence. The mean value of $\sigma_D = 0.035 \pm 0.009$.

There are three entries in Table I where a sharp transition ($\sigma_D \simeq 0$) between regions in the implanted sample is indicated. Sample 76-1 is double-layered in the implanted region. The measured reflection spectrum clearly shows the beating patterns in the interference pattern produced by multilayered samples. Least-squares fitting of the experimental results indicates that there is a lightly damaged surface layer of thickness 0.143 μm and a heavily damaged buried layer of thickness 0.388 μm. The width of the transition region between the lightly damaged layer and the heavily damaged layer is essentially zero ($\sigma_D < 0.01$ μm), the width of the transition region between the heavily damaged region and the substrate crystalline material is typically $\sigma_D = 0.052$ μm.

Samples 77-5 and 77-6, the two 200-keV P^+ implants, do not indicate double layers, but the interfaces between the damaged regions and the substrate are also sharp ($\sigma_D < 0.01$). These two samples were implanted simultaneously at room temperature, and we believe that the sharp interface is the result of some heating and partial annealing during the implant. This conclusion is based on the results of annealing studies which we are preparing for publication. These studies indicate that the first change observed in annealing at 500 °C is an increase in the amplitude of the high-frequency fringes due to a reduction in the width σ_D of the transition region between the damaged and undamaged Si. (Annealing effects at lower temperatures have not been investigated.) In addition, we note that the indices of refraction for the 0.143-μm-thick surface layer of sample 76-1 are closer to those of crystalline Si than to those of heavily damaged Si. The n_D values for the 200-keV samples (77-5 and 77-6) are both on the low side but they are not outside the expected range of n_D values due to uncertainties in R.

In Fig. 8 we present the indices of refraction for crystalline Si,[22] the indices for sputtered amorphous Si films,[7] and the indices for highly damaged Si obtained from fitting the reflection measurements from the indicated samples. The curves chosen for display were those representing the extreme changes in the indices of refraction and include data from P^+ implants at 200, 300, and 2700 keV and Si^+ implants at 300 keV. In comparing the present results with the indices of sputtered Si it is important to note that the accuracy ascribed to these latter measurements is $\sim 10\%$, so that these measurements agree within the quoted errors with the present measurements.

In Table I the indices of refraction for each calculation are given at $\nu = 500$, 4000, and 7500 cm^{-1}. Perusal of Table I and Fig. 8 indicates that there are no discernible trends in variation of the indices of refraction with ion species, energy, or fluence; instead, the variations in n_D appear to be those associated with the experimental accuracy of the reflection measurements.

Assuming that the variations in the calculated values of n_D are due to the uncertainties in the measurement of R, we

TABLE II. Indices of refraction for heavily damaged silicon

ν (cm^{-1})	$n_D + \delta n_D$
500	3.798 + 0.019
1000	3.800 + 0.019
1500	3.803 + 0.020
2000	3.808 + 0.020
2500	3.814 + 0.020
3000	3.821 + 0.021
3500	3.830 + 0.022
4000	3.841 + 0.022
4500	3.854 + 0.023
5000	3.869 + 0.024
5500	3.886 + 0.025
6000	3.905 + 0.027
6500	3.926 + 0.030
7000	3.952 + 0.032
7500	3.980 + 0.034
8000	4.013 + 0.038

have determined the index of refraction of highly damaged (amorphous) Si by taking the average of all our measurements at a given frequency. The results of this averaging are presented in Table II, and the quoted error is the standard deviation. These data can be represented by Eq. (4) with the parameters $A_D = 7.03$, $B_D = 2.64 \times 10^{-5}$ cm^{-1}, and $\Omega_D = 18\,860$ cm^{-1}.

In Table III we present a comparison of the various measurements of the thicknesses of the damaged region. R_p and σ_p are the projected range and straggling, respectively, calculated from LSS[24] theory for Si; R_D and σ_D are the depth and transition width, respectively, of the damaged region presented in Table I. The thickness of the damaged region was determined by He channeling measurements for four samples. The depth of the visual interface was determined by microscopic measurement of the width of the white layer along a beveled surface.

First, we note that σ_D and σ_p are unrelated. σ_D determines the width of the region in which there is a transition from heavily damaged to lightly damaged or crystalline material. σ_p is a measure of range straggling of the incident ions. σ_D appears to be unrelated to ion species, energy, or fluence for the fluence range studied (1×10^{14} to 10×10^{14} cm^{-2}). The constancy of σ_D is an indication of the saturation of the amount of disorder within the damaged region.

The width of the transition region was also determined by He channeling measurements for samples 77-1, 77-3, and 77-4, which were 300-keV implants of P$^+$ and Si$^+$. The width for all three samples was $\sigma_D = 0.025 \pm 0.010\,\mu$m, which is in reasonable agreement with the infrared average value $\sigma_D = 0.035 \pm 0.009\,\mu$m.

Although σ_D does not change with ion fluence, R_D does. For 2.7-MeV P$^+$ ions, R_D increases from 2.53 μm for 1.7×10^{14} ions/cm^2 to 2.61 μm for 10×10^{14} ions/cm^2; for 300-keV P$^+$ ions the depth increases from 0.51 to 0.55 μm as the fluence increases from 1×10^{14} to 3×10^{14} ions/cm^2. The same effect is noted for 300-keV Si$^+$ ions. These results again suggest that there is saturation in the amount of disorder produced when a well-defined amount of displacement damage is produced. These results are in accord with the measurements of Crowder and Title[7] for somewhat smaller fluences at 280 keV.

Comparison of R_D to LSS projected range calculations indicates that, for the fluence range studied, $R_D \simeq R_p + \sigma_p$. This correlation is shown in Fig. 9. For the few cases measured there is good agreement between the disorder depths determined by channeling measurements and R_D or $R_p + \sigma_p$. There is also agreement with the visual depth of

TABLE III. Comparison of measurements of depth of damage

Si Sample	Ion	Ion energy (keV)	Ion fluence ($\times 10^{14}$ cm^{-2})	R_D (μm)	σ_D (μm)	R_p (μm)	σ_p (μm)	R_c	He channeling (μm) σ_c	Visual[a] layer (μm)
78-6	P$^+$	2700	1.74	2.52	0.041	2.50	0.20	...	...	2.59
78-7	P$^+$	2700	1.74	2.54	0.035	2.50	0.20	...	...	...
75-1[b]	P$^+$	2700	6.4	...	...	2.50	0.20	0.9	...	...
								3.2	...	
75-2	P$^+$	2700	6.4	2.54	0.036	2.50	0.20	...	...	...
75-3[b]	P$^+$	2700	6.4	...	...	2.50	0.20	...	...	...
78-8	P$^+$	2700	10.0	2.61	0.032	2.50	0.20	...	...	2.61
76-3	P$^+$	300	1.0	0.507	0.037	0.38	0.10	...	...	...
76-4	P$^+$	300	1.0	0.506	0.035	0.38	0.10	...	...	(0.40)
77-1	P$^+$	300	3.0	0.551	0.044	0.38	0.10	0.54	0.025	(0.36)
77-2	P$^+$	300	3.0	0.549	0.045	0.38	0.10	...	...	(0.30)
76-1[b]	Si$^+$	300	1.0	0.143	< 0.01[c]	0.41	0.10	...	...	...
				0.531	0.052					
76-2	Si$^+$	300	1.0	0.569	0.040	0.41	0.10	...	...	...
77-3	Si$^+$	300	3.0	0.611	0.038	0.41	0.10	0.60	0.025	(0.25)
77-4	Si$^+$	300	3.0	0.624	0.030	0.41	0.10	0.57	0.025	(0.19)
77-5	P$^+$	200	1.0	0.407	< 0.01[c]	0.25	0.08	...	...	(0.21)
77-6	P$^+$	200	1.0	0.407	< 0.01[c]	0.25	0.08	...	...	...

[a] See text for discussion of values in parentheses
[b] Double-layered sample
[c] Believed to be due to partial annealing during implant. See text for discussion.

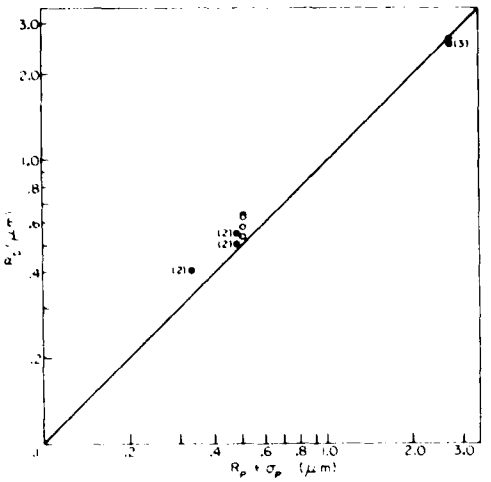

FIG. 9. Thickness of the damaged layer deduced from the curve fitting of the interference data versus $R_p + \sigma_p$ calculated from LSS theory (see Ref. 24). The open circles are for Si$^+$ ion implants and the closed circles are for P$^+$ ions. The parentheses indicates the number of superimposed data points.

the interface for the high-energy implants. However, the comparison breaks down for the low-energy implants where the visual depths are considerably smaller than R_D, $R_p + \sigma_p$, or the depths from channeling. There is no evidence in either the infrared or channeling measurements for an interface at the positions indicated by the visual measurements.

In previous work, Crowder and Title[1] obtained good agreement between infrared and visual depths for 280-keV P$^+$ ions implanted in Si. In this previous work the visual observation of the interface was accomplished by anodic oxidation and HF stripping of adjacent implanted and unimplanted areas. Their infrared depths are in agreement with our lower-energy results, and their visual depths are slightly less than the infrared depths. Thus, the difficulty appears to lie in the technique used here in producing the bevel. This beveling technique is frequently used in the semiconductor industry and apparently was not reliable for the low-energy high-dose implants in Si.

V. DISCUSSION AND CONCLUSIONS

The model given in Sec. III gives good representation of the experimental results presented in Sec. IV with physically reasonable values of the parameters. The results indicate

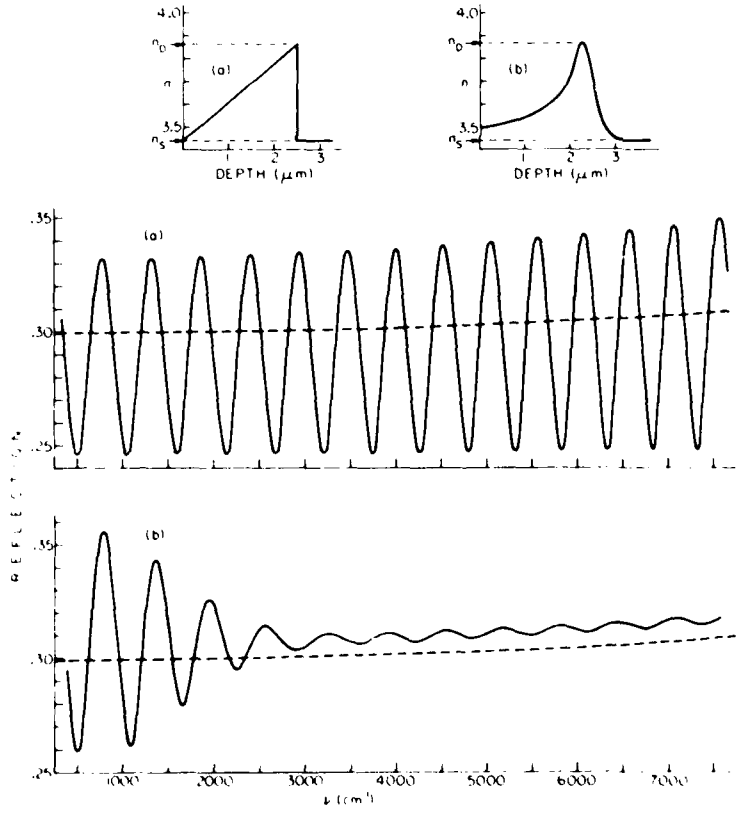

FIG. 10. The calculated reflection curves for two assumed refractive index profiles. The profile (b) is similar to the energy deposition curve for the 2.7-MeV P$^+$ ions of Fig. 1. The dashed curves are for the reflectivity when $n = n_s$ at all depths.

that $n_D(v)$ shows little, if any, dependence upon ion species (P^+ or Si^+), ion energy, ion fluence, or sample temperature during the implant (approximately 200 °K and room temperature). In almost all cases it was necessary to include a transition region from n_D to n_s, and the σ_D of the half-Gaussian used to characterize the transition region averaged 0.035 μm. The few exceptions have been discussed. The $n_D(v)$ curves for all samples measured lie within a range which was previously indicated as that attributable to the nonreproducibility in R. The data of Table II represent the best estimate of $n_D(v)$ from all of the measurements made here. The result is in reasonable accord with previous and generally less rigorous estimates of n_D.

One might question the validity of the assumption in our model that n_D is constant in depth within the heavily disordered region as shown in Fig. 4. It may be recalled that the model leads to a reflection spectrum in which interference minima R_{min}, are at R_s values given by

$$R_s \quad \left(\frac{n_s - 1}{n_s + 1}\right)$$

as long as $\lambda_{medium} \gg \sigma_D$, an attenuated fringe amplitude when λ_{medium} is the same order of magnitude as σ_D, and a mean reflection R_{mean} given by

$$R_D \quad \left(\frac{n_D - 1}{n_D + 1}\right)^2,$$

where λ is the wavelength. In no case is R_{min} less than R_s or R_{mean} unequal to R_D when n_D is uniform in depth. All of the experimental data presented in Figs. 2, 3, 6, and 7 and for the remaining samples of Tables I and III fit these conditions. If one removes the restriction of the spatial uniformity of n_D, then the calculations predict an R_{min} which can lie below R_s. Two examples are given in Fig. 10 for the hypothetical n_D profiles indicated. In both cases the fringes have R_{min} values at low frequency which are substantially less than R_s. The R_s is also shown as a dashed curve in Fig. 10. When there are spatial changes in n_D that involve sharp transitions from one value to another with changes in depth z, then structure or multilayer effects would be present in the interference pattern,[12] effects not observed in the data except in the few special cases which probably involve annealing as already noted and discussed.

ACKNOWLEDGMENTS

The authors would like to thank P.R. Malmberg for several of the high-energy ion implantations and G. Mueller for his aid in the infrared measurements. One of us (C.N.W.) wishes to thank Dr. J. McElhinney and Dr. J.W. Butler of the Naval Research Laboratory for their continued support. The research of G.K. Hubler was sponsored in part by the Navy Material Command and the Air Force Materials Laboratory. The research of C.N. Waddell and W.G. Spitzer command, USAF, under Grant No. AFOSR-F49620-78-C0065. The United States Government is authorized to reproduce and distribute reprints for Governmental purposes notwithstanding any copyright notation herein.

[1] B.L. Crowder and R.S. Title, 1st *International Conference on Ion Implantation in Semiconductors*, edited by I. Ruge and J. Graul (Springer, Berlin, 1971), p. 87.
[2] J.F. Gibbons, Proc. IEEE **60**, 1062 (1972).
[3] D.J. Mazey, R.S. Nelson, and R.S. Barnes, Philos. Mag. **17**, 1145 (1968).
[4] L.D. Glowinski, K.N. Tu, and P.S. Ho, Appl. Phys. Lett. **28**, 332 (1976).
[5] W. Rothemund and C.R. Fritzsche, Appl. Phys. **10**, 111 (1976).
[6] B.L. Crowder, R.S. Title, M.H. Brodsky, and G.D. Pettit, Appl. Phys. Lett. **16**, 205 (1970).
[7] M.H. Brodsky, R.S. Title, K. Weiser, and G.D. Pettit, Phys. Rev. B **1**, 2632 (1970).
[8] I. Csepregi, J.W. Mayer, and T.W. Sigmon, Phys. Lett. A **54**, 157 (1975).
[9] I. Csepregi, E.F. Kennedy, S.S. Lau, and J.W. Mayer, Appl. Phys. Lett. **29**, 645 (1976).
[10] W.G. Spitzer, C.N. Waddell, G.H. Narayanan, J.E. Fredrickson, and S. Prussin, Appl. Phys. Lett. **30**, 623 (1977).
[11] A.H. Kachare, W.G. Spitzer, and J.E. Fredrickson, J. Appl. Phys. **47**, 4209 (1976).
[12] A.H. Kachare, W.G. Spitzer, J.E. Fredrickson, and F.K. Euler, J. Appl. Phys. **47**, 5274 (1976).
[13] A.H. Kachare, W.G. Spitzer, F.K. Euler, and A. Kahan, J. Appl. Phys. **45**, 2938 (1974).
[14] A.H. Kachare, J.M. Cherlow, J.T. Yang, W.G. Spitzer, and F.K. Euler, J. Appl. Phys. **47**, 161 (1976).
[15] O.S. Heavens, *Optical Properties of Thin Films* (Butterworths, London, 1964).
[16] The first number identifies the wafer and the second identifies the piece cut from the wafer.
[17] H.E. Bennett, M. Silver, and E.J. Ashley, J. Opt. Soc. **53**, 1089 (1963).
[18] The energy expended in displacement collisions was computed with the NRL energy deposition code E-DEP-1 see I. Manning and G.P. Mueller, Comp. Phys. Commun. **7**, 85 (1974).
[19] The exceptions are samples (75-1, 75-3, and 76-1) of Table I in which there is a thin less heavily damaged region on the surface. This is believed to be due to inadequate temperature control which produced annealing during the implantation.
[20] I. Csepregi, E.F. Kennedy, S.S. Lau, J.W. Mayer, and T.W. Sigmon, Appl. Phys. Lett. **29**, 645 (1976).
[21] T.E. Seidel, G.A. Pasteur, and J.C.C. Tsai, Appl. Phys. Lett. **29**, 648 (1976).
[22] C.D. Saltzberg and J.J. Villa, J. Opt. Soc. **47**, 244 (1957).
[23] N.F. Mott and E.A. Davis, *Electronic Processes in Non-Crystalline Materials* (Clarendon, Oxford, 1971), p. 408 and 409, and Ref. 7.
[24] W.S. Johnson and J.F. Gibbons, *Projected Range Statistics in Semiconductors*, 1970 (Stanford U.P. Stanford, Calif., 1970). J.F. Gibbons, W.S. Johnson, and S.W. Mylroie, *Projected Range Statistics in Semiconductors and Related Materials* (Halsted, Stroudsburg, Pa., 1975).

Section IV.C

PLASMA REGION IN HIGH-FLUENCE IMPLANTS OF PHOSPHORUS IN AMORPHIZED SILICON

W. G. Spitzer,[1] J. S. Ko,[1] and C. N. Waddell,[1]

G. K. Hubler,[2] and J. E. Fredickson[3]

[1]Physics and Materials Science Departments
University of Southern California
Los Angeles, California

[2]Materials Modification and Analysis Branch
Radiation Technology Division
Naval Research Laboratory

[3]Physics-Astronomy Department
California State University
Long Beach, California

This work was supported in part by the Naval Material Command,
the Air Force Materials Laboratory (NRL), and by
the Air Force Office of Scientific Research, Air Force Systems Command (USC)

Plasma region in high-fluence implants of phosphorus in amorphized silicon

W. G. Spitzer, J. S. Ko, and C. N. Waddell

Physics and Materials Science Departments, University of Southern California, Los Angeles, California 90007

G. K. Hubler

Naval Research Laboratory, Washington, D.C. 20375

J. E. Fredrickson

Physics-Astronomy Department, California State University, Long Beach, California 90840
(Received 31 October 1978; accepted for publication 16 January 1979)

Phosphorus ions were implanted into silicon previously made amorphous by implantation with neon ions of projected range considerably greater than that of the P^+ ions. Comparison of the annealing behavior for this case with that for P^+-only implants indicates that free-carrier plasma formation in the region of high phosphorus concentration does not occur until the material has recrystallized.

PACS numbers: 78.20.Dj, 61.70.Tm, 81.40.Tv

In an earlier paper [1] we reported the observation of strong free-carrier plasma effects in the behavior of the infrared reflection of high-resistivity Si implanted with high fluences of high-energy (2.7 MeV) P^+ ions. The plasma was detected after thermal annealing. After a 500 °C/20 h anneal, approximately 0.2 μm of the amorphous region had epitaxially recrystallized by regrowth [2] of the amorphous-crystalline (a-c) interface towards the original surface. Spreading resistance profiling after annealing indicated the formation of a low-resistivity region near the a-c interface but mainly in the amorphous region. It was suggested that this resistivity change results from short-range reordering which could produce increases in the carrier density of a heavily P-implanted region, and therefore indicates that a plasma could exist within the heavily damaged or amorphous region. Brodsky *et al* [3] have reported that the index of refraction of sputtered amorphous-Si films decreases during thermal anneal without crystallization. The present authors have observed the same effect [4] in ion-implanted Si.

This suggestion was supported by calculation of the infrared reflection spectrum [1] which used a simple layer model which included a plasma layer having the width and location indicated by the spreading resistance measurements. However, later calculations with a more refined model incorporating a Gaussian plasma region and smooth changes of the refractive index at the a-c interface indicated that best fits were obtained when the plasma was in crystalline material near the a-c interface. These later results suggested that the spreading resistance measurements could be in error because of mechanical or electrical punching through a thin high-resistivity layer on top of the conducting region.

In this communication we report the results of an experiment in which P^+ ions were implanted into a region previously amorphized to a much greater depth than the range of the P^+ ions to determine whether the plasma initiates in the annealed but still amorphous region or within an epitaxially recrystallized region. It will be shown that the plasma effects are not observed until the epitaxial recrystallization reaches the region of high P concentration.

To facilitate comparison with previous results [1] the (111) oriented Si samples were cut from the same ingot of high-resistivity single-crystal Si. The implantations were done with the samples maintained at low temperature and with the ion beam 8° from the surface normal. Several samples were implanted with 2.7-MeV P^+ ions only; the others were first implanted with 4-MeV Ne^+ ions and then with 2.7-MeV P^+ ions. The implantation conditions as well as some of the results for these samples are summarized in Table I. Note that the measured depth of amorphous layer after the 4-MeV Ne^+ implant was 3.7 μm compared to 2.7 μm for the 2.7-MeV P^+ implant (the projected range and standard deviation[5] for 2.7-MeV P^+ ions are $R_p = 2.5\ \mu$m and $\sigma_p = 0.2\ \mu$m).

Figures 1 and 2 compare the reflection spectra for room-temperature and higher-temperature anneal conditions of a sample (No.3) implanted with Ne + P with others (Nos. 1 and 2) implanted with P only. The P^+ ion energies were the same and the fluences similar in each case. The layer thicknesses given in Table I were calculated from the fringe spacing in the frequency interval $4000 < \nu < 7000\ \text{cm}^{-1}$ with $n = 3.9$ as the average index of refraction of heavily damaged Si. This n value is obtained from the mean reflection [4] in the given frequency range. In the cases where the recrystallization reached the front surface, the mean value of the reflection indicated that the refractive index of the annealed material had reduced to ~ 3.5 which is close to the average value of ~ 3.4 for crystalline Si.

Comparison of the room-temperature (as-implanted) curves of Figs. 1 and 2 shows that the amorphous layer for Ne + P implantation is thicker than for P-only implanta-

 0021-8979/79/053775-03$01.10

TABLE I. A summarization of our results.

Sample No.	Implanted ions—energy (MeV)	Fluence (ions/cm²)	Implant temp (°K)	Anneal temp (°C)/time (h)	Damage[a] layer thickness(μm)	Plasma observed
1	P^+—2.7	1.74×10^{14}	200	Room temp	2.7	No
				500/10	2.5	indication
				500/30	2.4	Yes
				500/50	2.0	Yes
2	P^+—2.7	1.74×10^{14}	200	Room temp	2.7	No
				600/0.5	1.9	Yes
				600/10	*b*	Yes
3	P^+—2.7	2.0×10^{14}	200	Room temp.	3.7	No
	Ne^+—4.0	1.0×10^{14}	77	500/10	3.6	No
				500/60	3.6	No
				500/60 + 600/1.5	2.9	No
				500/60 + 600/2.5	2.8[c]	No
				500/60 + 600/4.5	*b*	Yes
				500/60 + 600/10	*b*	Yes

[a]Calculated from the number of fringes between 4000 and 7000 cm^{-1} using the average refractive index for amorphous Si of 3.9 in this frequency range.

[b]Mean value of the reflection indicates that the regrowth has gone through the entire layer.

[c]Only approximate as observed beatlike pattern means more than one layer.

tion. Sample 1 (P only) clearly indicates the low-frequency effects of the plasma beginning after annealing at 500 °C for 10 h. The low-frequency fringes grow in amplitude until ~ 30 h with only minor changes occurring for still longer anneal times. Figure 1 shows a curve for sample 1 after a 500 °C/50 h anneal. Sample 2 (P only) has fully developed plasma fringes after 0.5 h at 600 °C, and the recrystallization is equivalent to ~ 50 h anneal at 500 °C.

When sample No. 3 (Ne + P) is annealed at 500 °C, there is a slight reduction in the amorphous layer thickness after ~ 10 h with no further measurable changes occurring after 60 h. There are small changes in the high-frequency fringe amplitude which indicate some spatially dependent annealing of the refractive index of the amorphous region, but there is no indication of a plasma. After further annealing at 600 °C for 1.5 and 2.5 h, there was recrystallization and regrowth at the a-c interface, but still no evidence of the plasma effect. There was structure in the fringe spectra which indicated that the refractive index varied with depth. After an additional 2-h anneal at 600 °C (4.5 h total) the plasma was fully developed and the amorphous layer was

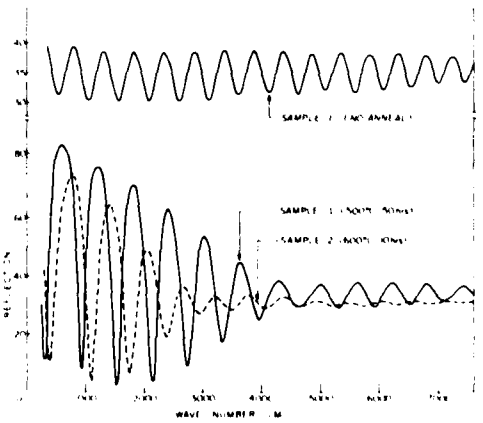

FIG. 1. Reflection versus wave number at room temperature for sample 1 before high-temperature annealing and after annealing at 500 °C for 50 h, and for sample 2 after annealing at 600 °C for 10 h.

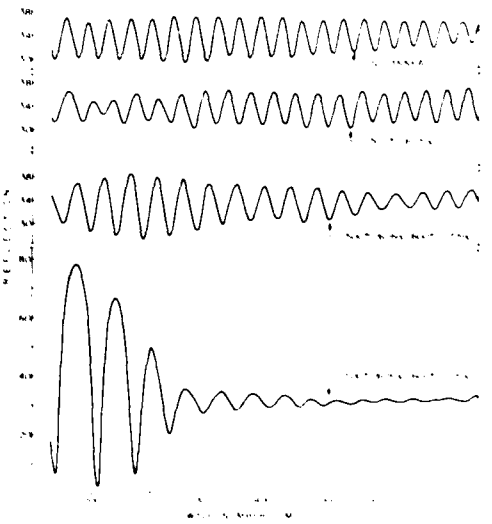

FIG. 2. Reflection versus wave number at room temperature for sample 3 at four different annealing stages, room-temperature annealing, 500° C/60 h, 500 °C/60 h + 600 °C/1.5 h and 500 °C/60 h + 600 °C/10 h.

completely recrystallized. The final anneal curves for samples 2 and 3 of Figs. 1 and 2 are very similar, indicating that the final dielectric state of the P- and Ne + P-implanted samples are essentially the same.

Similar measurements of another pair of P- only and Ne + P- implanted samples in which the incident energies were reduced $\sim 20\%$ gave very similar annealing results. However, in this case meaningful layer thicknesses cannot be given because the Ne + P- implanted sample did not recrystallize uniformly across the surface. This sample recrystallized in from the sample edges. Once initiated, this regrowth proceeded at a greater rate than that from the underlying crystalline material, which is consistent with measurements which show that the {111} direction is the slowest regrowth direction. [7]

The experimental results shown in Figs. 1 and 2 and summarized in Table I clearly demonstrate that the plasma does not develop due to local reordering in the amorphous region but rather that the plasma develops in the P-implanted region only after recrystallization. The thicknesses of the amorphous region for the Ne + P sample in Table I indicate that the regrowth proceeds until the thickness of the amorphous layer slightly exceeds $R_p + \sigma_p$ for the P implants without observation of the plasma even though the anneal times greatly exceeded those required to produce the plasma in the P- only implanted samples. In the case of samples implanted with P only, calculations to be published [4] have shown that the initial development of the plasma involves the tail of P ions which extend past the a-c interface into a region where the material is less heavily damaged. When this damage is annealed, carriers are produced and the plasma effect is seen.

This research was sponsored in part by the Air Force Office of Scientific Research, Air Force Systems Command, USAF. The research of one of the authors (G.K.H.) was sponsored in part by the Navy Material Command.

[1] W G Spitzer, C N Waddell, G H. Narayanan, J E Fredrickson, and S Prussin, Appl. Phys. Lett. **30**, 623 (1977)
[2] L. Csepregi, J W Mayer, and T W Sigmon, Phys Lett. A **54**, 157 (1975), Y Tamminga and W J M Josquin, Appl. Phys. Lett **32**, 13 (1978)
[3] M H Brodsky, R S Title, K Weiser, and G D Pettit, Phys Rev B **1**, 2632 (1970)
[4] W G Spitzer, J S Ko, C N Waddell, G K Hubler, and J E Fredrickson (unpublished)
[5] Values extrapolated from the calculations of J F Gibbons, W S Johnson, and S W Mylroie [*Projected Range Statistics* (Dowden, Hutchinson, and Ross, Stroudsburg, Pa 1975)]
[6] A H Kachare, W G Spitzer, J E Fredrickson, and F K Euler, J Appl Phys **47**, 5374 (1976), also G K Hubler, C N Waddell, W G Spitzer, J E Fredrickson, S Prussin, and R G Wilson (unpublished)
[7] L. Csepregi, J W Mayer, and T W Sigmon, Appl Phys Lett **29**, 92 (1976)

Section IV.D

HIGH-DOSE IMPLANTATION AND ION-BEAM MIXING

J. W. Mayer,[1] S. Lau,[1] B. Tsaur.[1]

J. M. Poate,[2] and J. K. Hirvonen[3]

[1]California Institute of Technology
Pasadena, California

[2]Bell Laboratories
Murray Hill, New Jersey

[3]Materials Modification and Analysis Branch
Radiation Technology Division
Naval Research Laboratory

This research wsas supported in part by the U. S. Army Research Office under the Joint Services Electronics Program (CalTech) by the Office of Naval Research (NRL)

HIGH-DOSE IMPLANTATION AND ION-BEAM-MIXING*

James W. Mayer, Silvanus S. Lau and Bor-Yeu Tsaur
California Institute of Technology
Pasadena, California

John M. Poate
Bell Laboratories
Murray Hill, New Jersey

James K. Hirvonen
Naval Research Laboratory
Washington, D. C.

Substitutional solid solutions and metastable phases in single-crystal metals can be produced by ion bombardment either by ion implantation to high-dose levels of one of the elements or by implantation of inert ions through a thin film to induce atomic mixing between the film and the single-crystal substrate. In this paper we compare these two methods of high-dose implantation and ion-beam-mixing to introduce Au and Pd into single-crystal Cu. In direct implantation the maximum concentration of implanted ions is determined, by the sputtering effects whereas in ion-beam-mixing the concentration is determined by the film thickness and the amount of interdiffusion over the penetration depth of the energetic ions.

With implantation of $1 \times 10^{17}/cm^2$ Au or Pd ions at 150 keV into <110> Cu high substitutional concentrations at about 6 atomic % were achieved. With ion-beam-mixing of ~ 100 Å Au or Pd films by 300 keV Xe ions at ion doses $\lesssim 1 \times 10^{16}/cm^2$, substitutional concentrations twice as high ($\simeq 12$ atomic %) were achieved. With thicker films, higher concentrations of Au and Pd were achieved with polycrystalline solid solutions formed at Au and Pd concentrations above 30 atomic %.

*This research was supported in part by the U.S. Army Research Office (H. Wittmann) under the Joint Services Electronics Program (DAAG-29-77-C-0015).

Introduction

Ion implantation is now used routinely to modify the properties of materials. An indication of the usage is given by the change in the name of the Implantation Conference Series which started in 1970 as "Ion Implantation in Semiconductors" and is now called "Ion Beam Modification of Materials". In the field of modification of the near-surface region of metals, considerable attention has been directed toward the physical properties of the metal, such as improvements in friction and wear (1). Another aspect is the study of metastable phases in metals produced by ion implantation (2). Amorphous layers can be formed (3,4) as well as substitutional solid solutions (5-7).

Relatively high doses of implanted ions, generally $\gtrsim 1 \times 10^{17}/cm^2$, are required to obtain concentrations of implanted species of about 10 atomic %. Aside from the long implantation time, the process is limited by sputtering effects which establish the maximum concentration which can be achieved by implantation (8). This sputtering limitation sets a strict constraint on using direct implantation to produce high concentration alloyed layers.

In order to achieve higher concentrations than those achievable by direct implantation, one can deposit a thin film of the given species on the substrate and then intermix the film and substrate by bombardment of energetic ions which penetrate through the film-substrate interface. With metal films on silicon, it has been shown that dose levels around $10^{15}/cm^2$ can produce silicide phases (9). At higher doses, but still an order of magnitude below that used in direct implantation, a progressive intermixing to redistribute the metal deeper into the samples occurs (10).

In this paper we compare these two methods, direct implantation and ion-beam-mixing, for introducing Au and Pd into single-crystals of Cu. In a previous study (11) we compared the two methods to form substitutional Au-Cu and Ag-Cu solid solutions. The experimental concept and phase diagrams of the Au-Cu and Pd-Cu system are shown in Fig. 1.

Experimental Procedure

Single-crystal Cu, <110> oriented, samples were etch-polished at Bell Laboratories. Backscattering and channeling analysis with 1.8 MeV ^4He ions were made at Bell Labs to evaluate the amount of residual disorder. High-dose implantation of 150 keV Au and Pd ions to doses of up to 1×10^{17} ions per cm^2 were carried out at the Naval Research Laboratory. Channeling measurements with 1.5 MeV ^4He ions were made at Bell Labs to determine the

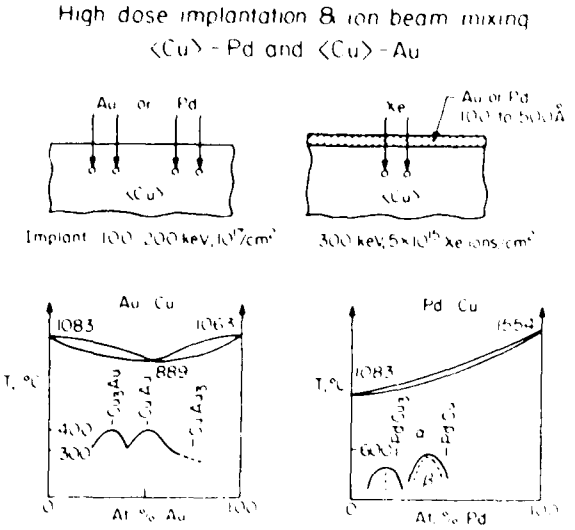

Fig. 1 - Schematic diagrams of the experiment concept and the Au-Cu and Pd-Cu phase diagrams.

implanted ion concentration and substitutional fraction.

Thin metal films a few hundred angstroms thick were prepared at Caltech by electron-gun evaporation of Au or Pd onto the <110> Cu substrates in an oil-free vacuum system. Ion-beam-mixing was carried out at Caltech by implanting 300 keV Xe ions to doses of 1×10^{15} to 1×10^{16} ions/cm^2 at beam current densities of about 1 μA/cm^2. To minimize beam heating effects, the samples were glued onto the sample holder using a thermally conductive compound. Backscattering and channeling analyses were made at Caltech and Bell Laboratories.

Experimental Results

High-Dose Implantation

A concentration of 6 at. % Pd was produced by implantation of $\sim 10^{17}$ Pd/cm^2. As indicated by the difference between the random and aligned spectra of Fig. 2, more than 90% of the Pd was on substitutional sites. The results obtained with Pd and Au (5) implantations are similar: high substitutional fraction at concentrations between 5 and 6 at. %.

Ion-Beam-Mixing - Concentrations ≈ 10 at. %

The objective of this set of experiments was to use ion-beam-mixing to obtain Pd or Au concentrations near those found in direct implantation so that a direct comparison of the two techniques could be made. Film thicknesses of about 100 Å and ion doses up to 10^{16}/cm^2 were used. The data in Fig. 3 for Pd on Cu indicates that a substitutional fraction of 72% can

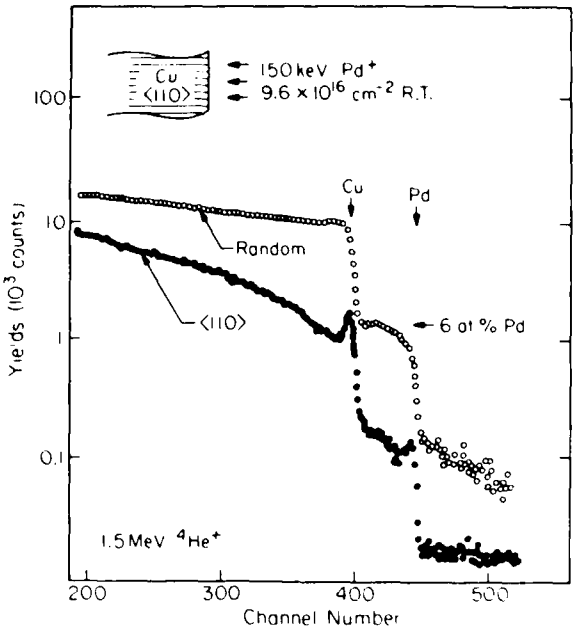

Fig. 2 - Random and <110> aligned spectra for 1.5 MeV ^{4}He ions incident on Pd implanted Cu.

be achieved at a Pd concentration of 11 at. %. The results shown in the Table indicate that high substitutional fractions of Au or Pd can be

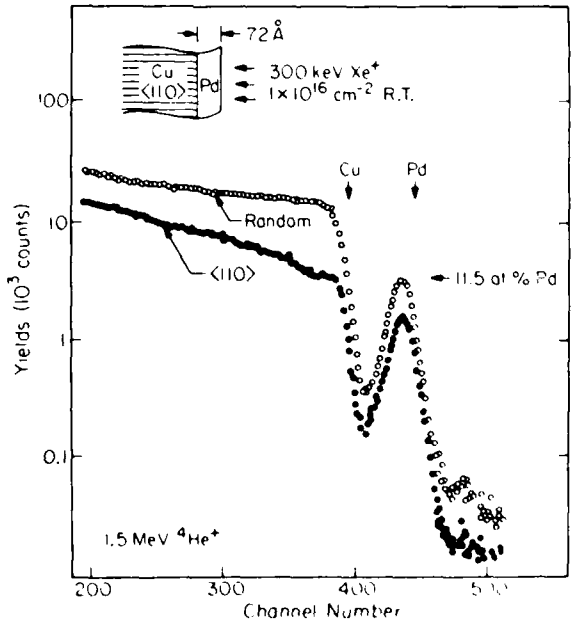

Fig. 3 - Random and <110> aligned spectra for 1.5 MeV ^{4}He ions incident on an ion mixed sample (see schematic).

Table I. Comparison of Ion-Beam-Mixing and High-Dose Implantation

Incorporation Of Au and Pd in ⟨110⟩ Cu

Cu ⟨100⟩	Implantation 150 keV Au, Pd	Ion Beam Mixing 300 keV Xe
Au	dose $\sim 1 \times 10^{17}/cm^2$ conc ~5 at % subst ~100 %	$t_{Au} = 160$ Å dose $\sim 5 \times 10^{15}/cm^2$ conc ~12 at % subst ~96 %
Pd	dose $\sim 1 \times 10^{17}/cm^2$ conc ~6 at % subst ~96 %	$t_{Pd} = 72$ Å dose $\sim 1 \times 10^{16}/cm^2$ conc ~11 at % subst 72 %

obtained by ion mixing. As in the case of Ag (11), both direct implantation or ion-beam-mixing give comparable results; however, an order of magnitude or higher dose is required with high-dose implantation as compared to ion-beam-mixing.

Ion-Beam-Mixing - High Concentrations

The objective of this set of experiments was to achieve concentrations well in excess of those that can be obtained by direct, high-dose implantation. The samples were prepared by depositing thicker films, thicknesses between 150 and 500 Å, than those described in the previous section where the objective was to achieve Pd or Au concentrations near 10 at. %. In all cases, the film thicknesses were less than the range of 300 keV Xe ions.

With these thicker films, differences in the substitutional fraction of Au and Pd became apparent. The data in Fig. 4 shows that 23 at. % of Au in Cu can be achieved by implanting Xe through a 300 Å Au film. The substitutional fraction is not as high (≈ 50%) as that obtained in lower concentrations of Au and the aligned yield in the Cu is higher. However, for the same concentration (≈ 25 at. %) of Pd, the amount of disorder in the near-surface region was higher and, as shown in Fig. 5, there was no difference in the Pd aligned and random yields. X-ray diffraction measurements showed the presence of a polycrystalline layer.

With the thicker films of Au and Pd on Cu, backscattering measure-

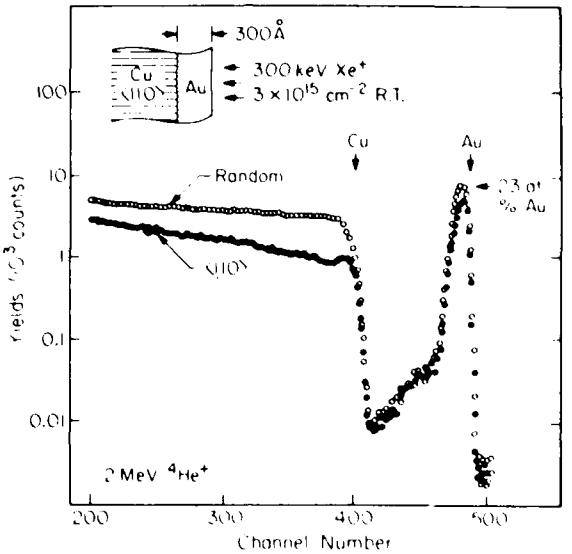

Fig. 4 - Random and aligned spectra for 3.0 MeV ^{4}He ions incident on an ion mixed Au film on Cu.

ments showed that the initial stages of ion-beam-mixing led to interdiffusion and reactions at the interface. The interfacial reactions are similar to those found in ion-mixed layers on silicon in which silicide layers are formed. In the present case, polycrystalline solid solutions are formed.

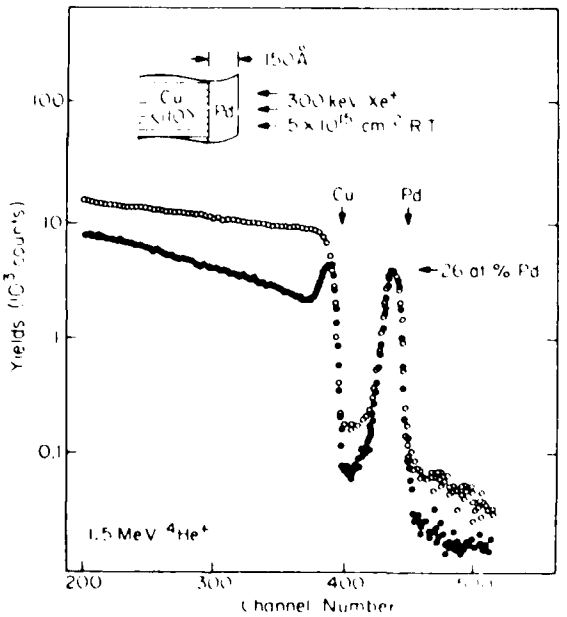

Fig. 5 - Random and aligned spectra for 1.5 MeV ^{4}He ions incident on an ion mixed Pd film on Cu.

The data in Fig. 6 shows a random spectrum for a 470 Å thick Pd film on Cu, and the aligned and random spectra after mixing with a dose of $5 \times 10^{15}/cm^2$ Xe ions. The spectra show that intermixing occurs in the interfacial layer and that the reacted region is highly disordered. The Cu signal does not

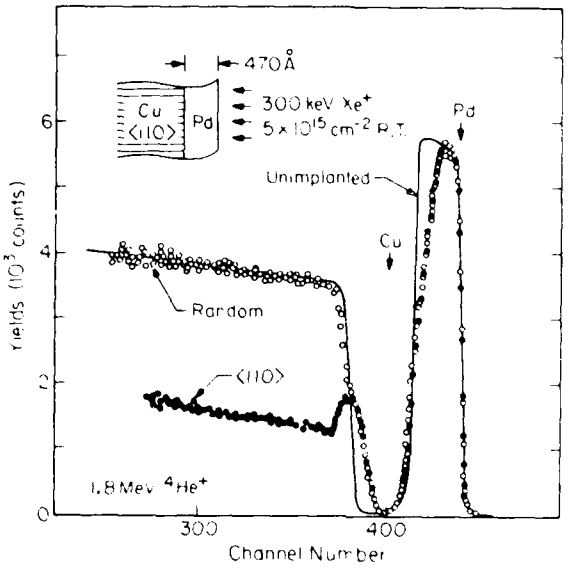

Fig. 6 - Random and aligned spectra for 470 Å thick Pd films on <110> Cu.

extend to the surface energy position, and the Pd signal does not extend down to depths comparable to the penetration of the Xe ions. These results indicate that the initial extent of the interdiffusion is confined to the region around the interface and does not occur over the entire depth of the Xe collision cascade. This limited extent of interdiffusion is similar to that found in silicide forming systems. At higher doses, the Cu signal reaches the surface position and the Pd signal broadens and decreases in height. Ion-beam-mixing then can lead to diffusion and reaction of the entire Au or Pd layer as long as the ion range is substantially greater than the film thickness.

Ion-Beam-Mixing - Concentration versus Dose

The objective of this set of experiments was to determine the concentration and substitutional fraction that could be obtained for a given film thickness at different ion doses. The concept was that increased ion doses would lead to increased amount of interdiffusion and hence decreased concentrations of Pd or Au in Cu.

The data in Fig. 7 shows that for a given film thickness, the con-

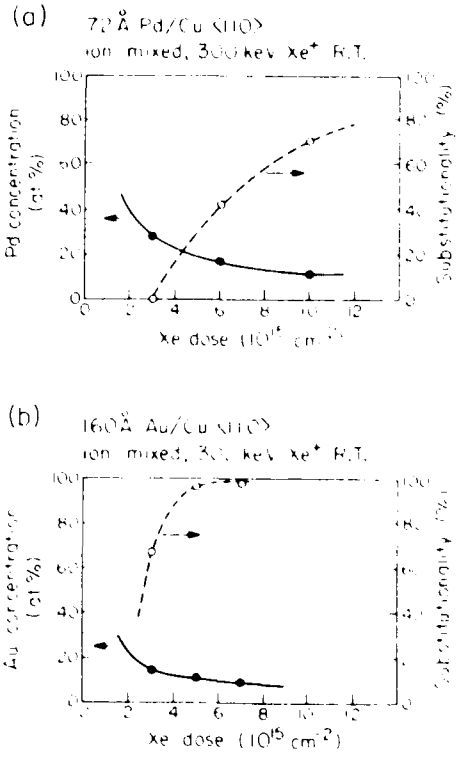

Fig. 7 - Atomic concentration (left axis) and substitutional fraction (right axis) versus ion dose for Pd (upper figure) and Au (lower figure) films on Cu.

centration of Pd (upper) and Au (lower) decreases with increasing ion dose. The substitutional fraction increases as the concentration decreases. However, there is a difference between Au and Pd: for a given dose the thickness of the mixed layer is greater for Au than Pd; i.e., the amount of diffusion within the collision cascade is greater for Au than Pd.

Figure 8 shows concentration-versus-dose curves for Au and Pd films in the thickness range of 100 Å to 200 Å. The two curves are offset because for a given film thickness there is more interdiffusion and hence lower concentration for Au than for Pd. At high concentrations, polycrystalline solid solutions are formed. At lower concentrations, about 30 at. % for Au and about 15 at. % for Pd, single-crystal solid solutions are formed. The schematic diagrams indicate that for a low dose, interdiffusion is confined to the interface region; for a higher dose, the Au or Pd layer is intermixed with Cu at concentrations dependent on the ion dose (solid curves),

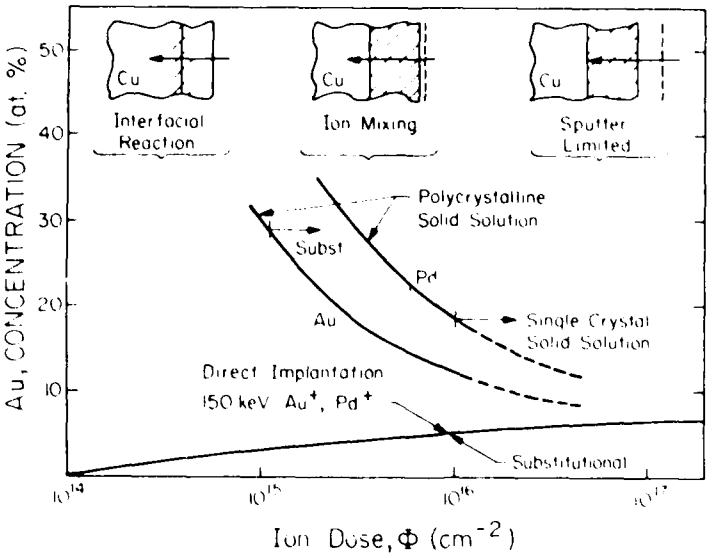

Fig. 8 - Concentration versus dose for Au and Pd films, 100 - 200 Å, ion mixed with 300 keV Xe ions. The lower curve is for direct implantation of 150 keV Au or Pd.

and at even higher doses, sputter erosion will determine the concentrations. The lower cover shows the concentrations that can be achieved by direct implantation of 150 keV Au or Pd into Cu. There should be two curves reflecting the differences in ion ranges and sputtering coefficients between the two species. However, the differences are small compared to the concentrations achieved by ion-beam-mixing.

Summary

Both direct implantation and ion-beam-mixing can be used to form substitutional single-crystal solid solutions of Au or Pd at low atomic concentrations on Cu single-crystals. With direct high-dose implantation, the maximum concentration of Au or Pd is limited to less than 10 at. % due to sputtering effects. With ion-beam-mixing higher concentrations can be achieved at one or two orders of magnitude lower Xe ion doses. At Pd and Au concentrations of ≈ 15 and 30 at. % polycrystalline solid solutions are formed. For ion mixing with Xe ions incident on Cu crystals held near room temperature, the amount of interdiffusion of Au is greater than that of Pd.

These results show that ion-beam-mixing can be used as an alternative to direct implantation in cases where the implanted ion species can be deposited as a thin film. In ion-beam-mixing, inert ions can be used at sub-

stantially lower doses than with direct implantation and higher concentrations can be achieved.

References

1. N. E. W. Hartley, "Friction and Wear of Ion-Implanted Metals - A Review", Thin Solid Films, 64 (1979) pp. 177 - 190.

2. James A. Borders, "Metastable Phases in Metals Produced by Ion Implantation",pp. 313 - 339 in Annual Review of Materials Science, 9, Robert A. Huggins, Richard H. Bube and David A. Vermilyea, Eds.; Annual Reviews, Inc., Palo Alto, Calif., 1979.

3. A. Ali, W. A. Grant and P. J. Grundy, "Amorphous Ni-P Alloys Prepared by Ion Implantation", Radiation Effects, 34 (1977) pp. 251-254.

4. W. A. Grant, "Amorphous Metals and Ion Implantation", Journal of Vacuum Science and Technology, 15 (5) (1978) pp. 1644 - 1649.

5. John M. Poate, James A. Borders, Anthony G. Cullis and James K. Hirvonen , "Ion Implantation as an Ultrafast Quenching Technique for Metastable Alloy Production: The Ag-Cu System", Applied Physics Letters, 30 (8) (1977) pp. 365 - 368.

6. Anthony G. Cullis, John M. Poate and James A. Borders, "The Physical State of Implanted Tungsten in Copper", Applied Physics Letters, 28 (6) (1976) pp. 314 - 316.

7. D. K. Sood, "Empirical Rules for Substitutionality in Metastable Surface Alloys Produced by Ion Implantation", Physics Letters, 68A (5,6) (1978) pp. 469 - 472.

8. Zong-Long Liau and James W. Mayer, "Limits of Composition Achievable by Ion Implantation", Journal of Vacuum Science and Technology, 15 (5) (1978) pp. 1629 - 1635.

9. Bor-Yeu Tsaur, Zong-Long Liau and James W. Mayer, "Ion-Beam-Induced Silicide Formation", Applied Physics Letters, 34 (2) (1979) pp. 168 - 170.

10. Bor-Yeu Tsaur, Zong-Long Liau and James W. Mayer, "Formation of Si-Enriched Metastable Compounds in the Pt-Si System Using Ion Bombardment And Post Annealing", Physics Letters, 71A (2,3) (1979) pp. 270 - 272.

11. Bor-Yeu Tsaur, Silvanus S. Lau, Zong-Long Liau and James W. Mayer, "Ion -Beam-Induced Intermixing of Surface Layers", Thin Solid Films, 63 (1979) pp. 31-36.

BIBLIOGRAPHY

1. E. A. Wolicki, C. R. Gossett, K. W. Marlow, and M. E. Toms, "Capabilities for Nonnuclear Applications with Nuclear Facilities at NRL," NRL Report 6599, 17 October 1967.

2. I. Manning and D. Padgett, "Transport Theory of Penetration by Heavy Ions," NRL Memorandum Report 2631, August 1973.

3. I. Manning and G. P. Mueller, "Depth Distribution of Energy Deposition in Ion Bombardment," Comp. Phys. Comm. **7**, 85 (1974).

4. G. P. Mueller, "Total Cross-Section Corresponding to the Differential Cross-Section of Lindhard, Nielsen and Scharff," Radiat. Eff. **21**, 253 (1974).

5. J. W. Butler, "Ion Implantation and Tribology," Proceedings of ONR-NRL Tribology Workshop, Washington, DC, 14-16 October 1975.

6. H. W. Kugel, L. Eytel, G. K. Hubler, and D. E. Murnick, "The Temperature Dependence of Hyperfine Fields at Rare Earth Nuclei Recoil Implanted into Iron and Nickel Hosts," Phys. Rev. **B13**, 3697 (1976).

7. J. W. Butler, "Ion Implantation and Wear," Reports, Memoranda and Technical Notes of the Materials Research Council Summer Conference, La Jolla, CA (University of Michigan Document 005020, 1976) p. 255.

8. Irwin Manning, Mervine Rosen, and J. E. Westmoreland, "Adaptation of a Program for Depth Distribution of Energy Deposition by Ion Bombardment: Calcualtion of Ion Lateral Ranges," Comp. Phys. Comm. **12**, 335 (1976).

9. I. Manning, M. Rosen, and J. E. Westmoreland, "Computer Code for the Calculation of Lateral Range of a PKA," NRL Memorandum Report 3358, September 1976.

10. J. M. Poate, J. A. Borders, A. G. Cullis, and J. K. Hirvonen, "Ion Implantation as an Ultrafast Quenching Technique for Metastable Alloy Production: The Ag-Cu System," Appl. Phys. Letters **30**, 365 (1977).

11. G. K. Hubler, P. R. Malmberg, and C. N. Phillippi, "Ion Implantation of Infrared Window Materials." Contribution to Navy Laser Hardened Materials Development Program, NRL Memorandum Report 3447, January 1977.

12. G. K. Hubler, P. R. Malmberg, and C. N. Phillippi, "Ion Implantation of Infrared Window Materials," Proceedings of 3rd DoD Conference on Laser Effects, Vulnerability, and Countermeasures (Classified), San Diego, CA, July (1977).

13. G. P. Mueller and Mervine Rosen, "A Boltzmann Transport Code for Ion Penetration in Matter," NRL Memorandum Report 3556, July 1977.

14. J. K. Hirvonen, "Spinodal Decomposition in Amorphous Au-Implanted Pt," Appl. Phys. Letters **32**, 25 (1978).

15. A. G. Cullis, J. A. Borders, J. K. Hirvonen, and J. M. Poate, "Metastable Alloy Layers Produced by Implantation of Ag^+ and Ta^+ Ions into Cu Crystals," Phil. Mag. **B32**, 615 (1978).

16. J. K. Hirvonen, "Ion Implantation in Tribology and Corrosion Science," J. Vac. Sci. Technol. **15**, 1662 (1978).

17. Wen-Wei Hu, C. R. Clayton, H. Herman, and J. K. Hirvonen, "Fatigue-Life Enhancement by Ion Implantation," Scr. Met. **12**, 697 (1978).

18. E. McCafferty and G. K. Hubler, "Electrochemical Behavior of Palladium-Implanted Titanium," J. Electrochem. Soc. **125**, 1892 (1978).

19. G. K. Hubler, P. R. Malmberg, C. A. Carosella, T. A. Kennedy, and G. E. Matthews, Jr., "Ion Implantation of Infrared Window Materials," Contribution to Navy Laser Hardened Materials Development Program, NRL Memorandum Report 3798, July 1978.

20. J. W. Butler, "Some Effects of Ion Implantation on Fluid-Solid Surface Interactions," Proceedings of the Fourth Symposium on Fluid-Solid Surface Interactions, sponsored by the U.S. Department of the Navy and the West Germany Federal Ministry of Defense, 18-20 October 1978, National Bureau of Standards, Gaithersburg, MD, p. 267.

21. J. K. Hirvonen, C. A. Carosella, R. A. Kant, I. L. Singer, R. Vardiman, and B. B. Rath, "Improvement of Metal Properties by Ion Implantation," Thin Solid Films **63**, 5 (1979).

22. G. K. Hubler, P. R. Malmberg, and T. P. Smith, III, "Refractive Index Profiles and Range Distributions of Silicon Implanted with High-Energy Nitrogen," J. Appl. Phys. **50**, 7147 (1979).

23. G. K. Hubler, C. N. Waddell, W. G. Spitzer, J. E. Fredrickson, S. Prussin, and R. G. Wilson, "High-Fluence Implantations of Silicon: Layer Thickness and Refractive Indices," J. Appl. Phys. **50**, 3294 (1979).

24. R. A. Kant, J. K. Hirvonen, A. R. Knudson, J. S. Wollam, "Surface Hardening of Beryllium by Ion Implantation," Thin Solid Films **63**, 27 (1979).

25. W. G. Spitzer, J. S. Ko, C. N. Waddell, G. K. Hubler, and J. E. Fredrickson, "Plasma Region in High-Fluence Implants of Phosphorus in Amorphized Silicon," J. Appl. Phys. **50**, 3775 (1979).

26. Y. F. Wang, C. R. Clayton, G. K. Hubler, W. H. Lucke, and J. K. Hirvonen, "Applications of Ion Implantation for the Improvement of Localized Corrosion Resistance of M50 Bearing Steel," Thin Solid Films **63**, 11 (1979).

27. J. K. Hirvonen, "Implantation Into Metals - Mechanical Property Changes," Proceedings of the 1st Conference on Ion Beam Modification of Materials, eds., J. Gyulai, T. Lohner, and E. Pasztor, Central Research Institute for Physics, H-1525, Budapest 114 POB 49, Hungary, Vol. III, p. 1753 (1979).

28. J. K. Hirvonen and J. W. Butler, "Improved Corrosion and Mechanical Behavior of Alloys by Ion Implantation," 1978 Science and Engineering Symposium Proceedings (Joint Air Force and Navy), Vol. IV (Basic Research), Navy Material Command and Air Force Systems Command, p. 981 (1979).

29. J. K. Hirvonen, J. W. Butler, T. P. Smith, III, R. A. Kant, and V. C. Westcott, "Sliding-Wear Reduction by Ion Implantation," Proceedings of the 1st Conference on Ion Beam Modification of Materials, eds., J. Gyulai, T. Lohner, and E. Pasztor, Central Research Institute for Physics, H-1525, Budapest 114, POB 49, Hungary, Vol. III, p. 1973 (1979).

30. J. K. Hirvonen, J. M. Poate, Z. L. Liau, and J. W. Mayer, "Sputtering Limitations for High-Dose Implantations," Proceedings of the 1st Conference on Ion Beam Modification of Materials, eds., J. Gyulai, T. Lohner, and E. Pasztor, Central Research Institute for Physics, H-1525, Budapest 114, POB 49, Hungary, Vol. III, p. 1519 (1979).

31. G. K. Hubler, P. R. Malmberg, C. A. Carosella, T. P. Smith, III, W. G. Spitzer, C. N. Waddell, and C. N. Phillippi, "Optical Effects Resulting from Deep Implants of Silicon with Nitrogen and Phosphorus," Proceedings of the 1st Conference on Ion Beam Modification of Materials, eds., J. Gyulai, T. Lohner, and E. Pasztor, Central Research Institute for Physics, H-1525, Budapest 114, POB 49, Hungary, Vol. II, p. 1323 (1979).

32. W. W. Hu, C. R. Clayton, H. Herman, J. K. Hirvonen, and R. A. Kant, "Fatigue-Life Enhancement of Steel by Nitrogen Implantation," Proceedings of the 1st Conference on Ion Beam Modification of Materials, eds., J. Gyulai, T. Lohner, and E. Pasztor, Central Research Institute for Physics, H-1525, Budapest 114, POB 49, Hungary, Vol. III, p. 1977 (1979).

33. D. J. Land, D. G. Simons, J. G. Brennan, M. D. Brown, and J. K. Hirvonen, "Range Distribution for 25-100 keV $^{14}N^{+}$ Ions," Proceedings of the 1st Conference on Ion Beam Modification of Materials, eds., J. Gyulai, T. Lohner, and E. Pasztor, Central Research Institute for Physics, H-1525, Budapest 114, POB 49, Hungary, Vol. I, p. 93 (1979).

34. E. McCafferty, G. K. Hubler, and J. K. Hirvonen, "Corrosion Control by Ion-Implantation," Proceedings of the 1978 Tri-Service Conference on Corrosion, ed. by M. Levy and J. Brown, Materials and Ceramics Information Center, Battelle, OH, p. 435, May 1979.

35. R. G. Vardiman, R. A. Kant, and T. W. Crooker, "The Effect of Ion Implantation on Fatigue Behavior of Ti/6Al/4V Alloy," Report of NRL Progress, p. 4, May 1979.

36. I. Manning, "Use of Range Distributions to Approximate Energy Distributions," F. A. Smidt and L. A. Beach, Coordinators, Cooperative Radiation Effects Simulation Program (Annual Progress Report) NRL Memorandum Report 4080 (October 1979), p. 2.

37. I. Manning, "Approximation for Energy Deposition in Ion Beam Bombardment," F. A. Smidt and L. A. Beach, Coordinators, Cooperative Radiation Effects Simulation Program (Annual Progress Report) NRL Memorandum Report 4080 (October 1979), p. 8.

38. G. K. Hubler, A. R. Knudson, R. D. Willis, P. R. Malmberg, and T. A. Kennedy, "Ion Implantation of Infrared Window Materials," Contribution to Navy Laser Hardened Materials Development Program," NRL Memorandum Report 4134, 28 December 1979.

39. M. Zamanzadeh, A. Allan, H. W. Pickering, and G. K. Hubler, "Effect of Helium-, Iron-, and Platinum-Ion Implantation on Permeation of Hydrogen Through Ion Membranes," ONR Technical Report No. 10 (Contract No. N00-14-75-C-0264), July 1979.

40. G. K. Hubler and E. McCafferty, "The Corrosion Behaviour and Rutherford Backscattering Analysis of Palladium-Implanted Titanium," Corros. Sci. **20**, 103 (1980).

41. R. N. Bolster and I. L. Singer, "Surface Hardness and Abrasive Wear Resistance of Nitrogen-Implanted Steels," Appl. Phys. Letters **36**, 208 (1980).

42. I. L. Singer and J. S. Murday, "The Chemical State of Ion-Implanted Nitrogen in $Fe_{18}Cr_8Ni$ Steel," J. Vac. Sci. Technol. **16**, 330 (1980).

43. G. P. Mueller, "New Analytical Calculation of Displacement Damage," Nucl. Instr. and Methods **170**, 389 (1980).

44. G. P. Mueller, "Differential Cross Section and Related Integrals for the Moliere Potential," Radiat. Eff. Letters **50**, 87 (1980).